NOTICE

The quality of this microform is heavily dependent upon the quality of the original thesis submitted for microfilming. Every effort has been made to ensure the highest quality of reproduction possible.

If pages are missing, contact the university which granted the degree.

Some pages may have indistinct print especially if the original pages were typed with a poor typewriter ribbon or if the university sent us an inferior photocopy.

Reproduction in full or in part of this microform is governed by the Canadian Copyright Act, R.S.C. 1970, c. C-30, and subsequent amendments.

AVIS

La qualité de cette microforme dépend grandement de la qualité de la thèse soumise au microfilmage. Nous avons tout fait pour assurer une qualité supérieure de reproduction.

S'il manque des pages, veuillez communiquer avec l'université qui a conféré le grade.

La qualité d'impression de certaines pages peut laisser à désirer, surtout si les pages originales ont été dactylographiées à l'aide d'un ruban usé ou si l'université nous a fait parvenir une photocopie de qualité inférieure.

La reproduction, même partielle, de cette microforme est soumise à la Loi canadienne sur le droit d'auteur, SRC 1970, c. C-30, et ses amendements subséquents.

High Peak Power Frequency Conversion of Visible Light into Near-Infrared Laser Radiation Using a Nonlinear $LiNbO_3$ Crystal

by

Robert Parent

Thesis submitted to the School of Graduate Studies
of the University of Ottawa in partial fulfilment
of the requirements for the degree
of Master of Science in Physics

Physics Department
Faculty of Science
University of Ottawa
Ottawa, Canada
1991

ISBN 0-315-68055-5

UNIVERSITÉ D'OTTAWA
UNIVERSITY OF OTTAWA

Acknowledgements

I take this opportunity to thank Chris Church for helping proofread and criticize some portions of this document as well as the research paper to be published. His help allowed me to understand some aspects of the written word. I would also like to thank Louis Allard for helping with some of the measurements of the damage threshold of the crystal and the full pump power utilization measurements. I would also like to thank the following friends at the Physics Department who helped make life a little more bearable during my Master's research: Pam Tume, Riccardo Brun Del Re, Chris Church, Micheal Jackson, David LeBlanc, Michel Royer, Ye Wang, Paula Heron, the students from 3rd year, as well as the professors, the secretaries and staff of the department.

The most credit due of course is to my supervisor, Emery Fortin, who succeeded in getting me to work hard in the laboratory. I must also say that I am impressed with his stamina for discussing the ideas presented herein so that he and I fully understood the ideas behind the different physical processes. The tortuous task of reading the first 2 drafts of this thesis was also born by my supervisor. His comments and guidance were very usefull and permitted me to obtain a final version of the present thesis with only 2 revisions.

Dedication

I also take this opportunity to dedicate this thesis to my parents Leona and Bernard Parent, to my sister and brothers Mona, André, Claude and Gilles who have provided me with unconditional support in whatever endeavours I have undertaken throughout life. As with many people, my friends are very important to me, without their companionship and friendship I would be but a small fraction of the human being that I am presently, therefore little bits of these hundreds of people are also scattered throughout the pages of this text in subliminal ways.

I would like to dedicate this thesis to a friend who was very important to me in my formative years, Eric Gagnon. Although he passed away just a couple of weeks before I began my Master's Degree, I still feel his presence in many things that I do each and every day. During our formative years he influenced to a significant degree the moral code that I now live by. He also taught me that friendship transcends time. May he be happy in the afterlife.

Abstract

High peak power 10 ns near-infrared coherent radiation has been obtained from frequency conversion of a dye laser beam in a $LiNbO_3$ crystal. The observed tuning range spanned the 0.734 to 2.853 μm wavelength range. An examination of optical parametric oscillator frequency conversion revealed that the production of monochromatic laser radiation at the signal wavelength was only obtainable for a limited portion of the accessible pump wavelengths. In contrast, optical parametric amplifier frequency conversion resulted in the production of bichromatic infrared radiation for the entire accessible pump wavelength range. It appears that the crystal pump acceptance bandwidth leading to reduced power conversion can be described by a model in which the signal wave is assumed to have zero bandwidth.

Statement of Originality

The following observations appear to be original:

1. The use of a 10 ns pump pulse, rapidly tunable dye laser having a peak intensity in the 480 MW/cm^2 range.

2. The production of 10 ns ,10 Hz near-infrared laser radiation having a peak intensity in the 27 MW/cm^2 range.

3. Mapping of the different characteristics of optical parametric amplifier operation.

4. The observation that the pump acceptance bandwidth for optical parametric amplifier operation is determined by the signal wave.

5. A damage threshold of 240 MW/cm^2 was observed for an antireflection coated crystal with the peak transmission centred at 600 nm.

Table of Contents

Abstract	i
Statement of Originality	ii
Table of Contents	iii
Introduction	1
Chapter 1. Theory of Parametric Frequency Conversion	10
Chapter 2. $LiNbO_3$	22
Chapter 3. Experimental Setup and Equipment	32
Chapter 4. Tuning Curves	42
Chapter 5. OPO Operation	50
A. Variation of the Output Power Produced by the OPO Using a Constant Input Power	51
B. Behaviour of the Output Power with the Input Power	57
C. Temporal Profile of the Signal Wave	61
D. Spatial Profile of the Signal Wave	62
E. Spectral Analysis of the Signal Wave	62
F. Conclusion	65
Chapter 6. OPA Operation	69
A. Behaviour of the Output Power from the OPA	69
B. Theoretical Crystal Pump Acceptance Bandwidths	71
C. Determination of the Wave Limiting the Crystal Pump Acceptance Bandwidth in OPA Operation	74
D. Distribution of the Output Power Between the Waves Generated During OPA Operation	79

E. Model of the Output Power Produced During OPA Operation 81

F. Measurement of the Crystal Damage Threshold 89

G. Maximum Observed Conversion Efficiency 91

H. Full Pump Power Utilization 91

I. Conclusion 94

Conclusion 95

Appendix I 97

Appendix II 99

Appendix III 100

Appendix IV 101

Appendix V 102

References 103

Introduction

This thesis will present the results obtained during the past year and a half while mapping out the characteristics of a high-peak-power near-infrared laser system. The laser radiation was produced by frequency converting the output of a dye laser within an $LiNbO_3$ crystal. Although this has been previously achieved by many other researchers, no one has attempted such an experiment with 10 ns laser pump pulses. The system has been operated both as an optical parametric oscillator as well as a single pass parametric amplifier. The investigation of the latter method of operation has revealed interesting results with regards to the behaviour of the output power. These results which seem fundamental to the latter method of operation have as yet remained unreported in the reference publications. The system operated as an optical parametric amplifier (OPA) has been able to produce output powers as high as 855 kW.

This infrared laser source has been developed as a research tool for different experiments. Near infrared radiation sources are very useful for examining the various properties of semiconductors because of the particular energies required for transitions between states. Due to a lack of tunable laser sources in the near infrared wavelength range, conventional sources such as tungsten lamps are still being used to study the properties of semiconductors such as GaAs, InGaAsP and InGaAs. Presently there are only a couple of tunable laser systems operating in the near infrared which are

commercially available. The Ti:Sapphire and the MgF_2:Co laser, tunable in the 0.700 to 1.050 μm and 1.7 to 2.6 μm range, respectively, are just two examples of such systems. Of the known sources available, the accessible tuning range obtainable from frequency conversion in $LiNbO_3$ is by far the largest covering 0.55 to 4.5 μm. Due to this broadband tunability, this type of infrared radiation source is a very useful research tool for optoelectronic and semiconductor research.

Low- or medium-intensity laser sources in the near infrared are useful for the study of semiconductors such as GaAs, InGaAsP and InGaAs which have their band gaps in the near infrared. These sources are also useful for fundamental research in optical communications, since optical fibres have peak transmission coefficients in the 1 to 2 μm range. For the investigation of nonlinear optical phenomena, near-infrared intensities in the MW/cm^2 range can be essential since the probability of occurrence of nonlinear processes varies rapidly with the excitation intensity. Fundamental studies in saturation and multiple-photon spectroscopy in semiconductors impose the additional requirement of rapid tunability.

Frequency conversion of a frequency doubled $CaWO_4:Nd^{3+}$ laser (529 nm) beam was first achieved in 1965 by Giordmaine and Miller[1] by using a $LiNbO_3$ optical parametric oscillator. In 1969, Falk and Murray were able to obtain as much as 340 kW of peak power from a combination temperature and angle tuned $LiNbO_3$ OPO (25 to 30 ns pump pulse length)[2]. In this system the output beam position was dependent upon the wavelength because of the crystal dispersive power. Later Wallace described a system that used a Nd:YAG laser to pump a parametric generator[3] in which the output beam position was wavelength independent. This wavelength independence occurred since 90° phase

matching was used between the pump and generated waves within the crystal. The infrared wavelength selection was achieved by varying the crystal temperature. The resulting system was capable of producing peak powers of 4 kW (0.54 mJ at 130 ns pulse length). In 1972, Wallace described a rapidly tunable system[4] consisting of a frequency doubled 0.1 μs Nd:YAG pumped tunable dye laser (0.5 mJ per pulse). In this system the dye wavelength was used to select the infrared wavelengths for fixed parametric crystal temperatures. This configuration resulted in the first rapidly tunable frequency conversion system which did not suffer from beam walk-off. The descriptions of other temperature tuned sources have appeared over the years[5,6,8,9,10]. Of these systems the ones achieving the highest peak powers are described by G. Ionushauskas, A. Piskarskas, V. Sirutkaitis, and A. Yuozapavichyus[6] and M. Ignatavichyus, G. Orshevskii, V. Potsyunas, and É. Skardhyus[8] and produced peak powers of 250 MW (2.5 mJ for 10 ps) and 200 MW (4 mJ for 25 ps), respectively. Rapid tuning of these sources is not possible since a relatively long time is required to achieve a stable temperature and temperature gradient within the crystal. In the 1970's a commercial infrared system pumped by a flashlamp pumped dye laser was available from Chromatix Corp. The $LiNbO_3$ Optical Parametric Oscillator was capable of producing pulses that were approximately 1 μs long attaining peak powers as high as 1 kW. Recently, M.L.W. Thewalt, and D.J.S. Beckett[7] extended this technique by frequency converting the output from a 6 kHz Cu Vapour pumped dye laser (30 ns pulse length) using a Chromatix Optical Parametric Oscillator. They were able to obtain peak powers as high as 1.3 kW (23 μJ for a 17.8 ns pulse length) which is of the same order of magnitude as that obtainable with the original system.

A simple model of the frequency conversion process in $LiNbO_3$ is presented at this time. This model should allow a mental picture of the physical phenomena to be formed.

It is well known that all materials in nature become polarized when they interact with electromagnetic waves. For normal everyday experiences, the resultant polarization is adequately described by the following relationship:

$$\vec{P}=\varepsilon_0 \overline{\chi}^{(1)} \vec{E} \tag{0.1}$$

Here $\vec{P}$ and $\vec{E}$ are vectors while $\overline{\chi}^{(1)}$ is the 1st order susceptibility tensor. In general the susceptibility is not an isotropic quantity for a given medium, hence it cannot be approximated by a scalar quantity.

When the amplitude of the incident electromagnetic waves become sufficiently large, relation (0.1) is no longer valid. In such cases the resultant electronic polarization dependent on the electromagnetic field is better approximated by the following Taylor's series in powers of the electric field:

$$P_i=\varepsilon_0(\sum_j \chi_{ij}^{(1)}E_j + \sum_{j,k} \chi_{ijk}^{(2)}E_jE_k + \sum_{j,k,l} \chi_{ijkl}^{(3)} E_jE_kE_l + ...) \tag{0.2}$$

Where the $\overline{\chi}^{(n)}$ are the n^{th} order susceptibility tensors. These coefficients are frequency and direction dependent for all crystals.

Proceeding with the description of the simple picture, imagine two electromagnetic waves having the same polarization direction (but not a necessary condition), $\vec{E}_1$ and $\vec{E}_2$, collinearly propagating within a non-centrosymmetric crystal. These waves will interact

with the electrons within the crystal in a fashion described by the n^{th} order susceptibility tensors. The resulting electronic polarization within the crystal is described by equation (0.2). As further simplifications, the waves are assumed to be harmonic and polarized in the z-direction. The total field can thus be written as follows:

$$\vec{E} = \vec{E}_1 + \vec{E}_2 = E_1 \hat{z} \sin(k_1 x - \omega_1 t) + E_2 \hat{z} \sin(k_2 x - \omega_2 t) \qquad (0.3)$$

The 2^{nd} order non-linear polarization stimulated within the crystal, which is the term we are concerned with in the particular frequency conversion process studied in this thesis, is then described by the following equation:

$$P_z \alpha E_z^2$$

$$= E_1^2 \sin^2(k_1 x - \omega_1 t) + E_2^2 \sin^2(k_2 x - \omega_2 t) + 2 E_1 E_2 \sin(k_1 x - \omega_1 t) \sin(k_2 x - \omega_2 t)$$

$$= \frac{E_1^2}{2} + \frac{E_2^2}{2} - \frac{E_1^2}{2}\cos(2k_1 x - 2\omega_1 t) \frac{E_2^2}{2} \cos(2k_2 x - 2\omega_2 t)$$
$$+ E_1 E_2 \cos[(k_1 - k_2)x - (\omega_1 - \omega_2)t] - E_1 E_2 \cos[(k_1 + k_2)x - (\omega_1 + \omega_2)t] \qquad (0.4)$$

An examination of this equation reveals terms describing a wave having a polarization separable into components oscillating at several frequencies. These are: 0, 0, $2\omega_1$, $2\omega_2$, $\omega_1 - \omega_2$ and $\omega_1 + \omega_2$ and are referred to as the D.C.(or steady state), the doubled, the difference and the summed frequencies respectively. Due to momentum considerations, the electrons which have been set into motion will produce electromagnetic radiation propagating along

the original direction of the incident waves. The properties of the medium in conjunction with phase-match conditions, to be presented later, usually allow the production of an electromagnetic wave at only one of these frequencies. These conditions can be obtained classically or from modern principles and impose conservation of energy and momentum on the waves participating in the physical phenomena.

Parametric frequency conversion within $LiNbO_3$ occurs when the difference frequency generation is the dominant phase-matched process. In this process, the incident pump wave interacts with broadband quantum noise present within the crystal. This allows the simultaneous amplification of two waves, called the signal and idler, satisfying the following equations:

$$\omega_{pump} = \omega_{signal} + \omega_{idler} \quad \text{(conservation of energy)} \tag{0.5}$$

$$\vec{k}_{pump} = \vec{k}_{signal} + \vec{k}_{idler} \quad \text{(conservation of momentum)} \tag{0.6}$$

The generated radiation at the shorter wavelength is called the signal wave while the longer wavelength one is called the idler wave. A more detailed analysis of this process will be given in Chapter 1.

The experimental configuration of the system used to produce near infrared laser radiation is shown in figure 0.1. The precise details of the individual components will be presented later. The production of near-infrared radiation occurs in several steps. The 532 nm pump beam for the dye laser is obtained from the frequency doubled 1064 nm line of an

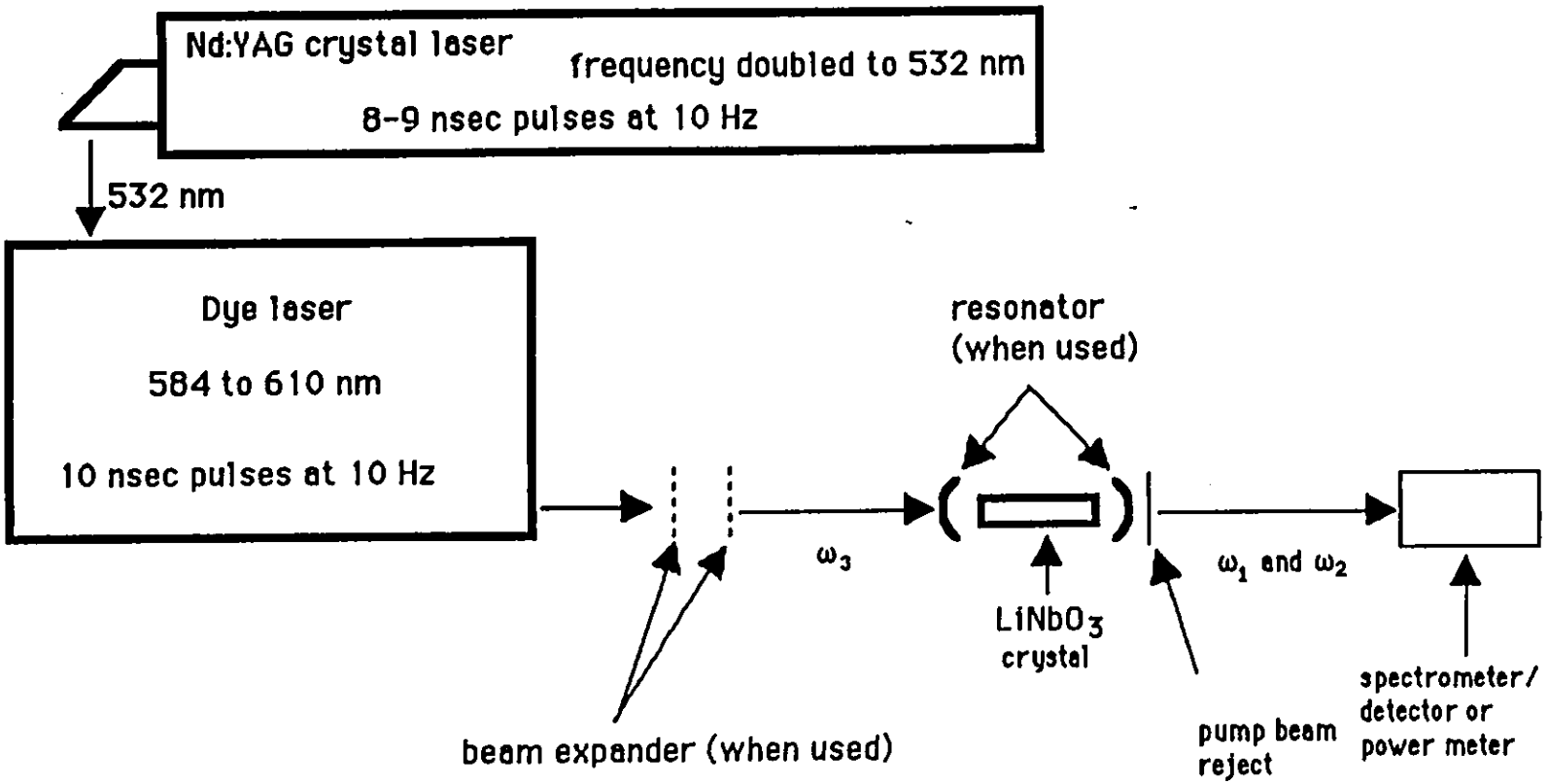

Figure 0.1. Experimental Setup

Nd:YAG laser. Once the dye is excited by the doubled Nd:YAG laser beam, tunable laser radiation in 584 to 610 nm range is directed through an $LiNbO_3$ crystal. As this beam propagates through the crystal, it interacts with the electrons of the crystal and the broadband electromagnetic noise within the crystal. This interaction results in the production of radiation at two new frequencies satisfying equations (0.5) and (0.6). Beam walk-off of all the waves is avoided by using 90° phase-matching between the directions of propagation of the generated signal and idler waves, and the pump wave.

The system can be operated in two different ways. The first of these is called optical parametric oscillation (OPO) and allows the preferential production of one of the generated waves by resonating the other with the help of mirrors highly reflecting at the idler wavelengths. The other method of operation is called optical parametric amplification (OPA) and allows the nondiscriminatory production of waves through single pass frequency conversion of the pump wave. The operating characteristics of these two method was examined in some details. These results are presented in the experimental portion of the thesis consisting of Chapters 4, 5, and 6.

The experiments that were performed allowed the production of infrared radiation covering the 0.734 μm to 2.853 μm range. These wavelengths were produced for pump wavelengths in the 584 to 610 nm range for crystal temperatures at 25 C° intervals from 225 °C to 425 °C. Changing the pump wavelength allows fine tuning of the output wavelengths and changing the temperature allows coarse tuning of the latter. The production of radiation at 0.687 μm was also observed for a 425 °C crystal temperature using a 560 nm pump wavelength. This implied the production of a complementary wave with a 3.1 μm wavelength. The pump and signal laser pulses were found to be 10 ns (FWHM) in length. The maximum conversion efficiencies of input power into signal and

idler power were 46 % and 30 % for OPA and OPO operation, respectively. These efficiencies were obtained with 560 kW of peak pump power. A maximum output power of 855 kW was observed for 3.3 MW of input pump power. This output power was obtained by operating the pump laser at the peak output power obtainable for this particular pump wavelength while doubling the input beam diameter in order to avoid damaging the crystal.

The damage threshold intensity of one of the crystals examined was found to be 240 MW/cm^2. The output beam size at the signal wavelength for an unexpanded pump beam was 2 mm in radius with a 4.3 mrad half-angle divergence. It was also found that the pump acceptance bandwidth of the crystal is determined by the signal wavelength during OPA operation. This latter result is discussed in detail in Chapter 6.

The fascinating details of nonlinear optical frequency conversion in $LiNbO_3$ are presented in the following chapters. A presentation of the classical theory of parametric frequency conversion is followed by an examination of the properties of $LiNbO_3$ pertinent to this phenomena. A description of the equipment and experimental setup is then presented. The experimental and theoretical tuning curves, that is the values of the output wavelengths generated for given pump wavelengths, are compared. This comparison is then followed by an examination of the optical parametric oscillator and amplifier methods of operation. These include an investigation of the effects of the pump power, pump wavelength and crystal temperature on the infrared power produced in the frequency conversion process.

Chapter 1

The general theory of parametric frequency conversion is derived in this chapter. Maxwell's equations are used as the starting point for the description of the electromagnetic waves interacting with the nonlinear medium. Once the rapid spatial and temporal variations of the waves are taken into account, the second order terms will be eliminated from the resultant equations in order to obtain their final form. From these equations the phase-match conditions governing frequency conversion are obtained. A single pass loss coefficient is also defined in order to take into account the various losses within the system. The solution of these equations in the low conversion limit is shown so that a deeper understanding of the frequency conversion process can be obtained. Theoretical conversion efficiencies for OPO and OPA methods of operation are also given for future comparison with the experimental data.

The theoretical reasoning that follows parallels the one described by Byer[11] and includes some of the steps not shown in his derivation. Maxwell's equations are used as the starting point for the derivation of the equations governing the frequency conversion process. These equations are as follows:

$$\vec{\nabla} \times \vec{E} = - \frac{\partial \vec{B}}{\partial t} \tag{1.1}$$

$$\vec{\nabla} \times \vec{H} = \frac{\partial \vec{D}}{\partial t} + \vec{J} \tag{1.2}$$

where the different quantities are assumed to have the following forms,

$$\vec{D} = \varepsilon_0 \vec{E} + \vec{P}$$

$$\vec{J} = \sigma \vec{E} \tag{1.3}$$

$$\vec{B} = \mu_0 \vec{H}$$

Equation (1.1) can be transformed by applying the curl operator, this results in the following equation:

$$\vec{\nabla} \times (\vec{\nabla} \times \vec{E}) = - \frac{\partial (\vec{\nabla} \times \vec{B})}{\partial t}$$
$$= - \mu_0 \frac{\partial (\vec{\nabla} \times \vec{H})}{\partial t} = - \mu_0 \frac{\partial}{\partial t} \left(\frac{\partial \vec{D}}{\partial t} + \vec{J} \right) \tag{1.4}$$

Using the vector relation $\vec{\nabla} \times (\vec{\nabla} \times \vec{E}) = \vec{\nabla} \left(\vec{\nabla} \cdot \vec{E} \right) - \vec{\nabla}^2 \vec{E}$ and $\vec{\nabla} \cdot \vec{E} = 0$, equation (1.4) can then be transformed into the following form:

$$-\vec{\nabla}^2\vec{E} = -\mu_0\left[\frac{\partial^2\vec{D}}{\partial t^2} + \frac{\partial\vec{J}}{\partial t}\right] \tag{1.5}$$

Once relations (1.3) are introduced into the latter, the following equation is obtained:

$$\vec{\nabla}^2\vec{E} = \mu_0\left[\varepsilon_0\frac{\partial^2\vec{E}}{\partial t^2} + \frac{\partial^2\vec{P}}{\partial t^2} + \sigma\frac{\partial\vec{E}}{\partial t}\right] \tag{1.6}$$

$$\rightarrow \quad \vec{\nabla}^2\vec{E} - \mu_0\varepsilon_0\frac{\partial^2\vec{E}}{\partial t^2} - \mu_0\sigma\frac{\partial\vec{E}}{\partial t} = \mu_0\frac{\partial^2\vec{P}}{\partial t^2} \tag{1.7}$$

An examination of this equation reveals how the crystal polarization and the electromagnetic waves interact within the crystal. The waves are assumed to be described by the following vector relations:

$$\vec{E}(\vec{r},t) = \frac{1}{2}\left[\vec{E}(\vec{r},\omega)\, e^{i\left(\vec{k}\cdot\vec{r} - \omega t\right)} + c.c.\right] \tag{1.8}$$

$$\vec{P}(\vec{r},t) = \frac{1}{2}\left[\vec{P}(\vec{r},\omega)\, e^{i\left(\vec{k}\cdot\vec{r} - \omega t\right)} + c.c.\right] \tag{1.9}$$

Assuming the waves are propagating in the z-direction and substituting the above expressions into equation (1.7), the following equation is obtained after a little algebra:

$$\frac{1}{2}\frac{\partial^2 E}{\partial z^2} + ik\frac{\partial E}{\partial z} - \frac{\mu_0\sigma}{2}\frac{\partial E}{\partial t} + i\frac{\omega\mu_0\sigma}{2}E - \frac{\mu_0\varepsilon_0}{2}\frac{\partial^2 E}{\partial t^2} + i\omega\mu_0\varepsilon_0\frac{\partial E}{\partial t}$$
$$= \frac{\mu_0}{2}\frac{\partial^2 P}{\partial t^2} - i\omega\mu_0\frac{\partial P}{\partial t} - \frac{\omega^2\mu_0}{2}P \qquad (1.10)$$

Since all the rapid spatial and temporal variations of the waves and the electron polarizations have been accounted for by equations (1.8) and (1.9), it is possible to make the following approximations:

$$\omega^2 P >> \omega\frac{\partial P}{\partial t} >> \frac{\partial^2 P}{\partial t^2}$$

$$k\frac{\partial E}{\partial z} >> \frac{\partial^2 E}{\partial z^2}$$

and,

$$\omega E >> \frac{\partial E}{\partial t}$$

therefore equation (1.10) becomes:

$$ik\frac{\partial E}{\partial z} + i\frac{\omega\mu_0\sigma}{2}E + i\omega\mu_0\varepsilon_0\frac{\partial E}{\partial t} = -\frac{\omega^2\mu_0}{2}P \qquad (1.11)$$

Using $k = n\omega/c$ and $\mu_0\varepsilon_0 = 1/c^2$ and dividing by ik we obtain:

$$\frac{\partial E}{\partial z} + \frac{\alpha}{n} E + \frac{1}{nc}\frac{\partial E}{\partial t} = i\frac{\mu_0 c\omega}{2n} P \qquad (1.12)$$

Here α ($= \mu_0\sigma c/2$) is the electric field loss coefficient and is related to the conductivity of the medium. This coefficient can also be redefined to take into account other system losses. Once the behaviour of the electron polarization is known, equation 1.12 can be used to obtain the form of the generated electromagnetic fields and vice-versa.

As shown in Appendix I, electromagnetic fields interacting in nonlinear media can give rise to at least four different oscillating polarizations having frequencies at $2\omega_i$, $2\omega_j$, $\omega_i+\omega_j=\omega_k$, and $\omega_i-\omega_j=\omega_l$ as well as a steady state field (i.e. $\omega_i-\omega_i=0$ and $\omega_j-\omega_j=0$). The generated polarization at all these frequencies can in turn produce oscillating electromagnetic fields due to the oscillating electrons in the dielectric medium (i.e. oscillating dipoles). The fields which will interact in the frequency conversion process must satisfy the following phase-match conditions[12]:

$$\omega_k = \omega_i + \omega_j \qquad (1.13a)$$

$$\vec{k}_k = \vec{k}_i + \vec{k}_j + \Delta\vec{k} \qquad (1.13b)$$

Equation (1.13a) arises because it is not possible to produce an oscillating electron polarization at a given frequency without a driving mechanism. The driving mechanism in this case is provided by an input electromagnetic wave. This electromagnetic wave interacts with the background electromagnetic noise present in the crystal. This interaction

results in beating between two different electromagnetic waves simultaneously present in the crystal, at frequencies ω_i and ω_j, and the incident wave at frequency ω_k. This beating stimulates the electron polarization to oscillate at the three frequencies mentioned in the previous line. This electron oscillation then generates new electromagnetic fields oscillating at these same frequencies. During this process some power of the incident electromagnetic wave at the original frequency ω_k is converted into power at the generated electromagnetic waves having frequencies ω_i and ω_j.

The second equation results since the generated waves must interact in a constructive manner. In order for the waves to interact constructively they must propagate at the same velocity as the original wave for the entire crystal length, l, or in this case the frequency weighted velocity of the generated waves must be the same. Only the waves satisfying equations (1.13) with $|\Delta\vec{k} \cdot \vec{l}| \leq 2\pi$ are amplified in the frequency conversion process ($\Delta\vec{k}$ being the allowable wavevector mismatch). If this last condition is not satisfied destructive interference between the incident and generated waves will occur resulting in the regeneration of the original wave along the crystal length.

Since the wave-vectors are frequency dependent ($k_i = n_i\omega_i/c$), equations (1.13) only contain two independent variables, ω_i and ω_j. Now if a solution to these equations exists the values of ω_i and ω_j can be obtained in principle if ω_k is known. It can be shown that no solution to these equations exist for a material possessing only one index of refraction. It turns out that it is possible to obtain a solution for a material possessing two indices of refraction with sufficient birefringence (Δn). In this case the crystal of choice is

$LiNbO_3$. It is possible to change the crystal birefringence using several methods. These methods are listed in the next paragraph. This freedom in control of the value of the crystal birefringence allows different values of ω_i and ω_j to satisfy equations (1.13). That is, controlling the crystal birefringence allows the production of tunable radiation from the frequency conversion process.

In parametric frequency conversion, only one input wave having a frequency of ω_k, called the pump wave, is provided. The second and third waves which will be enhanced at frequencies ω_i and ω_j (determined by equations 1.13), are provided by the background noise contained within the crystal. With an appropriate choice of the crystal indices of refraction, two specific electromagnetic waves can be amplified from the parametric noise within the crystal. The indices of refraction can be changed by varying the crystal temperature, changing the orientation of the crystallographic axes, applying stress or strain along specific crystal directions, or by applying electric or magnetic fields across specific crystal directions. The choice of the crystal axes orientation used for parametric frequency conversion in $LiNbO_3$ will be presented in Chapter 3.

In the literature, the waves produced in the frequency conversion process have been traditionally called the signal (for the shorter wavelength one) and idler (for the longer wavelength one) waves. Most systems using the parametric frequency conversion process have been concerned with producing radiation at the signal wavelength by resonating the longer idler wave. Although radiation at the signal wavelength is emitted, these systems never emit radiation at the idler wavelength since it is resonated. Therefore the former wave has been dubbed the signal wave and the latter one has been called the idler.

Although phase-matching at the appropriate frequencies is important in the frequency conversion process, there are other factors which must be considered. The most important of these is the coupling coefficient between the electrons set into oscillation within the crystal and the electromagnetic waves within the crystal, it is described by the 2nd order susceptibility tensor, $\chi^{(2)}(-\omega_i, \omega_j, \omega_k)$. If the coupling constant is too small, the losses in the system will prevent the conversion process from occurring. Therefore the material used in the frequency conversion process must possess a sufficiently large 2nd order coupling coefficient if very low pump powers are used.

Before concluding this chapter, the equations describing parametric frequency conversion for small pump wave power depletion is presented (i.e. E_3 ~ constant electromagnetic pump field). Assuming a crystal polarization described by the equation in Appendix I, the equations governing the amplitude of the electromagnetic waves generated in the frequency conversion can be written using equation (1.12) as follows[13]:

$$\alpha_1' E_1^* + \frac{\partial E_1^*}{\partial z} = -i \kappa_1 E_3^* E_2 e^{-i \Delta k z} \tag{1.14a}$$

$$\alpha_2' E_2 + \frac{\partial E_2}{\partial z} = -i \kappa_2 E_3 E_1^* e^{i \Delta k z} \tag{1.14b}$$

where,

$$\kappa_i = \frac{\omega_i d_{eff}}{n_i c}$$

$$d_{eff} = \frac{\chi^{(2)}_{eff}}{2}$$

$$\alpha_i' = \frac{\alpha_i}{n_i}$$

The solutions of the electromagnetic fields described by equations (1.14) given by Byer[14] are:

$$E_1^*(z) = E_{10}^* \, e^{(\Gamma' - i\frac{\Delta k}{2})z} \tag{1.15a}$$

$$E_2(z) = E_{20} \, e^{(\Gamma' + i\frac{\Delta k}{2})z} \tag{1.15b}$$

Substituting these solutions into equations (1.14) values for the complex gain, Γ', can be obtained by solving the resultant determinantal equation. The values obtained in this fashion are:

$$\Gamma_{\pm}' = -\frac{(\alpha_1' + \alpha_2')}{2} \pm \frac{1}{2}\sqrt{(\alpha_1' - \alpha_2')^2 + i\frac{\Delta k}{2}(\alpha_1' - \alpha_2') - 4\left(\frac{\Delta k}{2}\right)^2 + 4\frac{\omega_1 \omega_2 |d_{eff}|^2 |\vec{E}_3|^2}{n_1 n_2 c^2}} \tag{1.16}$$

It is useful to define the following gain parameter:

$$\Gamma^2 = \frac{\omega_1\,\omega_2\,|d_{eff}|^2\,|\vec{E}_3|^2}{n_1\,n_2\,c^2} = \kappa_1\,\kappa_2\,|\vec{E}_3|^2 = \frac{\omega_1\,\omega_2\,|d_{eff}|^2\,I_3}{n_1\,n_2\,\varepsilon_0\,c^3} \qquad (1.17)$$

The simple coupled solutions, assuming $\alpha = \alpha_1' = \alpha_2'$ are:

$$\vec{E}_1^*(z) = (\,\vec{E}_{1+}^*\,e^{gz} + \vec{E}_{1-}^*\,e^{-gz}\,)\,e^{-\alpha z}\,e^{-i\Delta kz/2} \qquad (1.18a)$$

$$\vec{E}_2(z) = (\,\vec{E}_{2+}\,e^{gz} + \vec{E}_{2-}\,e^{-gz}\,)\,e^{-\alpha z}\,e^{i\Delta kz/2} \qquad (1.18b)$$

where,

$$g = \sqrt{\Gamma^2 - \left(\frac{\Delta k}{2}\right)^2} \qquad (1.19)$$

Assuming background electromagnetic fields of $\vec{E}_1^*(z=0)$ and $\vec{E}_2(z=0)$, and performing a little algebra, the following equation describing the generated electromagnetic radiation emitted from the frequency converter using a crystal of length l is obtained for $E_1(l)\,e^{\alpha l}$[15]:

$$E_1(l)\,e^{\alpha l} = E_1(0)\,e^{i\,\Delta kl/2}\left[\,\cosh gl - i\,\frac{\Delta kl}{2g}\sinh gl\,\right] + i\kappa_1\frac{E_3}{g}\,E_2^*(0)\,e^{i\,\Delta kl/2}\sinh gl \qquad (1.20)$$

and similarly for $E_2(l)\ e^{\alpha l}$.

From elementary considerations, the maximum pump power converted into signal and idler wave power during single pass parametric frequency (OPA) conversion should never exceed 50%. This maximum conversion is caused by recombination of the signal and idler waves into the original pump wave along the length of the crystal. Eventually the creation and annihilation of the generated waves become equal in magnitude and the net conversion becomes zero thus limiting the maximum pump power depletion to 50 % of the original value.

Many theoretical models describing the expected field intensities at the output end of optical parametric oscillators (OPO's) have been published[16-21]. According to Kreuzer's calculations[22], it should be possible to obtain 100% parametric frequency conversion for a singly resonant optical parametric oscillator. This assumes appropriate coupling of the waves with the resonator while pumping with a uniform plane-wave beam. It is not possible to have such a situation in practice since the profile of most lasers is TEM_{00} in profile and never exceeds 1 or 2 mm in diameter. The largest experimental conversion efficiency quoted in the literature is 45%[2].

When Bjorkholm took into account the Gaussian nature of the pump beam, calculations revealed that a maximum conversion efficiency of 71% was achievable[17]. Unfortunately these results are only valid for a beam waist having a radius larger than $\omega_0 \geq$ 0.12 cm and for a double refraction angle, $\rho = 0°$, as explained in the article. This result is

therefore not useful for the vast majority of experiments.

This covers the theoretical results which are deemed pertinent for the interpretation of the experimental values which will be presented later in the thesis. As mentioned in this chapter, there are many characteristics of the parametric frequency conversion process which require specific knowledge of the various properties of material mediating this physical phenomena. The next chapter is therefore devoted to discussing these properties.

Chapter 2

$LiNbO_3$

This chapter is devoted to a discussion of the properties of $LiNbO_3$ which are used in the frequency conversion process. To start with a simple model is used to show how a material can possess more than one index of refraction for a particular wavelength. This latter property allows the phase-match conditions to be satisfied using different scenarios depending on the crystal birefringence. These different scenarios are described and the one used in the system is pointed out. In order to obtain theoretical predictions of the wavelengths satisfying the phase-match conditions, the Sellmeier equations describing the temperature and wavelength dependence of the index of refraction are given. Another important property of $LiNbO_3$ which must be known is the value of the effective nonlinear coefficient. The form of this coefficient, determined by taking into consideration the particular orientation of the crystal axes, is obtained at the end of the chapter.

Lithium Niobate, a crystal belonging to the 3m crystal class[23], is transparent in the 0.35 to 4.5 μm range[24]. This material is very useful in the

frequency conversion process since it has a very large 2nd order nonlinear susceptibility as well as sufficiently large birefringence ($\Delta n = n_e - n_o$). The difference in refractive indices is sufficient to allow equations (1.11) to be satisfied for a very broad pump spectral range. By changing the crystal temperature, orientation and/or the pump frequency, it is possible to tune the generated parametric frequencies over the entire crystal transparency range. This tunability is directly linked to the dependence of the indices of refraction on these same parameters.

The properties of the crystal responsible for the different indices of refraction can be described by a simple mechanical model. The model consists of approximating the binding forces between the different atoms and the surrounding electron cloud by springs. Since the binding forces between atoms and electrons in the crystal lattice are usually direction dependent, the crystal will possess indices of refraction which are direction and electromagnetic wave polarization dependent. A simple illustration of such a model is shown in figure 2.1 in which the binding forces between atoms and the electrons (similar in behaviour to springs) are shown from the principal axes point of view[25].

The frequency dependent index of refraction can be obtained by considering a driven damped oscillator model for the electrons bound in a medium interacting with an electromagnetic wave. The resonant frequencies of the oscillators, corresponding to spectroscopic transitions, determine the exact character of the indices of refraction. Since the resonant frequencies of the oscillators of the model shown in figure 2.1 are direction dependent, so are the indices of refraction of the

medium.

In the case of $LiNbO_3$, the crystal anisotropy is such that only two independent force constants (usually possessing different transition frequencies) are necessary to describe the crystal indices of refraction. That is, the index of refraction along any direction can be described by two independent indices of refraction. This crystal is therefore a member of the uniaxial crystal class.

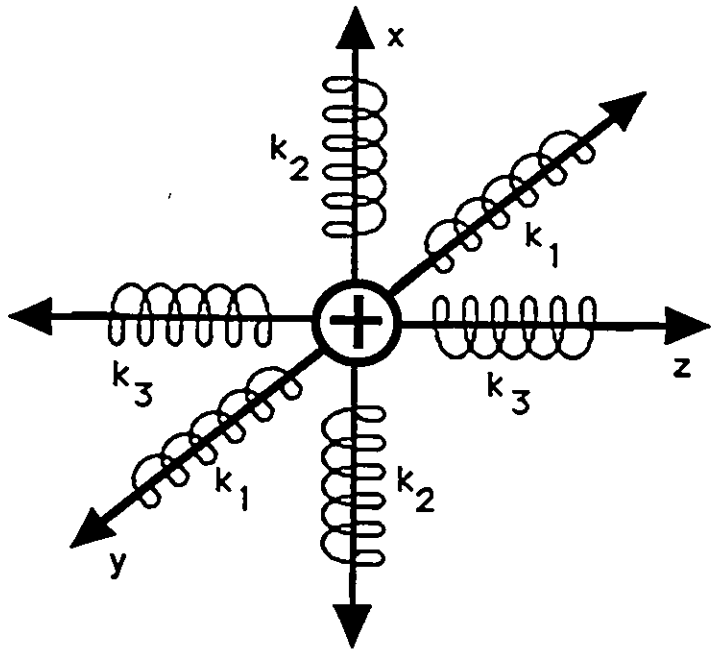

Figure 2.1. Spring representation of the binding forces in crystals.

The indices of refraction for $LiNbO_3$ can be described if $k_1 = k_2$ is assumed in the model shown in figure 2.1. With this constraint, the velocity of a wave propagating in the z-direction will be constant and described by the polarization

independent index of refraction. Now for a wave propagating in the x- or y-direction, the velocity will not be constant. Rather it will be described by an index of refraction having a value dependent on the orientation of the polarization vector with respect to the z-direction.

In this case the z-axis was chosen to be parallel to the optic axis. The optic axis, also called the c-axis, is defined by the direction for which the index of refraction is polarization independent. The dependence of the index of refraction on the polarization in a uniaxial crystal such as $LiNbO_3$ can be shown diagrammatically as in figure 2.2[26]. The diagram depicts the indices of refraction for a crystal possessing a negative birefringence. The small circles represent a wave having the polarization vector perpendicular to the plane defined by the paper, whereas the double ended arrows represent the case in which the polarization vector is parallel to the plane of the paper. As is depicted in figure 2.2, the index of refraction governing the behaviour of a wave having a polarization vector parallel to the plane of the page is described by the following equation[27]:

$$\frac{1}{n^e(\theta)} = \sqrt{\frac{\sin^2\theta}{n_e^2} + \frac{\cos^2\theta}{n_o^2}} \qquad (2.1)$$

Where the angle θ is measured with respect to the z-axis. The behaviour of the waves having a polarization vector perpendicular to the plane of the paper are governed by the ordinary index of refraction having a constant value, n_0. A crystal for which the birefringence, Δn, is positive is said to be positive uniaxial, and one

for which the birefringence is negative is said to be negative uniaxial.

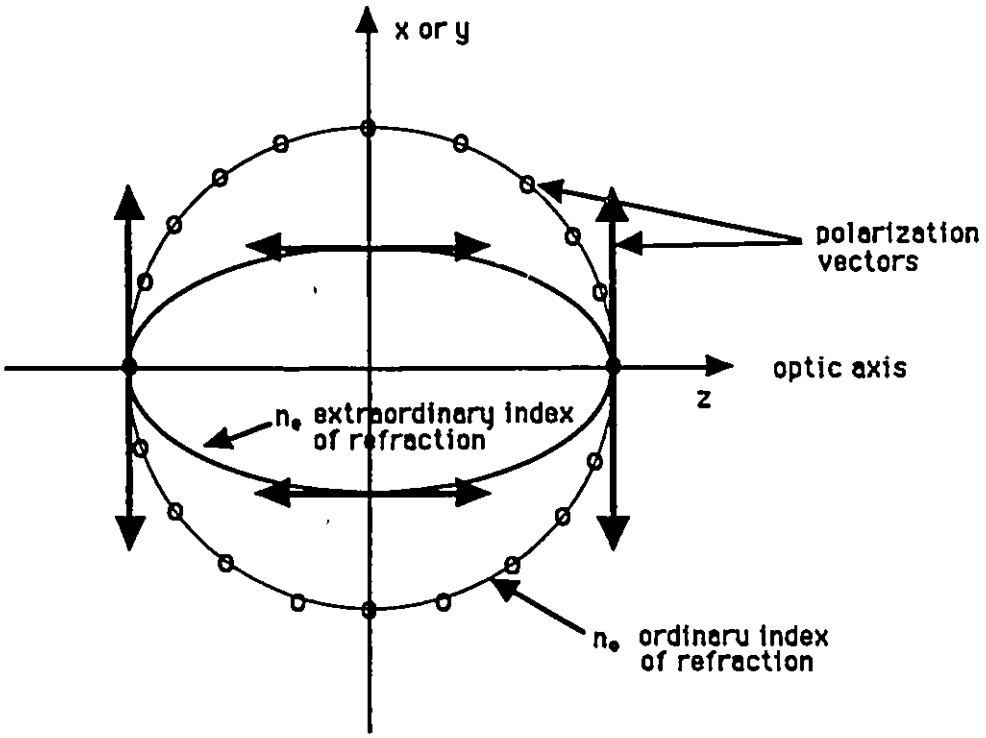

Figure 2.2. r-θ graph of n_o and n_e as a function of θ.(The direction of propagation being perpendicular to the wave polarization).

As pointed out in the preceding paragraph, the value of the birefringence allows the distinction between two different crystal types. It is therefore possible to satisfy equations (1.13) in different ways for different crystal types. In order to determine the possible ways of satisfying these equations, it is useful to rewrite equation (1.13b) in the following form:

$$\frac{n_p \omega_p}{c} = \frac{n_s \omega_s}{c} + \frac{n_i \omega_i}{c} \qquad (2.2)$$

(p = pump, s = signal, and i = idler)

By making use of the various permutations of the crystal indices of refraction n_o and n_e while taking into consideration the crystal type reveals that only the following types of phase-matching are possible[28]:

Type I (negative birefringence):

$$n_{e_p}(\omega_p)\,\omega_p = n_{o_s}(\omega_s)\,\omega_s + n_{o_i}(\omega_i)\,\omega_i \qquad (2.2a)$$

Type I (positive birefringence):

$$n_{o_p}(\omega_p)\,\omega_p = n_{e_s}(\omega_s)\,\omega_s + n_{e_i}(\omega_i)\,\omega_i \qquad (2.2b)$$

Type II (negative birefringence):

$$n_{e_p}(\omega_p)\,\omega_p = n_{e_s}(\omega_s)\,\omega_s + n_{o_i}(\omega_i)\,\omega_i \qquad (2.2c)$$

or $$n_{e_p}(\omega_p)\,\omega_p = n_{o_s}(\omega_s)\,\omega_s + n_{e_i}(\omega_i)\,\omega_i \qquad (2.2d)$$

Type II (positive birefringence):

$$n_{o_p}(\omega_p)\,\omega_p = n_{e_s}(\omega_s)\,\omega_s + n_{o_i}(\omega_i)\,\omega_i \qquad (2.2e)$$

or $$n_{o_p}(\omega_p)\,\omega_p = n_{o_s}(\omega_s)\,\omega_s + n_{e_i}(\omega_i)\,\omega_i \qquad (2.2f)$$

where $n_{e_k}(\omega_k) = n_{e_k}(\omega_k,\theta,T)$ and $n_{o_k}(\omega_k) = n_{o_k}(\omega_k,T)$.

Type I phase-matching is used by the system to satisfy equations (1.13) since $LiNbO_3$ is a negatively birefringent material. It will be shown later that the

effective nonlinear coefficient of $LiNbO_3$ is zero for type II phase-matching. The crystal orientation used in the frequency conversion process must be chosen in a way that allows the use type I phase-matching. For most crystals the incident pump wave and the generated signal and idler waves do not propagate in the same direction. In the case of $LiNbO_3$ it is possible to obtain collinear propagation of the beams since equation (2.2a) can be satisfied for $n_{e_i}(\theta)$ with $\theta = 90°$ by changing the crystal temperature. This type of phase-matching is commonly referred to as 90° phase-matching.

Analytic forms describing the temperature and wavelength dependence of the index of refraction were used to determine the exact wavelengths for which equations (1.13) can be satisfied. These equations are commonly referred to as the Sellmeier equations of the indices of refraction. Since the resulting equations are not linear, a computer program was used to determine the values of the signal and idler waves consistent with fixed values of the pump wavelength. The program that was developed and used for solving the phase-match conditions is listed in Appendix III. The following Sellmeier equations describing the indices of refraction of congruently grown $LiNbO_3$ were used in the program[29]:

$$n_o(\lambda,T)^2 = 4.9048 + \frac{1.178 \times 10^5 + 2.3416 \times 10^{-2} F}{\lambda^2 - (2.1802 \times 10^2 - 2.9671 \times 10^{-5} F)^2} - 2.7153 \times 10^{-8} \lambda^2 + 2.1429 \times 10^{-8} F \quad (2.3a)$$

$$n_e(\lambda,T)^2 = 4.5820 + \frac{0.9921 \times 10^5 + 5.2716 \times 10^{-2} F}{\lambda^2 - (2.1090 \times 10^2 - 4.9143 \times 10^{-5} F)^2} - 2.1940 \times 10^{-8} \lambda^2 + 2.2971 \times 10^{-7} F \quad (2.3b)$$

In these equations $F = (T-T_0)(T + T_0 + 546)$ with $T_0 = 24.5$ °C and λ in nm. There are many references containing the values of the indices of refraction for the different compositions of $LiNbO_3$[29-35].

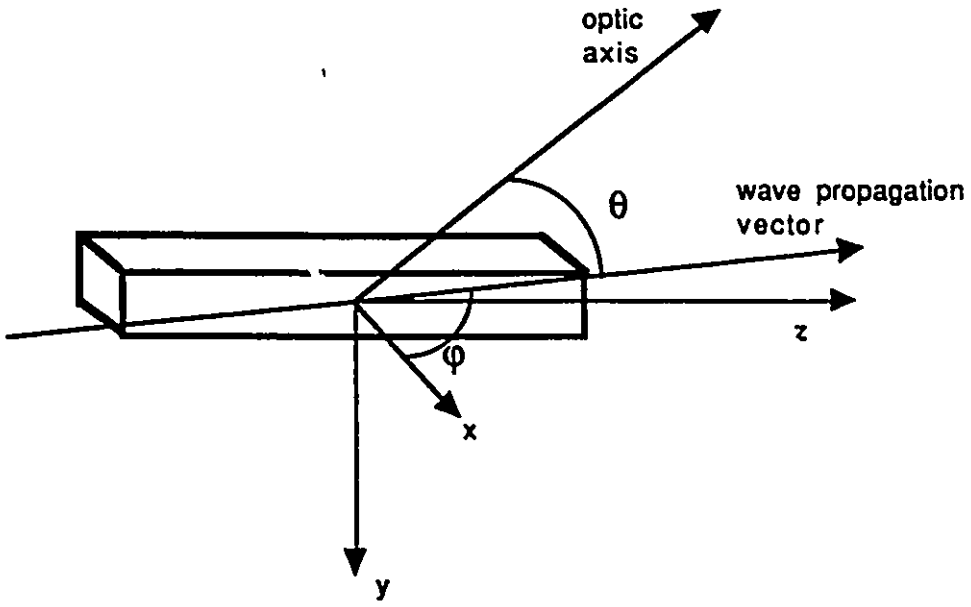

Figure 2.3. Orientation of the electromagnetic wave propagation vector and polarization orientation with respect to the crystal orientation.

The second order nonlinear susceptibility tensor determining the amount of coupling between the crystal polarizability and the electromagnetic field is given as[36]:

$$d^{(2)}_{jkl}(-\omega_p, \omega_s, \omega_i) \text{ which equals } 1/2\ \chi^{(2)}_{jkl}(-\omega_p, \omega_s, \omega_i) \qquad (2.4)$$

in the literature[37-40]. Once the crystal orientation is chosen for the particular experimental arrangement it is possible to define an effective nonlinear coefficient (d_{eff}). In order to obtain this expression it is necessary to know the angle of propagation of the waves with respect to the optic axis as well as the orientation of their polarization with respect to the latter. These particular angles are shown in figure (2.3). The following expression is obtained for the effective nonlinear coefficient of $LiNbO_3$ by using the nonlinear susceptibility tensor in conjunction with the equations describing the different electromagnetic waves[41]:

$$d_{eff} = d_{31} \sin\theta - d_{22} \cos\theta \sin 3\varphi \qquad (2.5)$$

From experimental results Harris has determined that d_{eff} is approximately frequency independent[16]. Since the angle $\theta = 90°$, only the value of d_{31} (= 6.25 x 10^{-12} m/V given by Byer[42]) is necessary to determine the effective nonlinear coefficient. This last bit of information allows equation (2.5) to be reduced to the following form:

$$d_{eff} = d_{31} \qquad (2.6)$$

The last important property of $LiNbO_3$ concerns the input intensity causing damage to the nonlinear material and is referred to as the damage threshold. The latter should be higher than the threshold input intensity required to produce frequency conversion. Many references give values for the damage threshold of $LiNbO_3$[2, 5, 10]. The smallest value given is 8 MW/cm^2 [5] and the largest value is

150 MW/cm^2 [2, 10, 43]. In the case of the last reference[43], the value is given for a 1/4 wavelength dielectric layer of Al_2O_3 used to antireflection coat the particular $LiNbO_3$ crystal.

The $LiNbO_3$ properties presented in this chapter allow some comparison between theoretical and experimental results. The next chapter is devoted to a description of the particular experimental arrangements used to map out the characteristics of the frequency conversion system. A description of the equipment used to accomplish each task is also included.

Chapter 3

Experimental Setup and Equipment

In the last chapter we described the different crystal properties that are utilized in the frequency conversion system. Now we are ready to describe the experimental layout and equipment used to generate near-infrared laser radiation. The near-infrared laser radiation was produced by frequency conversion of the output radiation from a dye laser in an $LiNbO_3$ crystal. This dye laser was pumped by a 532 nm laser beam produced by frequency doubling of the 1064 nm output from an Nd:YAG laser. The equipment used will be described briefly when the measurements of the different physical characteristics of the infrared radiation and the output for the different pump lasers are discussed.

As mentioned in the previous paragraph, near-infrared radiation was produced by frequency conversion of the dye laser beam within an $LiNbO_3$ crystal. The frequency conversion process would only occur once the input power was sufficient to offset the system losses. The system was designed to use 90° phase-matching between the pump and the generated waves. This type of phase-matching maximizes frequency conversion since long coherence lengths between the incident and generated waves are achieved. Under these conditions, the velocities of the generated waves within the crystal are described by

the ordinary index of refraction while the velocity of the pump wave is described by the extraordinary index of refraction. In this setup the frequency weighted average velocity of the generated waves is the same as that of the pump wave. The orientation of the different wave polarizations imposed by the phase-matching are shown in figure (3.1) with respect to the crystal shape and its optic axis.

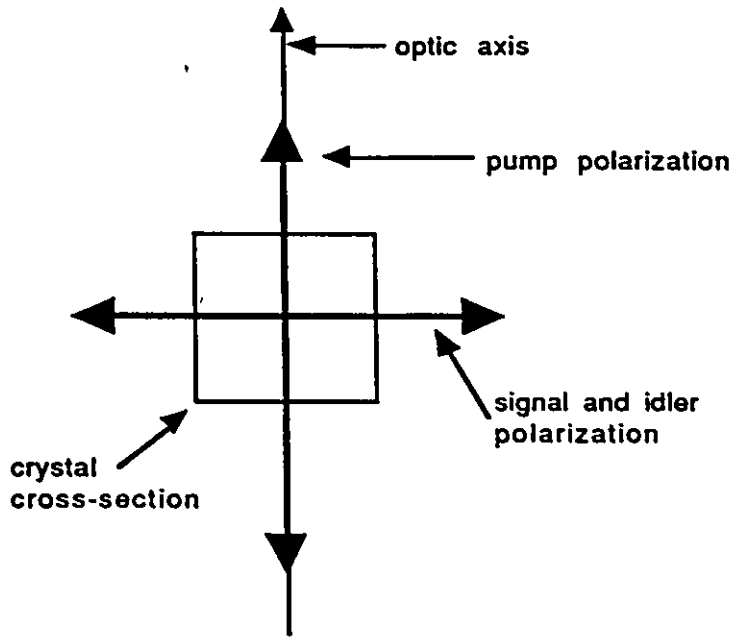

Figure 3.1. Orientation of the polarization vectors of the waves involved in the frequency conversion process (beams are propagating perpendicular to the plane of the paper).

A total of five crystals were used to produce near-infrared frequency conversion. Of these, four were manufactured by Union Carbide in 1990. The other crystal was provided by Chromatix Inc. with their frequency conversion system in the late 1970s. All of the crystals had approximately the dimensions shown in figure (3.2). The end faces of all the crystals are antireflection hard coated at 600 nm in order to maximize cross medium coupling at the pump wavelengths. Previous experiments have shown that this coating

increases the damage threshold of the crystalline material[43]. The oven used to house the crystals is open ended. The oven temperatures can be set to different values in the 225 to 450 °C range. The oven gap is designed to be closely fitting around the crystal. This oven design minimizes temperature gradients within the crystal by reducing the amount of cooling due to convection.

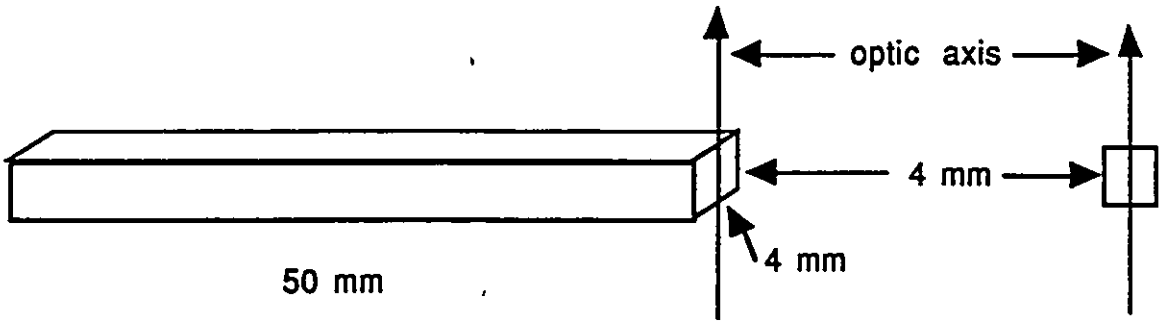

Figure 3.2 Dimensions of the $LiNbO_3$ crystals.

The population inversion within the dye is produced by exposing it to the 532 nm laser beam. This laser beam was obtained from the frequency doubling of the 1064 nm beam produced by an Nd:YAG laser. The stimulated emissions from the dye are resonated in order to produce coherent radiation over a very small spectral bandwidth. Kiton Red (KR620), the dye used in this experimental setup, allows the production of tunable laser radiation in the 584 to 610 nm range. The peak conversion efficiency of the dye occurs around 592.5 nm. The pulses have a 10 ns FWHM length and occur at a rate of 10 pulses per second. The output from the dye laser is vertically polarized and can attain peak output powers as high as 3.76 MW. This peak power corresponds to 400 mW of average power and a 4.8 TW/m^2 peak intensity. The dye beam is 1 mm in diameter at the output with a 0.5 mrad divergence. At a distance of 5 m, the dye beam is oval in cross-section with a

major to minor axis ratio of 2:1. This oval shape implies that some focusing of the beam has been performed in order to have a circular beam in the near field of the dye laser. Since the laser beam behaves in this fashion, the experiment was setup very near the output end of the dye laser.

In order to obtain maximum frequency conversion, the crystal optic axis and the dye laser polarization were aligned parallel to one another. The pump beam was directed along the length of the crystal and centred on the endfaces (see figure 3.1). The different components of the system were set up as shown in figure (3.3). A filter was placed at the output end of the frequency converter in order to reject the portion of the pump beam transmitted through the crystal. The type of phase-matching used in the experiment also allows the pump beam to be rejected from the output by using a polarizer.

The output power from the dye laser was measured at position 1 with a volume absorbing power meter while the output power of the infrared waves was measured at position 2 with the same unit (see figure 3.3). Optimization of the infrared radiation output power level was achieved by small adjustments of the crystal orientation with respect to the pump beam. A tentative examination of the beam profile was done with the help of an infrared fluorescence card. The profile appeared to be nearly TEM_{00} Gaussian in nature. This card was very useful for locating the infrared beam and for the initial adjustments of the crystal orientation so that the output was roughly TEM_{00} in profile.

The near-infrared wavelengths were measured with a 0.125 m spectrometer in conjunction with a pyroelectric detector. These components were placed at position 2 as shown in figure (3.3). Frequency conversion of the pump beam was possible for the entire dye wavelength range satisfying the phase-match conditions for crystal temperatures

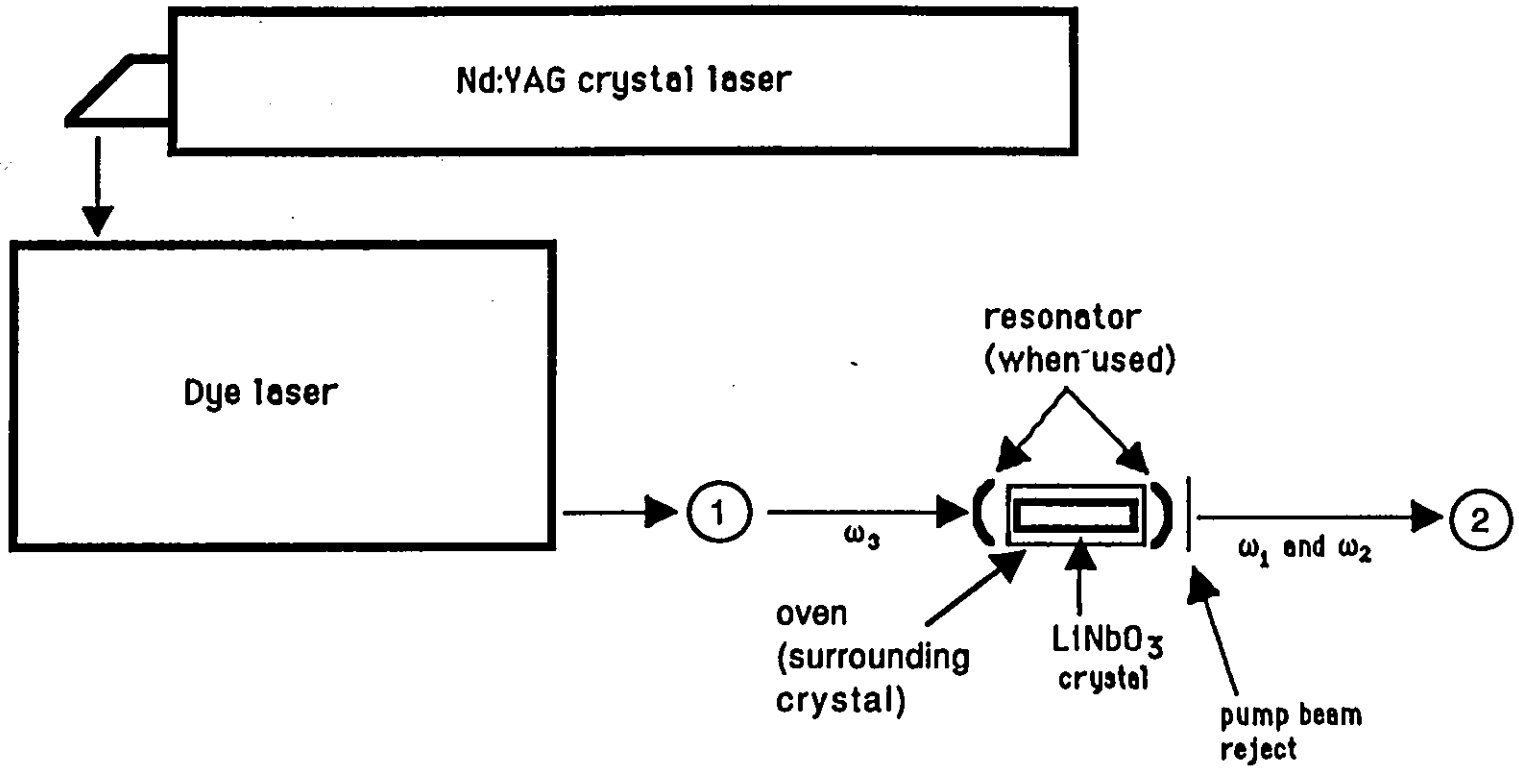

Figure 3.3 System setup and position of removable equipment.

between 225 °C and 450 °C. The experiment was only performed at 25 C° intervals in this temperature range. Using these temperature intervals, the production of near-infrared radiation from 0.734 to 2.853 μm was possible.

The spatial profile of the generated signal wave was mapped out while operating the frequency converter in the optical parametric oscillator configuration. This mapping was done by measuring the output radiation in a grid like fashion using a pinhole/detector arrangement at position 2 indicated in figure 3.3. A scan in the x and y directions was performed on a 21 x 21 cell grid. The two strips examined are shown in figure 3.4. The pinhole assembly was placed 23.5 cm from the end face of the output mirror. A lens was used to defocus the transmitted portion of the infrared beam in order to avoid damaging the pyroelectric detector.

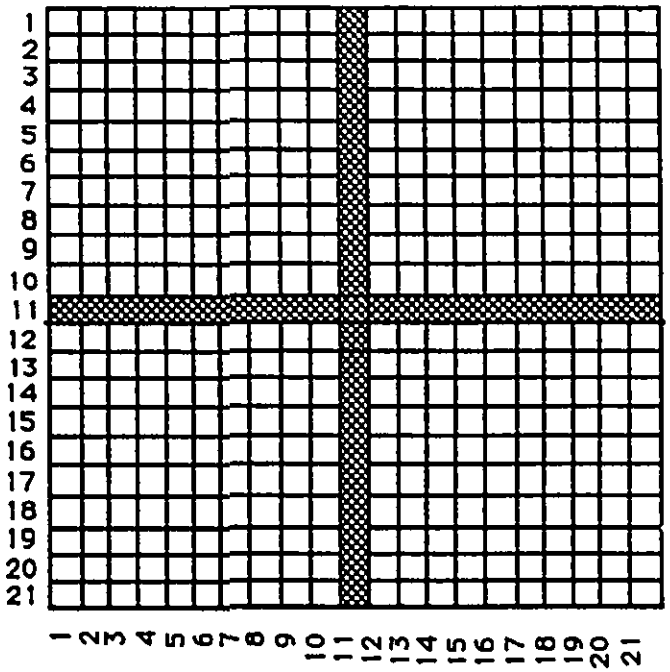

Figure 3.4. Section of the output infrared signal wave profile examined with the pinhole detector.

The temporal behaviour of the pump and signal waves were measured at positions 1 and 2, respectively, as shown in figure 3.3. In order to avoid saturating the subnanosecond diode detector used for these measurements, neutral density filters were placed in the beam paths. The subnanosecond detector output was passed through a boxcar signal averager equipped with a subnanosecond signal input head. The output from the boxcar was then used to reconstruct the average temporal behaviour of the pump and signal waves with 1 ns of resolution.

In order to obtain the crystal damage threshold, the input power of the dye laser was slowly increased from the threshold value. The output power produced by frequency conversion was monitored for sudden decreases in power with an increase in input power. The output power observed just before the crystal began to damage remained at a fixed value for a couple of seconds, and then it suddenly dropped by 40 %. The onset of damage was accompanied by a sparking noise. The sparking noise was deduced to be emanating from the point where the crystal was undergoing damage. Later inspection of the crystal confirmed this deduction. This experiment was only performed once using a 592.5 nm pump wavelength and a 275 °C crystal temperature. This pump wavelength was chosen near the peak conversion efficiency of the dye laser, whereas the crystal temperature was arbitrarily chosen at a value below 300 °C.

The experiment described in the previous paragraph revealed that using the maximum dye laser output would inevitably damage the crystal. Since the Nd:YAG pump laser works most efficiently when the driving flashlamp operates at the optimum voltage, the dye beam was expanded prior to directing it through the $LiNbO_3$ crystal. This expansion of the dye laser beam reduced the peak intensity to a value below that of the crystal damage threshold. A factor of four increase in area was calculated to be sufficient to

decrease the pump beam intensity below the damage threshold. A 2 x beam expander was built for this purpose and placed at position 1 as shown in figure 3.3. The expander consisted of 2 converging lenses having different focal lengths, a 10 cm and a 20 cm one. These lenses were placed 30 cm apart (= $f_1 + f_2$), as shown in figure 3.5, in order to achieve this 2 x expansion.

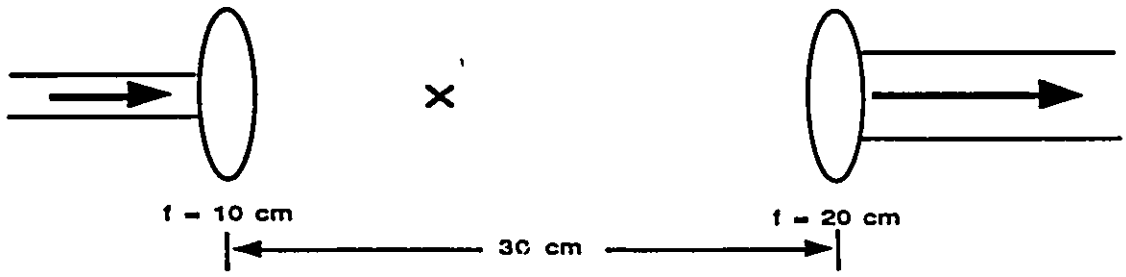

Figure 3.5. Beam expansion setup which allowed full pump power to be used in the frequency conversion process.

This concludes the description of the experimental setups and equipment used to perform the different experiments. The next three chapters will present the results obtained from these experiments.

This page left blank.

This page left blank.

Chapter 4

Tuning Curves

In this section the experimental tuning curves obtained from frequency conversion in congruently grown $LiNbO_3$ are presented. The tuning curves which are presented were obtained for the crystal provided by Chromatix Inc. The tuning curves for the other crystals were also examined briefly, but they were not found to be significantly different from those of the Chromatix crystal. The Chromatix crystal experimental tuning curves are also compared with theoretical tuning curves for congruently grown $LiNbO_3$.

The experimental tuning curves obtained while mapping out the characteristics of parametric frequency conversion are presented in figure 4.1. These curves were obtained by using a 0.125 m spectrometer and a pyroelectric detector. The wavelengths that were measured spanned the 0.734 to 2.853 μm range. These curves were obtained for pump wavelengths from 584 to 610 nm while keeping the crystal at fixed temperatures. The crystal temperatures that were used to alter the phase-matched wavelengths spanned the 225 to 425 °C range at 25 C° intervals. These temperatures are the dial temperatures and are a little different than the true temperatures. The temperatures measured with a thermocouple

Figure 4.1. Experimental Tuning Curves for Congruently Grown $LiNbO_3$ at Different Temperatures.

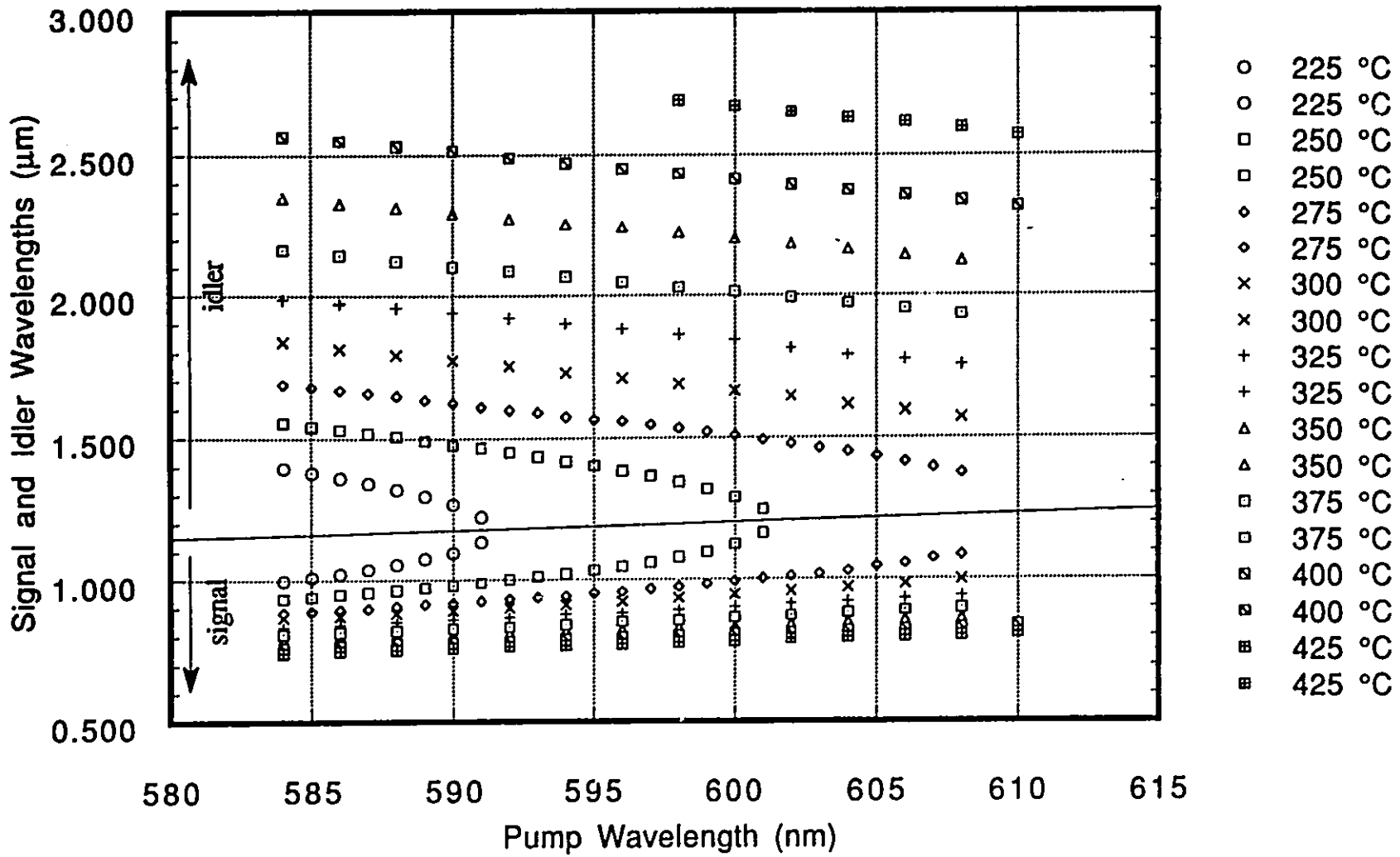

Table 4.1. Dial, measured and best fit temperature cross reference table.

Dial Temperature (°C)	Measured Temperature (°C)	Best Fit Temperature (°C)
225	227.2	226.2
250	252.4	252.4
275	277.1	277.1
300	301.7	301.7
325	326.9	327.5
350	351.6	351.6
375	376.3	376.3
400	401.3	401.3
425	426.3	426.3
450	451.2	451.2

are shown in table 4.1 for comparison. The shape of the tuning curves appears to be quadratic in nature, unfortunately there is some deviation from this shape. An examination of the tuning curves at 225 °C and 250 °C reveals that they do not span the entire pump wavelength range. This restriction to the lower wavelengths of the pump wavelength range arises since the phase-match conditions (1.13) cannot be satisfied above certain pump wavelengths. The wavelengths of the generated waves for temperatures above 425 °C could not be measured above a certain value because of the limitations of the spectrometer/detector. It was no longer possible to examine frequency conversion process for crystal temperatures above 425 °C since the gain coefficient of and the temperature gradient within the crystal were sufficient to inhibit the process.

The theoretical tuning curves for congruently grown $LiNbO_3$ are shown in figure 4.2. The tuning curves are shown for the accessible pump wavelengths and the crystal temperatures maximizing agreement with the experimental tuning curves. Table 4.1 contains the best fit temperatures used to obtain the theoretical tuning curves. These theoretical tuning curves were obtained by solving the phase-match conditions (1.13) for the two unknown wavelengths while holding the third wavelength at a fixed value. Although it may be possible to solve the phase-match equations analytically, a computer program (see Appendix III) was used to obtain the values of the two unknown wavelengths. This approach was deemed appropriate since the equations appear to show strong coupling between the values of the different wavelengths involved in the frequency conversion process. The program solved for these wavelength values by using the Sellmeier equations for the indices of refraction which can be manipulated into a fourth power equation in the λ variable. The tuning curves obtained using the computer program appear to have the same general shape as those contained in figure 4.1.

In order to compare the theoretical and experimental curves, the signal wavelengths have been shown separately from those of the idler wavelengths. Figure 4.3 shows the experimental and theoretical values of the signal wavelengths as a function of the pump wavelength and figure 4.4 shows the values of the idler wavelengths as a function of the pump wavelength. The differences between the theoretical and experimental values of the signal and idler wavelengths are very small. These differences never exceed 0.01 μm and usually lie in the 0.002 to 0.003 μm range for both the signal and idler waves. Based on these small differences it was concluded that the congruently grown crystal provided by Chromatix Inc. was of very good quality.

Figure 4.2. Theoretical tuning curves for congruently grown $LiNbO_3$ at different temperatures.

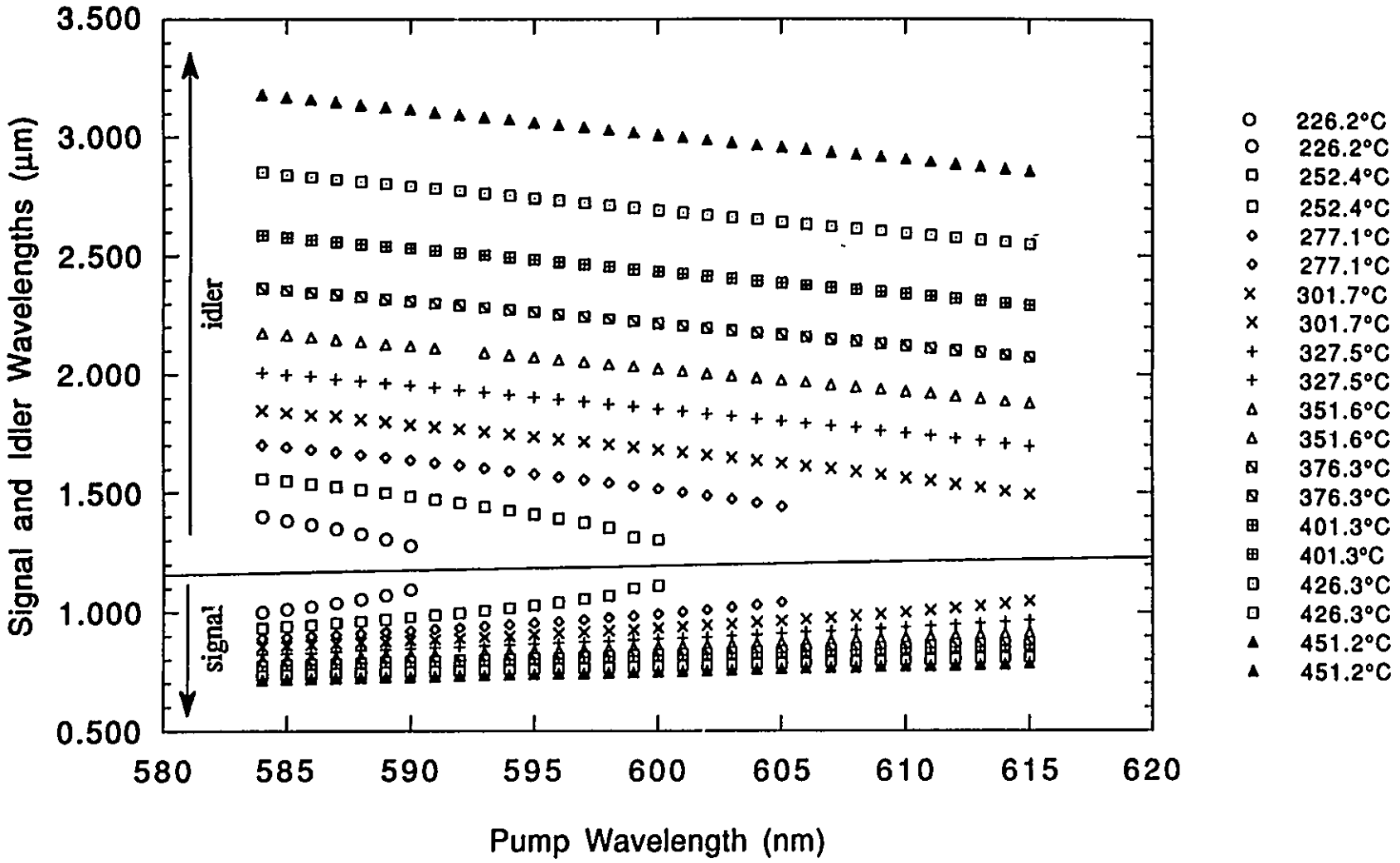

Figure 4.3. Comparison of the theoretical and experimental tuning curves at the signal wavelength for congruently grown $LiNbO_3$.

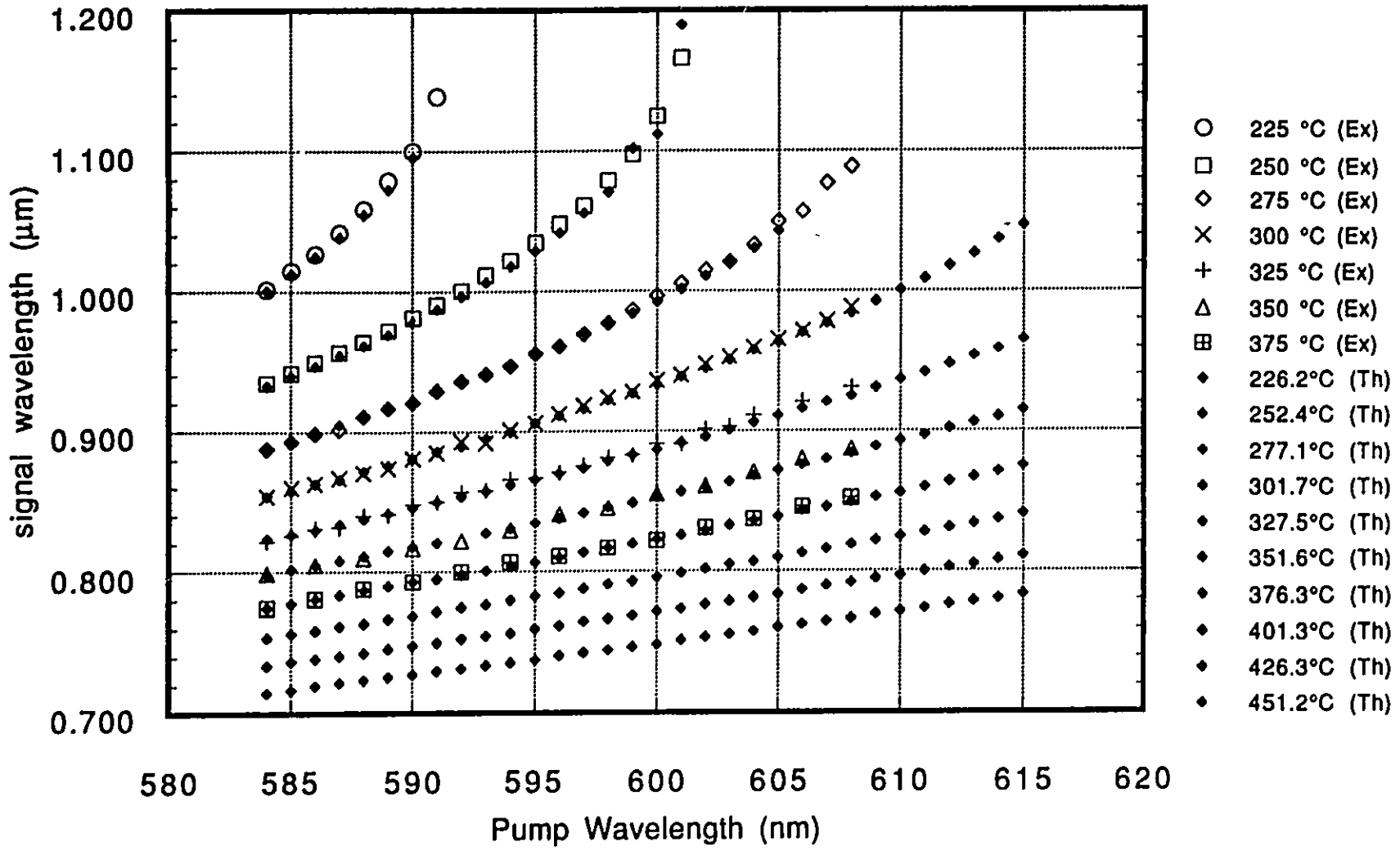

Figure 4.4. Comparison of the theoretical and experimental tuning curves at the idler wavelength for congruently grown $LiNbO_3$.

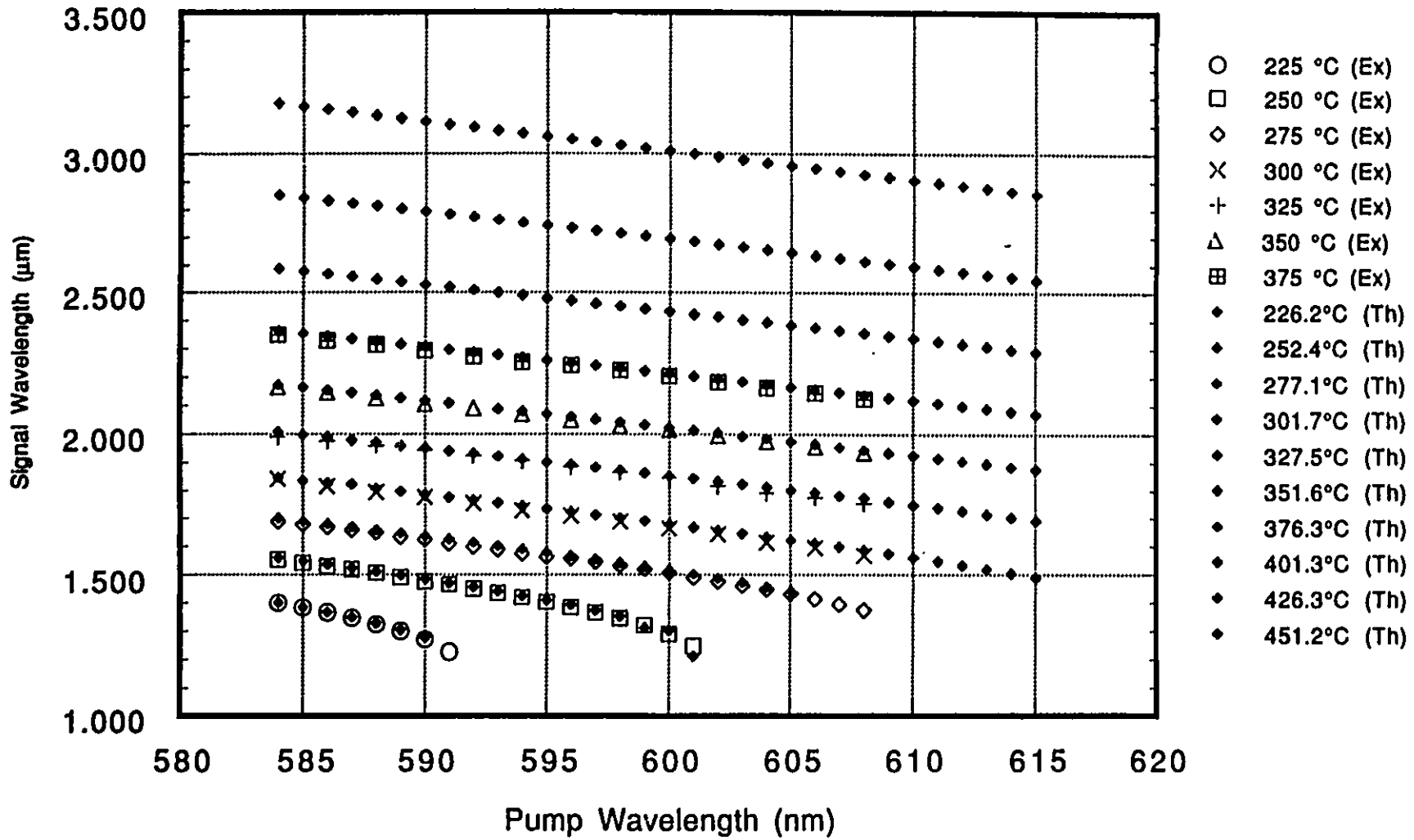

The tuning curves of the other four crystals were examined and found to differ by a couple of nanometres from the ones presented here. The next chapter presents the results obtained while operating the system as an optical parametric oscillator.

Chapter 5

OPO Operation

The different factors influencing the output power during optical parametric oscillator (OPO) operation are examined in this chapter. The factors examined include the influences of the temperature, pump wavelength, input power and the mirror reflectivity coefficients. An examination of the spatial and temporal profile of the output wave as well as the mirror damage threshold is also presented.

Optical parametric oscillator operation makes use of a resonator in order to enhance parametric frequency conversion. In this particular case a singly resonant oscillator is used to enhance the frequency conversion of the signal wave. This enhancement is achieved by using mirrors highly reflecting at the generated idler wavelength in the resonator cavity design. The mirrors allow very high intensities of the idler wave to buildup within the cavity. As the power builds up at the idler wavelength, the level becomes comparable to that of the pump wave power. This buildup of power thus allows the pump wave to be preferentially converted into signal wave power. Losses which can occur at the different wavelengths during this conversion process have been ignored.

A. Variation of the Output Power Produced by the OPO Using a Constant Input Power

The following figures show the typical behaviour of the output power at a constant 60 mW average input power as a function of the signal wavelength observed during optical parametric oscillator operation. This behaviour was examined at several temperatures. In order to convert to peak powers, the average power must be multiplied by 0.94×10^7, for instance 10 mW of average power corresponds to 0.94×10^5 Watts peak (see Appendix II).

The following set of figures, 5.1-5.4, shows the variation of the output power for a set of mirrors highly reflecting in the 1.20 to 1.55 μm wavelength region (Mirrors IR1). Results for different sets of mirrors are also similar in nature to these results and are therefore not shown here in order to avoid redundancy. The maximum average output power of 18 mW was observed for a crystal temperature of 275 °C (figure 5.3) while pumping the resonator at 597 nm (30% efficiency). This pump wavelength resulted in the production of signal radiation at $\lambda = 0.958$ μm.

The variation of the output power at the different signal wavelengths is shown in figure 5.1 for a 225 °C crystal temperature along with the mirror transmission curve. The behaviour of the output power closely follows the transmission coefficient of the mirror. This modulation of the output power by the mirror transmission is expected since the idler wavelengths generated with the signal waves are produced in the 1.20 to 1.55 μm range. The maximum average observed output power of 13.5 mW occurred for a 590 nm pump wavelength. This resulted in production of infrared radiation with $\lambda = 1.097$ μm.

Figure 5.1. Average output power of the optical parametric oscillator using mirrors highly reflecting in the 1.20 to 1.55 μm wavelength range for a 225 °C crystal temperature and 60 mW of input power.

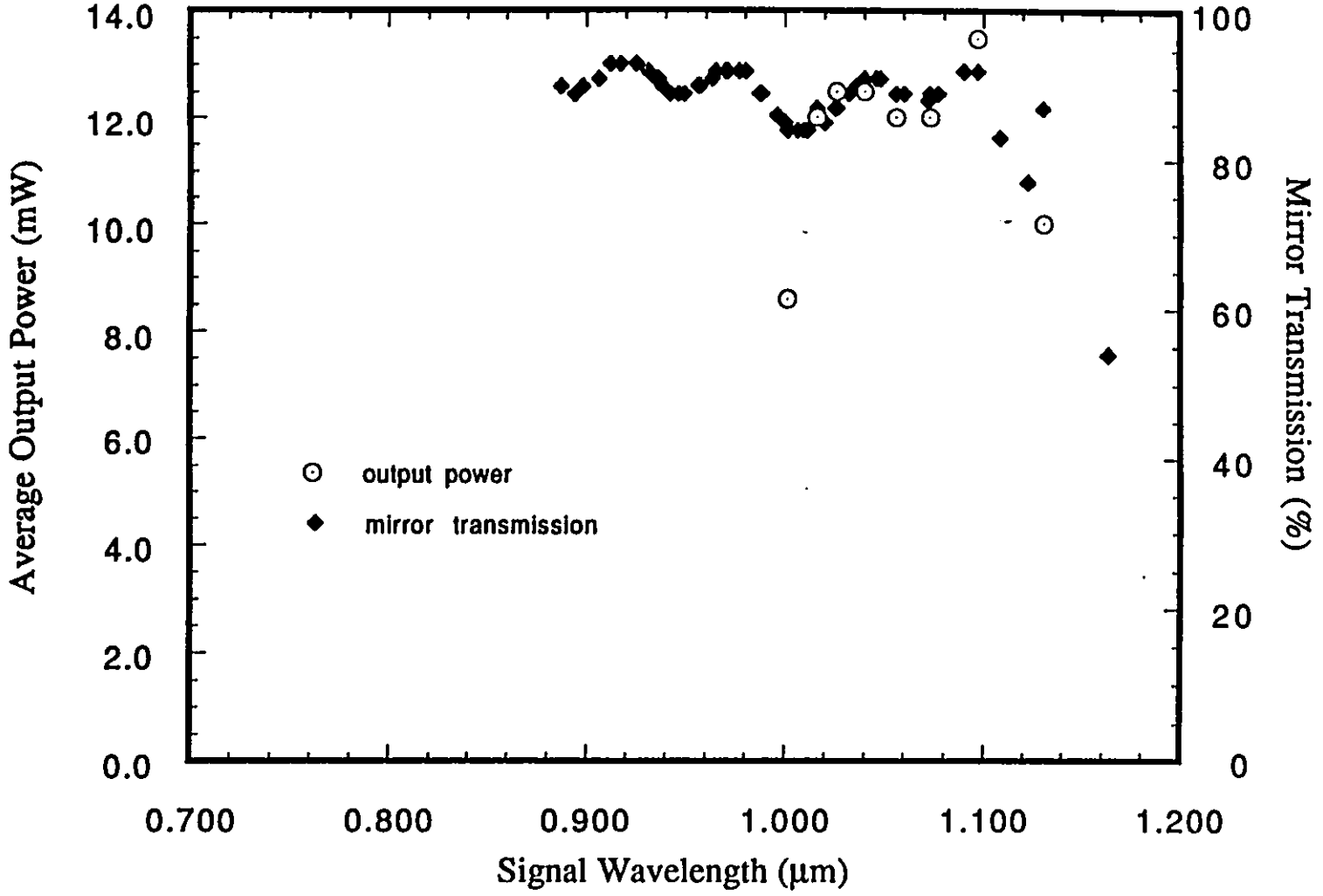

Figure 5.2. Average output power of the optical parametric oscillator using mirrors highly reflecting in the 1.20 to 1.55 μm wavelength range for a 250 °C crystal temperature and 60 mW of input power.

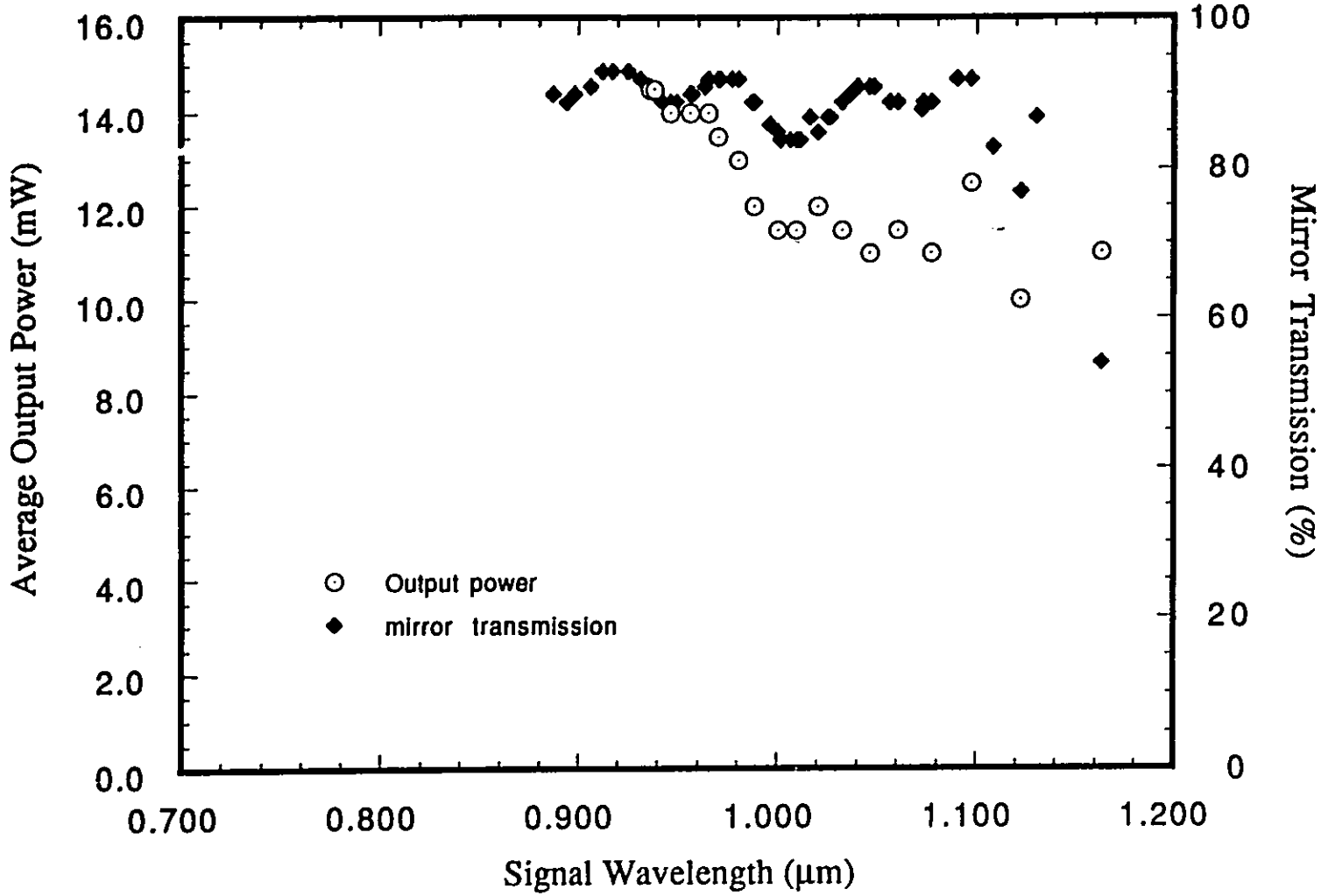

Figure 5.3. Average output power of the optical parametric oscillator using mirrors highly reflecting in the 1.20 to 1.55 μm wavelength range for a 275 °C crystal temperature and 60 mW of input power.

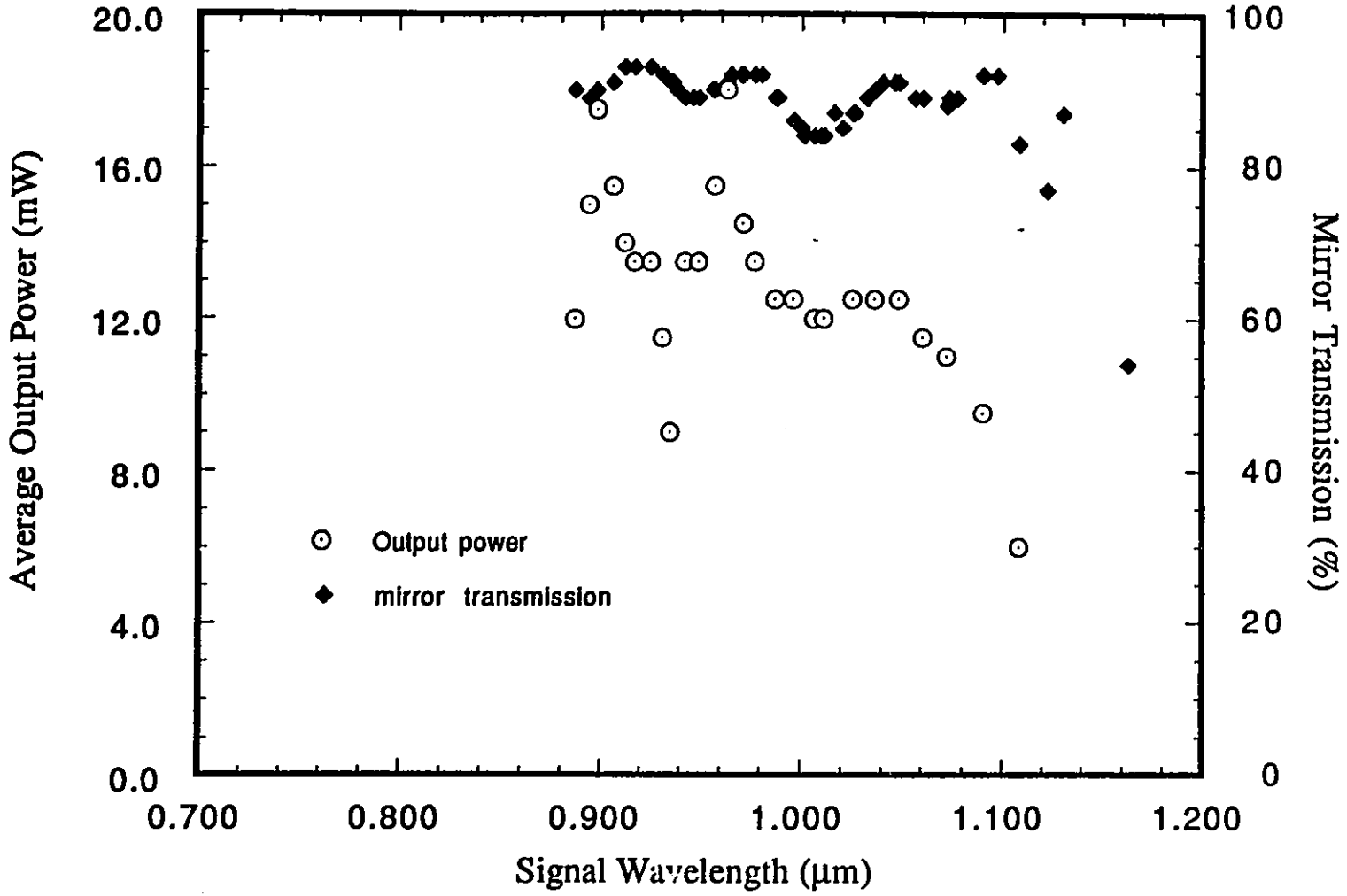

Figure 5.4. Average output power of the optical parametric oscillator using mirrors highly reflecting in the 1.20 to 1.55 μm wavelength range for a 300 °C crystal temperature and 60 mW of input power.

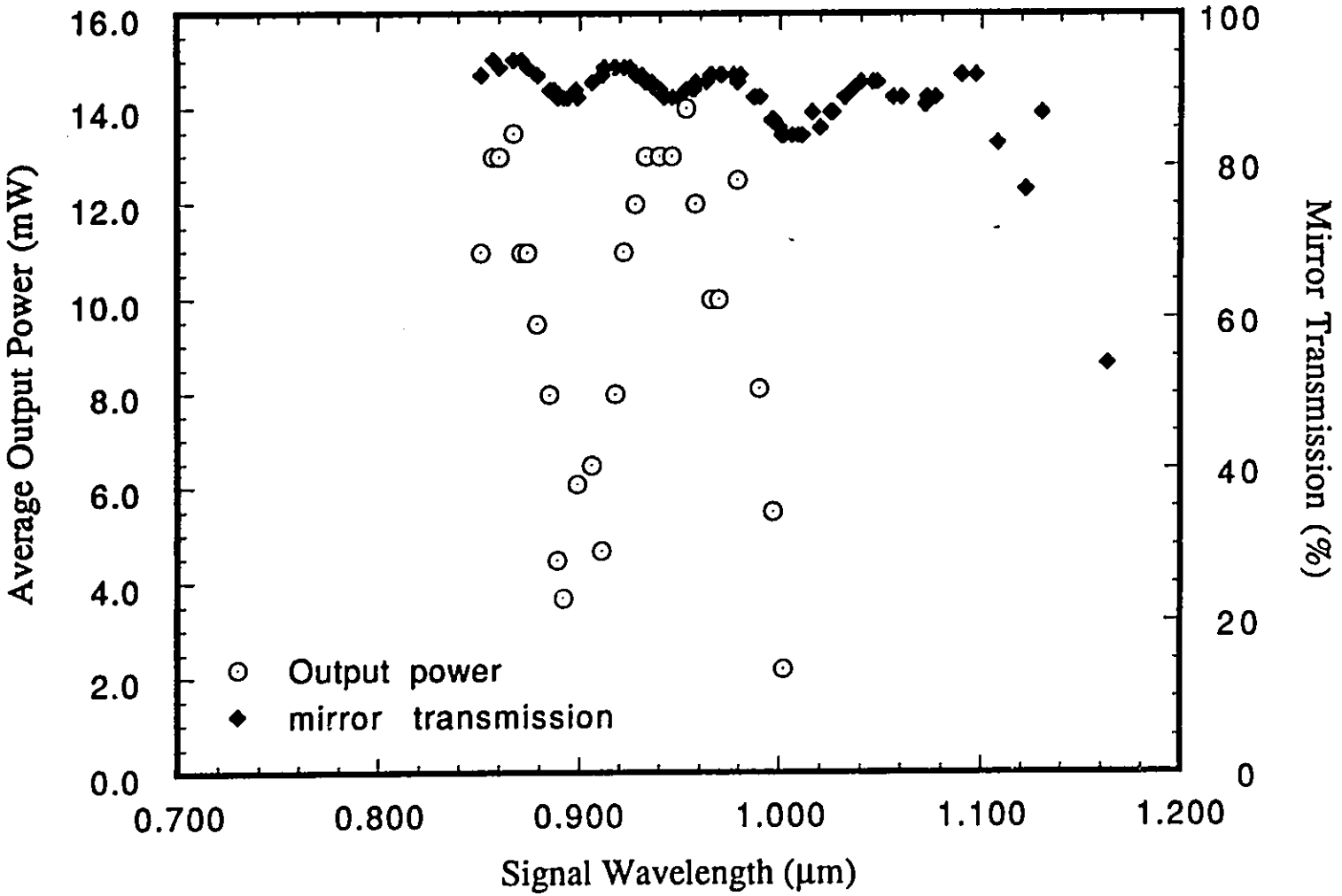

The behaviour of the output power as a function of the signal wavelength for a crystal temperature of 250 °C is shown in figure 5.2 along with the mirror transmission curve. The variation of the output power with wavelength once again follows that of the mirror transmission. This behaviour is as expected since the generated complementary idler waves have wavelengths in the 1.20 to 1.55 μm range. The peak average output power of 14.5 mW was observed while pumping at 584 and 585 nm. These pump wavelength values correspond to signal wavelengths of 0.932 and 0.941 μm respectively.

The output power as a function of the signal wavelength is shown in figure 5.3 for a crystal temperature of 275 °C along with the mirror transmission curve. The fluctuations in output power parallel those of the mirror transmission curve for signal wavelengths having values greater than 0.96 μm. Below this wavelength the generated idler waves are no longer completely reflected by the mirrors. This reduced reflectivity at the idler wavelength results in output radiation reduced in power and of bichromatic nature (i.e. composed of signal and idler waves). It is possible to use the system at this temperature if a monochromator is used to select the signal wavelength. The drawback here is that the behaviour of the output power will be sporadic even with the use of a monochromator. This sporadic behaviour is apparent in the fluctuations shown figure 5.3 for wavelengths below 0.96 μm. The observed maximum average output power of 14.5 mW known to be completely associated with the signal wave occurs for a 597 nm pump wavelength. This pump wavelength resulted in the production of a signal wave with $\lambda = 0.967$ μm.

Figure 5.4 shows the output power as a function of the signal wavelength for a 300 °C crystal temperature along with the mirror transmission curve. The output power should be somewhat uncorrelated to the mirror transmission curve since the generated idler

wavelengths at this crystal temperature are not produced in the 1.20 to 1.55 μm reflecting region of the mirrors. The variation of the output power with signal wavelength is a convolution of the mirror transmission coefficient at the signal and idler wavelengths. The output could once again be restricted to the signal wavelength, but the power at these wavelengths may undergo rapid fluctuations. It is not meaningful to talk about the maximum output power at a particular signal wavelength in such a situation.

Results were also obtained for two other sets of mirrors, one highly reflecting in the 1.40 to 1.85 μm wavelength range and the other in the 2.20 to 2.60 μm range. The results are similar and somewhat as predictable as those obtained for the mirrors highly reflecting in the 1.20 to 1.55 μm range and are therefore not presented here. It should be pointed out that the power at the signal wave decreases with increasing temperature. This decrease is directly related to a reduction in the gain coefficient resulting from the increased difference in wavelength of the generated waves (see equation (1.17)).

B. Behaviour of the Output Power with the Input Power

The behaviour of the output power at different input powers was examined for the operation of the system as an optical parametric oscillator. The output power was examined at the wavelength having the highest output power obtainable for a given crystal temperature. This behaviour was examined for the different sets of mirrors. Some typical results obtained are shown in figures 5.5 and 5.6. These results were obtained using mirrors highly reflecting in the 1.40 to 1.85 μm range. The cases shown in these figures are representative of the set of observed results. The behaviour of the output power with increasing input power appears to be approximately linear for all the situations examined.

Figure 5.5. Average output power of the optical parametric oscillator as a function of the input power for a 275 °C crystal temperature using mirrors highly reflecting in the 1.40 to 1.85 μm wavelength region for a 601 nm pump wavelength corresponding to a 1.003 μm signal wavelength.

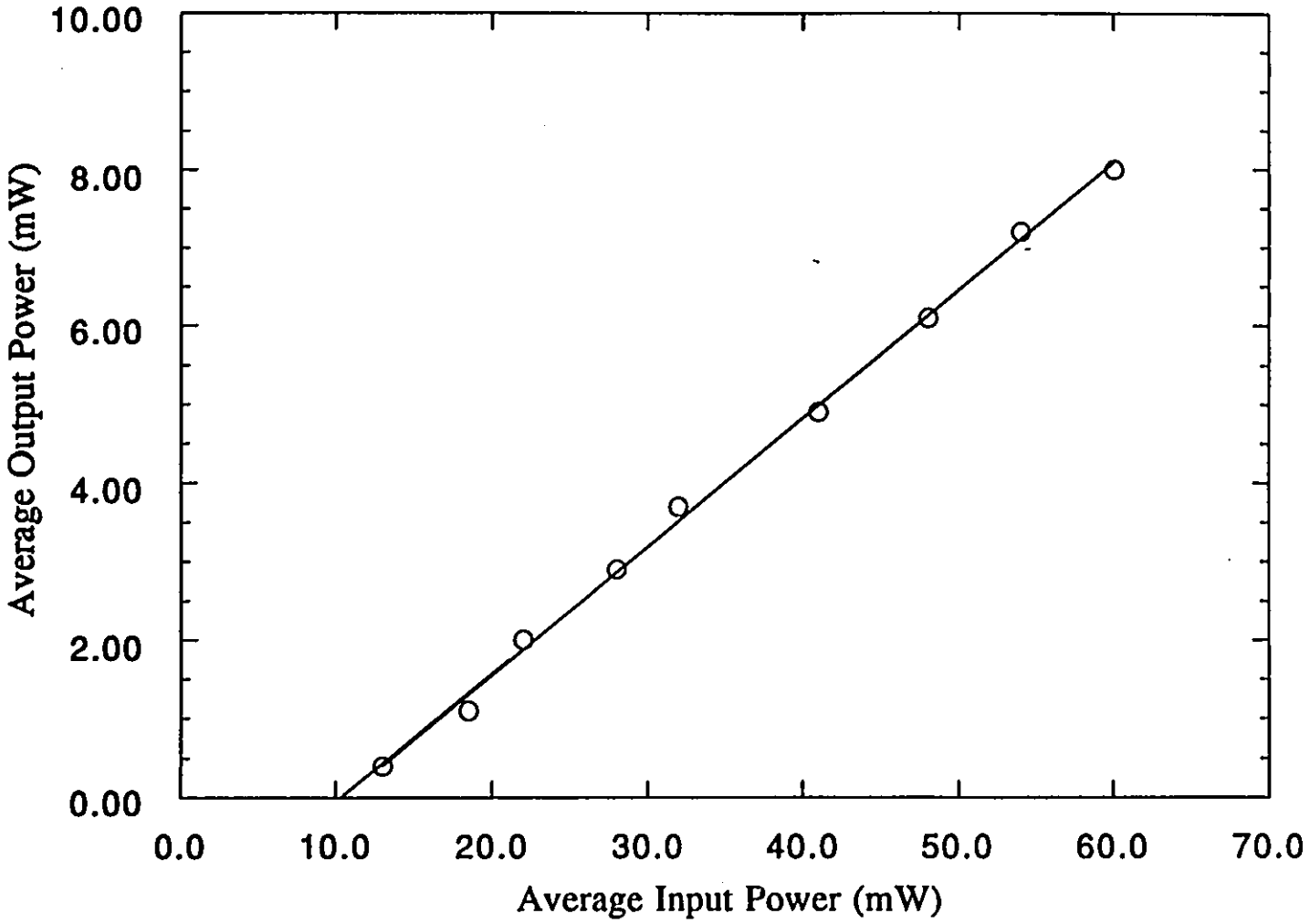

Figure 5.6. Average output power of the optical parametric oscillator as a function of the input power for a 300 °C crystal temperature using mirrors highly reflecting in the 1.40 to 1.85 μm wavelength region for a 601 nm pump wavelength corresponding to a 0.939 μm signal wavelength.

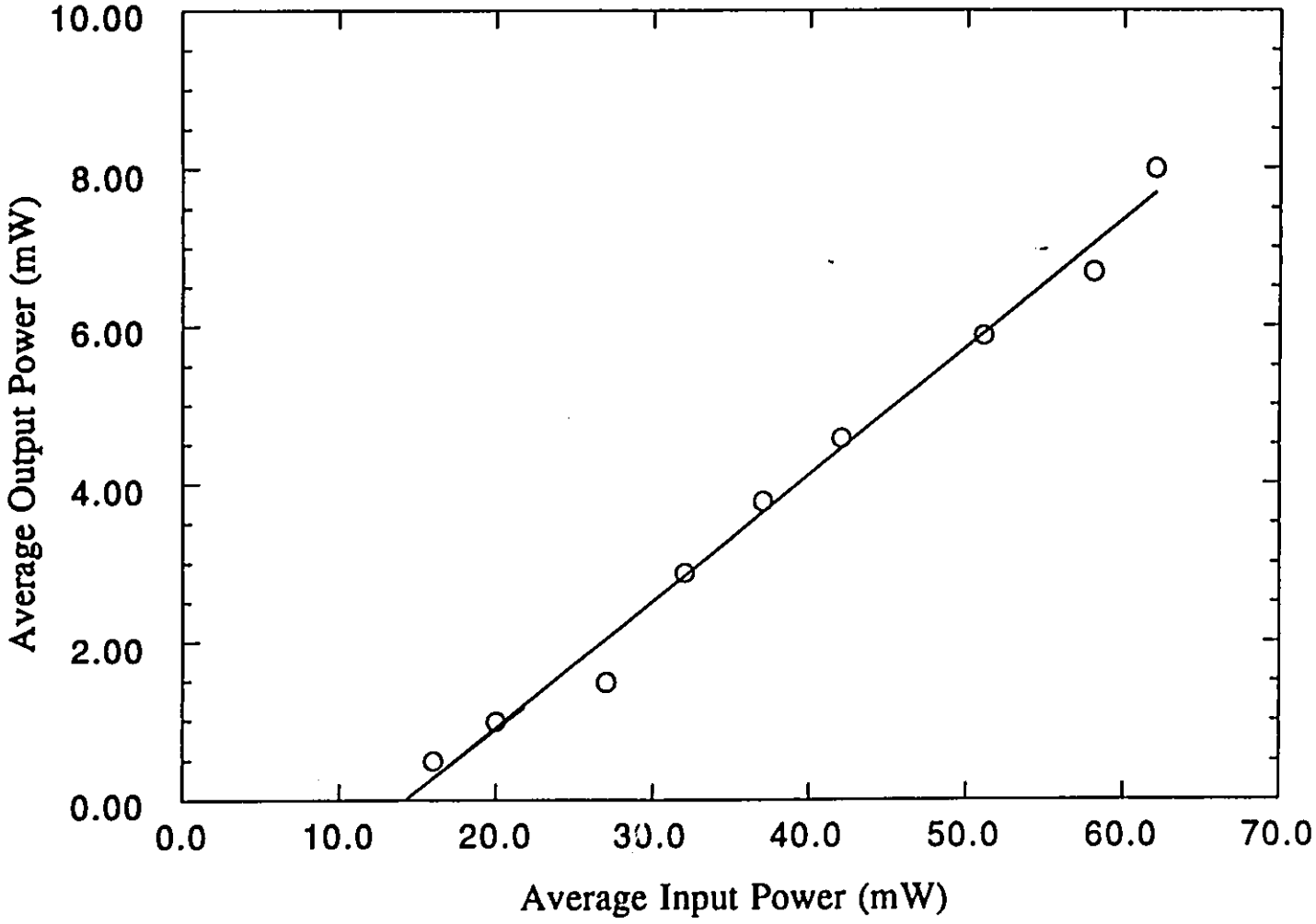

The average output power of the optical parametric oscillator as a function of the input power is shown in figure 5.5 for a 275 °C crystal temperature. The behaviour was examined for a 601 nm pump wavelength which produced a 1.003 μm signal wave. The slope of the linear relationship between the input and output power was 0.16 Watts/Watt. The value of the threshold input power was approximately 11 mW of average power. The resultant radiation was almost completely monochromatic since the idler wave had a 1.492 μm wavelength lying in the highly reflected wavelength range of the mirrors.

The average output power of the optical parametric oscillator as a function of the input power is shown in figure 5.6 for a 300 °C crystal temperature. The output power was examined for a 601 nm pump wavelength producing signal radiation having a 0.939 μm wavelength. The resulting linear relationship has a 0.16 Watts/Watt slope. The threshold occurs at 15 mW under these particular conditions. The resultant radiation is monochromatic since the generated idler wavelength was 1.655 μm.

A set of mirrors highly reflecting in the 1.75 to 2.25 μm wavelength range was also available. Unfortunately operating the system with these mirrors was not possible since they were damaged upon initial use. An inspection of these mirrors revealed that the antireflection coating was in poor condition most likely as a result of improper cleaning. It is also possible to use mirrors which are partly transmitting at the idler wavelength for the resonator system. Their use would allow the infrared output to contain both signal and idler radiation with preferential conversion to the signal wavelength. Since it was possible to obtain high conversion efficiencies without the use of mirrors, the operation of the system was not explored with the sets of mirrors partly reflecting at the idler wavelength. On one occasion it was noticed that the mirrors, although scratch free, damaged under the intense pump laser radiation. Although the dielectrics used to make the antireflection

coatings absorb very little incident radiation, the laser beam intensity was obviously close to the damage threshold.

C. Temporal Profile of the Signal Wave

The pulsed dye laser beam was found to have a 10 ns (FWHM) pulse length with 1 ns of resolution and appeared to have a Gaussian profile. The generated signal wave and the depleted pump wave both had 10 ns pulse lengths which appeared to have a Gaussian temporal behaviour. The signal pulse length is expected to be reduced by a factor of $\sqrt{2}$ since the frequency conversion process is proportional to the square of the electric field (assuming a temporal profile of Gaussian nature). The Gaussian temporal behaviour of the signal and depleted pump waves is unexpected since a longer pulse buildup time was expected before the frequency conversion process began. The Gaussian nature of the depleted wave is also unexpected since previous experiments have shown power limiting of the incident pump wave[38,44]. Regardless of these apparent inconsistencies, it seems that the pump power was high enough for the frequency conversion to proceed uninhibited by the threshold constraints of the system. In support of this conclusion, it must be pointed out that the input pump power level used to examine the temporal profile was 3 to 6 times above the system threshold input power. This leads to the hypothesis that the pump power used in this system is sufficient to mask any measurable buildup time required to achieve frequency conversion.

The power used to pump other optical parametric oscillators systems[1, 50, 51, 52] was closer to the conversion process threshold value than the pump power used in our system. In such systems many passes are required in order to obtain any frequency conversion to the signal wave of significant power. The observations of Kreuzer, in which

a 20 ns pump beam (2 to 4 times above threshold) results in the production of a signal beam pulse of 20 ns duration, are in agreement with our observations[45].

D. Spatial Profile of the Signal Wave

The spatial profile of the signal wave output from the optical parametric oscillator (using mirrors highly reflecting in the 1.20 to 1.55 μm wavelength range) was found to be approximately TEM_{00}. The variation of the intensity in the x and y directions are shown in figures 5.7 and 5.8 respectively for the strips indicated in figure 3.4 using a 591 nm pump wave and a 275 °C crystal temperature. The measurement was performed at a distance of 23.5 cm from the output mirror, and the divergence was found to be 4.3 mradin half angle. The generated waves have wavelengths of 0.962 μm (signal) and 1.610 μm (idler). The x profile of the signal wave appears to be nearly TEM_{00} and the slight noncentering of the profile is likely related to the digital nature of the scan. The y profile of the beam also appears to be TEM_{00} in nature except for a small artifact to the left of the central peak. This artifact is most likely due to partial transmission of the generated idler wave. Even with this aberration in the profile the wave appears to operate almost exclusively in the transverse TEM_{00} mode. The fact that the system operates in the fundamental transverses modes of the system does not preclude the presence of many longitudinal modes from the resonator.

E. Spectral Analysis of the Signal Waves

The spectral bandwidth of the output radiation was examined for crystal

Figure 5.7. Spatial scan of the signal wave intensity along the x-axis of an optical parametric oscillator for a 275 °C crystal temperature for a 591 nm pump wavelength using 32 mW of input power for a 0.635 cm y-axis position using a 1 mm pinhole.

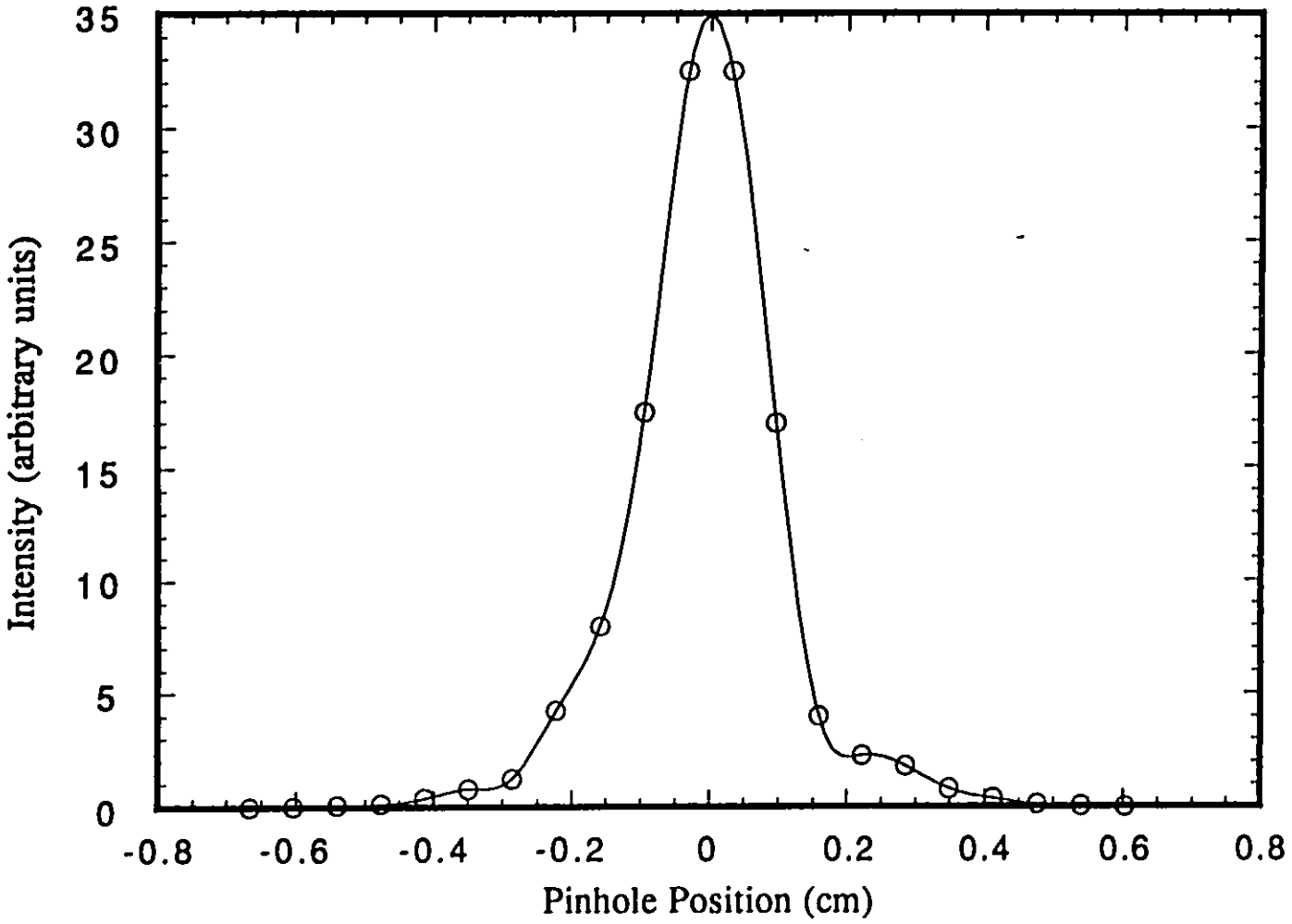

Figure 5.8. Spatial scan of the signal wave intensity along the y-axis of an optical parametric oscillator for a 275 °C crystal temperature using a 32 mW input laser beam operating at 591 nm for a 0.635 x-axis position using a 1 mm in diameter pinhole.

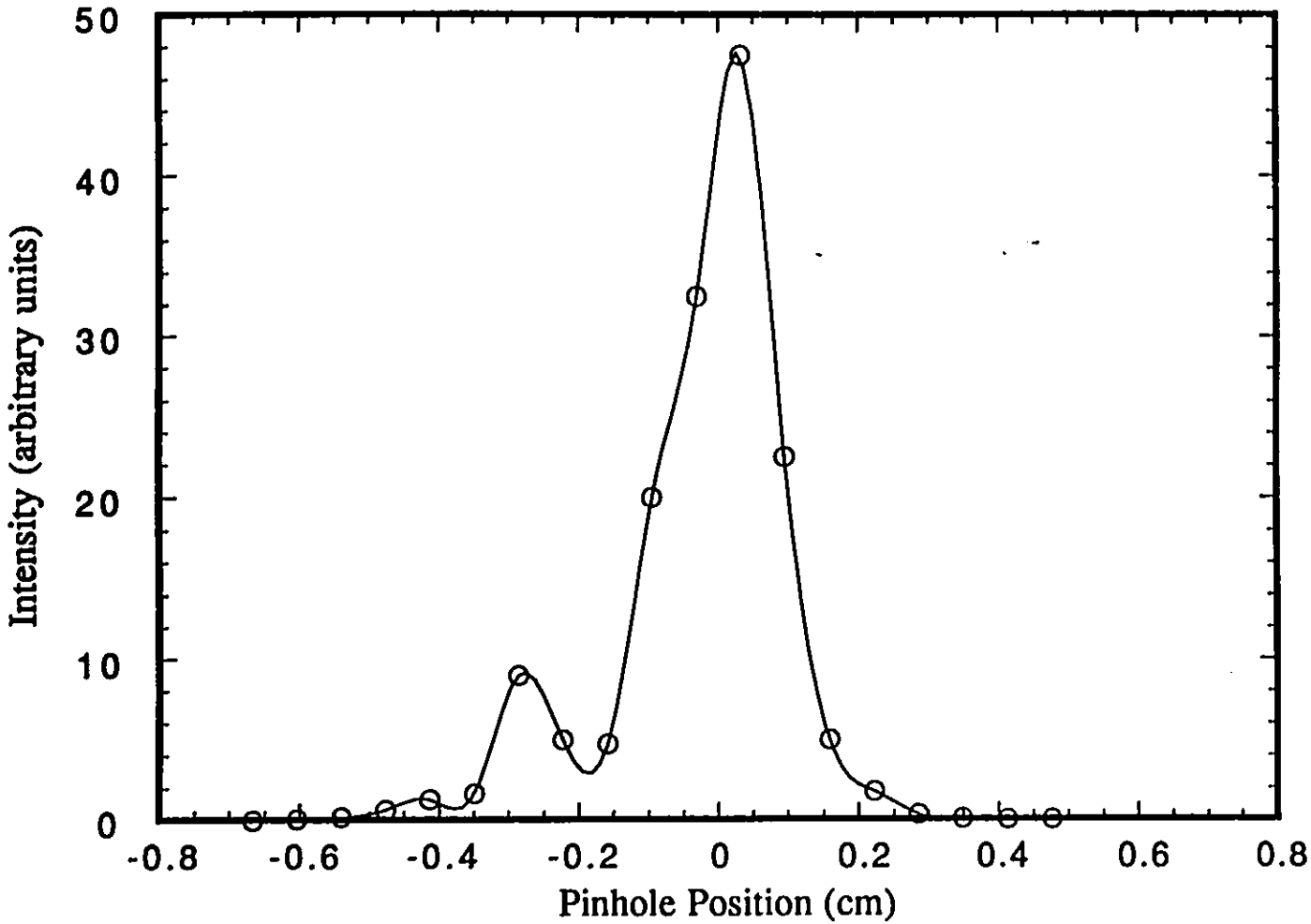

temperatures of 250 °C and 275 °C for different pump wavelengths and the results are shown in figure 5.9. The bandwidth is given in terms of $\Delta\nu$ (= $\Delta k/2\pi$) and is in units of cm^{-1}. The behaviour of the measured bandwidth near degeneracy for a 250 °C crystal temperature changes quite rapidly for the values of δ (= $(2\lambda_p - \lambda_s)/\lambda_s$) examined. Away from degeneracy the value of the linewidth approaches the behaviour of the linewidth curve provided by Chromatix. The value of the linewidth appears to be temperature dependent based on the difference between the results obtained for a 250 °C crystal temperature and those obtained for a 275 °C crystal temperature. These results are shown together in figure 5.9 for comparison.

The presence of many longitudinal modes is quite apparent upon the examination of the spectral distribution of the output signal wave. A sample high resolution scan of the output spectrum of the signal wave is shown in figure 5.10 for the optical parametric oscillator pumped by a 585 nm laser beam and a 250 °C crystal temperature using mirrors highly reflecting in the 1.40 to 1.85 μm wavelength range. The resulting radiation had a 942 μm signal wavelength and a 4.8 cm^{-1} bandwidth. For the value of δ (=0.242), which occurs at some distance from the degeneracy point, the output radiation has a very large spectral width as well as many side bands. These sidebands may result from phase-matching of waves with $|\Delta k| = n\pi$ (n = integer) and are therefore not generated at the same wavelength as the waves satisfying the condition $|\Delta k| \leq 2\pi$.

F. Conclusion

Many factors governing the operation of an optical parametric oscillator have been

Figure 5.9. The linewidth of the optical parametric oscillator output as a function of $\delta = (2\lambda_p - \lambda_s)/\lambda_s$ for 2 different crystal temperatures compared with the values given by Chromatix Inc. (Mirrors- IR1, IR1)

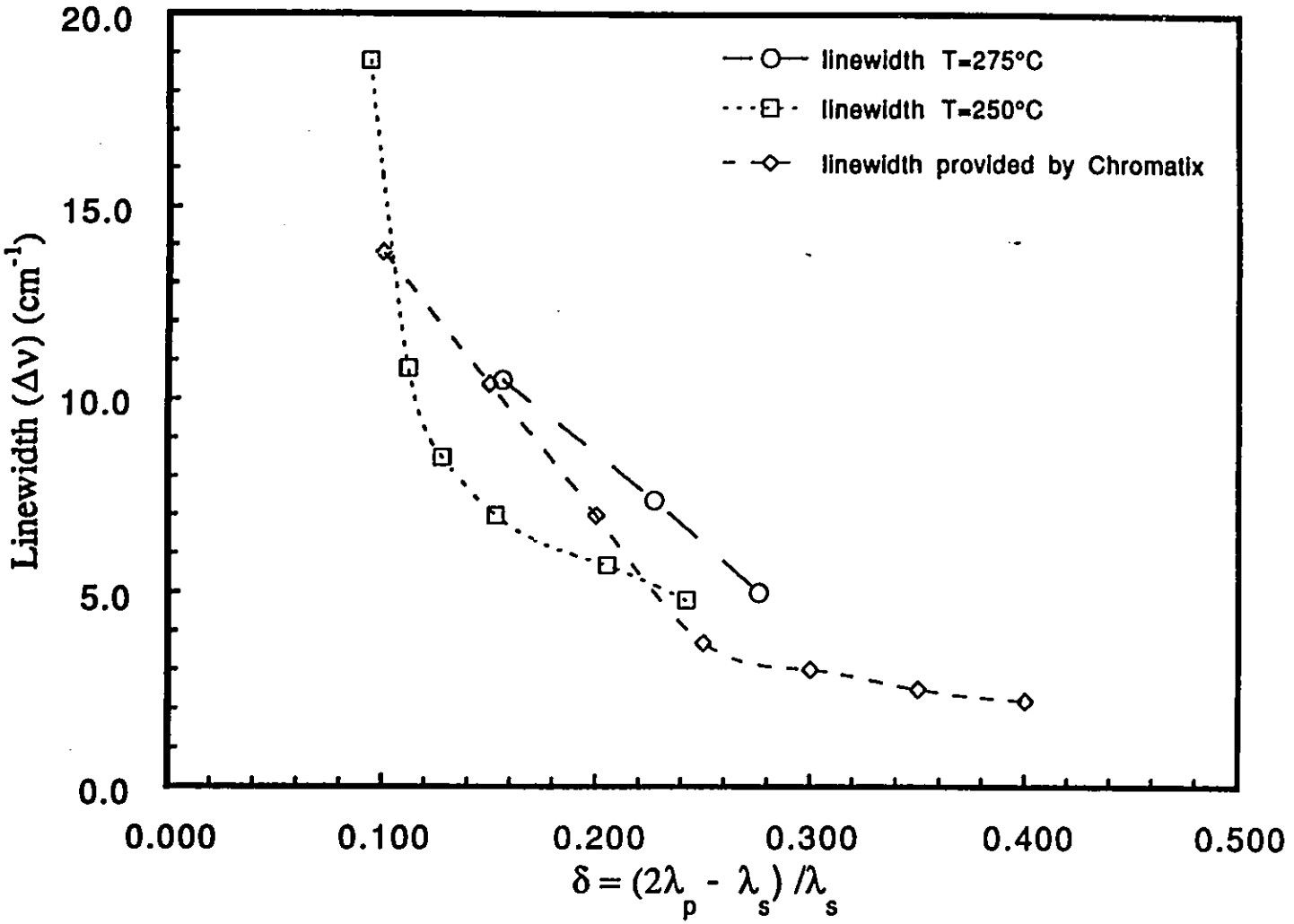

Figure 5.10. Spectral scan of a signal wave produced in the optical parametric oscillator frequency conversion process of a 585 nm pump wave using a 250°C crystal temperature and mirrors highly reflecting in the 1.20 to 1.55 μm wavelength range and 50 mW of average input power resulting in the production of a wave having $\lambda_s = 0.942$ μm. (Output power = 9.0 mW, $\lambda_i = 1.550$ μm, $\Delta\lambda = 0.425$ nm (FWHM)).

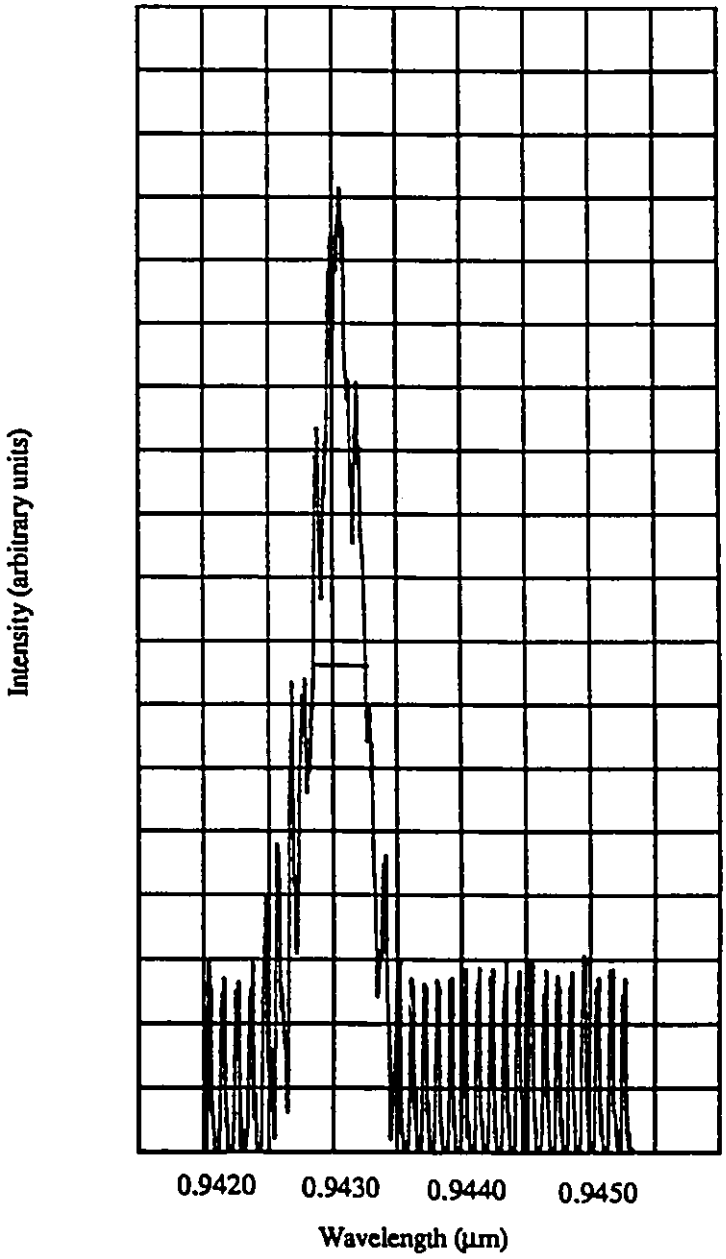

examined previously. Some of the factors examined include the behaviour of the spectral bandwidth of the output radiation as a function of the divergence angle[46]. Others include power limiting imposed by the frequency conversion process[45], and optimum focusing of the pump beam in order to maximize frequency conversion[47], as well as many others.

The next chapter is devoted to an examination of the characteristics governing optical parametric amplifier operation. The results have been presented in this sequence so that the differences of operating the system in the two different modes, that is OPO and OPA, can be compared.

Chapter 6

OPA Operation

This chapter is devoted to a thorough analysis of the physical parameters governing optical parametric amplifier operation. The experiments were designed to observe the operational characteristics of the generated waves as a function of the following parameters: temperature, pump wavelength, pump bandwidth and input power. Other system characteristics examined include: the crystal/antireflection coating damage threshold, the crystal's pump acceptance bandwidth, and maximum pump power utilization avoiding crystal damage. The reconstruction of the output power as a function of the pump wavelength for the different temperatures examined during the optical parametric amplifier frequency conversion process is also attempted using a simple model.

A. Behaviour of the Output Power from the OPA

The peak output power produced during single pass optical parametric amplifier frequency conversion is shown in figure 6.1 for several crystal temperatures. The combined output power of the signal and idler waves is shown as a function of the pump wavelength using 470 kW of pump power. The crystal temperatures used spanned the 225

Figure 6.1. Behaviour of the peak output power obtainable from the single pass optical parametric amplifier frequency converter as a function of the pump wavelength for different crystal temperatures and 470 kW of input power.

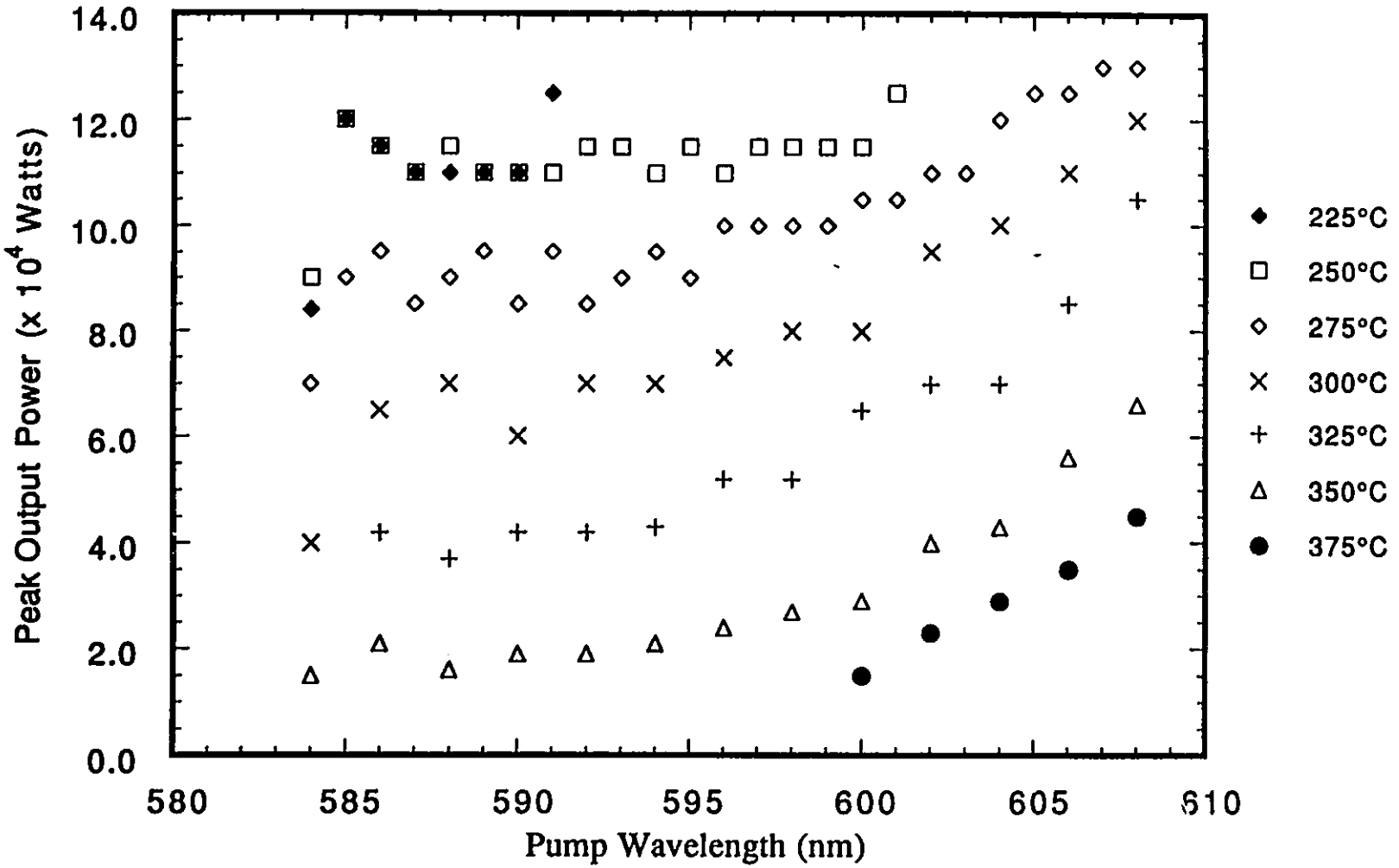

°C to 375 °C range at 25 C° intervals. Pump wavelengths above 591.5 nm for a 225 °C temperature and 602 nm for a 250 °C temperature did not result in frequency conversion of the pump beam. This lack of conversion is due to an inability to achieve phase-matching within the crystal under these conditions (see the tuning curves shown in figure 4.1). The total output power appears to be monotonically increasing with pump wavelength for all the crystal temperatures examined.

The output power for crystal temperatures above 275 °C lies below the levels observed at the lower temperatures. This drop in power is related to a couple of factors, namely: the gain factor, Γ (see equation 1.17), which is pump wavelength and temperature dependent (via the index of refraction), the pump acceptance bandwidth of the crystal, and the temperature gradient along the crystal length. For the lower crystal temperatures, the most important limiting factor is the pump acceptance bandwidth of the crystal. The pump acceptance bandwidth limits the fraction of the useful bandwidth of the pump laser which in turn decreases the available power for the frequency conversion process. The value of the acceptance bandwidth can have very dramatic effects on the generated infrared output.

B. Theoretical Crystal Pump Acceptance Bandwidths

The pump acceptance bandwidth is also determined by the generated wave, signal or idler, whichever is the most restricted in bandwidth. The signal and idler wavelengths change with changes in the pump wavelength in a manner that allows the phase-match conditions (1.13) to remain satisfied. In order to satisfy the phase-match conditions the signal wave is restricted to smaller wavelength variations than the complementary idler wave because of the particular spectral behaviour of the index of refraction of $LiNbO_3$. A

model which assumes a zero bandwidth for the signal wave while imposing no restrictions on the idler wave bandwidth is constructed in order to determine the behaviour of the crystal pump acceptance bandwidth. The equations obtained from this model, similar to those obtained by Byer for a calculation of the pump acceptance bandwidth of a system operating as an optical parametric oscillator[48], are as follows:

$$\Delta\nu_{pump}(\text{signal constant}) = \frac{1}{\beta_{idler,pump}\, l} \quad (cm^{-1}) \tag{6.1}$$

where,

$$\beta_{idler,pump} = c\left(\frac{\partial k_{idler}}{\partial \omega_{idler}} - \frac{\partial k_{pump}}{\partial \omega_{pump}}\right)_T \tag{6.2}$$

and,

l = length of the crystal in cm

c = speed of light in vacuo

T = fixed temperature

The theoretical pump acceptance bandwidth calculated for a zero bandwidth signal wave is shown in figure 6.2 for several crystal temperatures and pump wavelengths (the computer program used to obtain these values is shown in Appendix IV). The temperatures chosen span the 225 °C to 450 °C range at 25 C° intervals. The acceptance bandwidth initially decreases with temperature for a fixed pump wavelength. Above 400 °C the acceptance bandwidth begins to increase; it also increases with increasing pump

Figure 6.2. The calculated value of the pump acceptance bandwidth of a parametric frequency converter for which the signal wavelength has zero bandwidth as a function of the experimental pump range for different crystal temperatures.

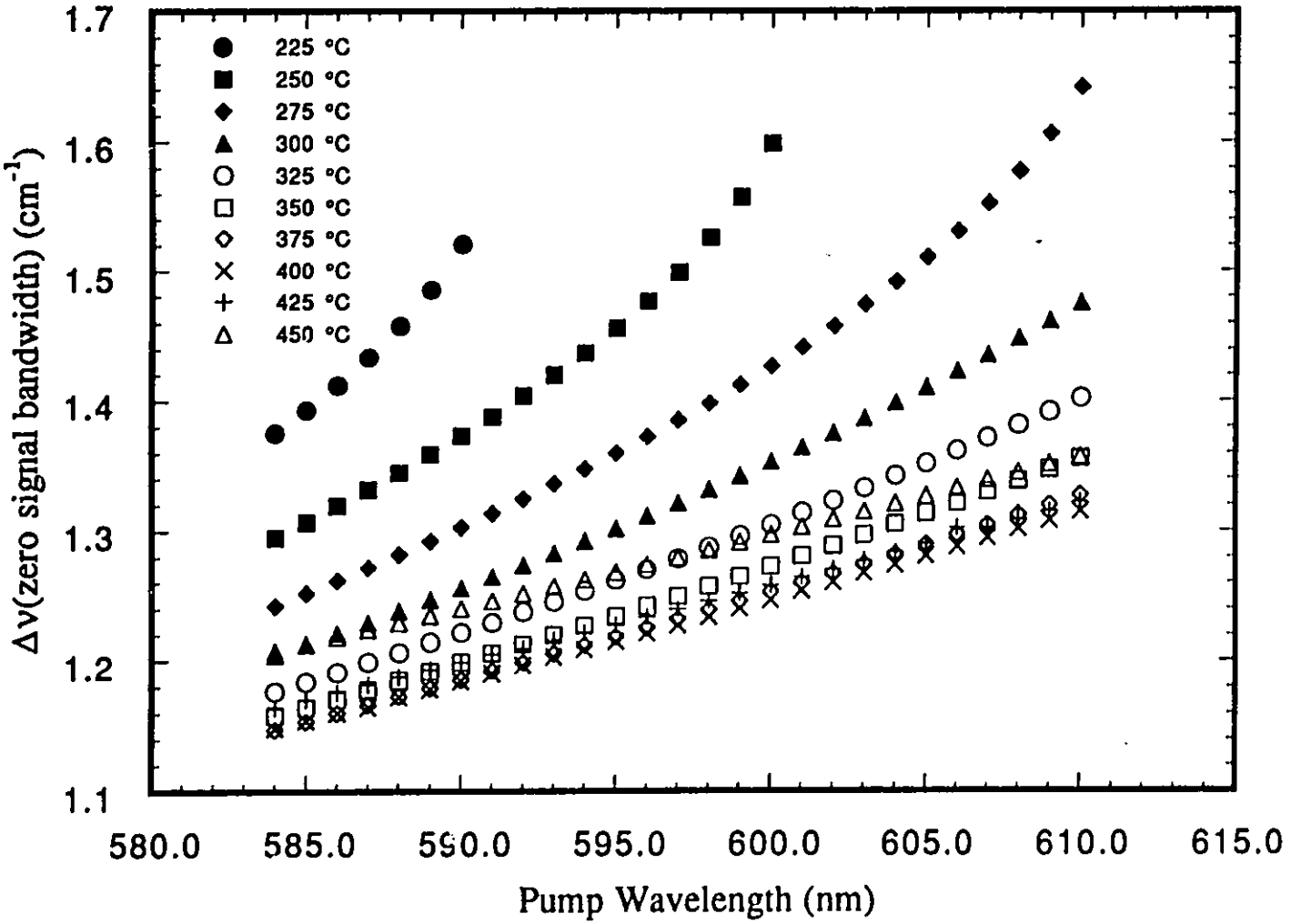

wavelength for all the temperatures shown. The rate at which the acceptance bandwidth changes decreases with increasing temperature over the entire pump wavelength range that was examined.

Figure 6.3 shows the values of the theoretical pump acceptance bandwidth obtained by assuming zero bandwidth for the idler wavelength. The value of the acceptance bandwidth increases with increasing temperature for fixed pump wavelength. The acceptance bandwidth is nearly constant, or decreases slowly with increasing pump wavelength for all temperatures examined. The rate of decrease of the pump acceptance bandwidth has a lower value for the higher temperatures. In the end the specific wave and the value of the pump acceptance bandwidth determined by it may result in less than 100 % use of the available pump power. By determining the value of the pump acceptance bandwidth it will be possible to evaluate the amount of output power obtainable from the OPA system for a given pump laser bandwidth.

C. Determination of the Wave Limiting the Crystal Pump Acceptance Bandwidth in OPA Operation

In figure 6.1 there appear to be sudden drops in the output power at a specific wavelength in the accessible pump wavelength range for a couple of crystal temperature (the system is operated with 60 mW of constant input power). The nature of these drops in power seems rather curious and their locations possibly correlated to a common physical characteristic of OPA operation. In order to determine if this was the case, the bandwidth of the pump laser was reduced in order to see if the power drop points would change positions. As it turned out they did, therefore a deeper exploration into the underlying physical phenomenon causing the power drop was undertaken. This exploration was

Figure 6.3. The calculated value of the pump acceptance bandwidth of a parametric frequency converter for which the idler wavelength has zero bandwidth as a function of the experimental pump range for different crystal temperatures.

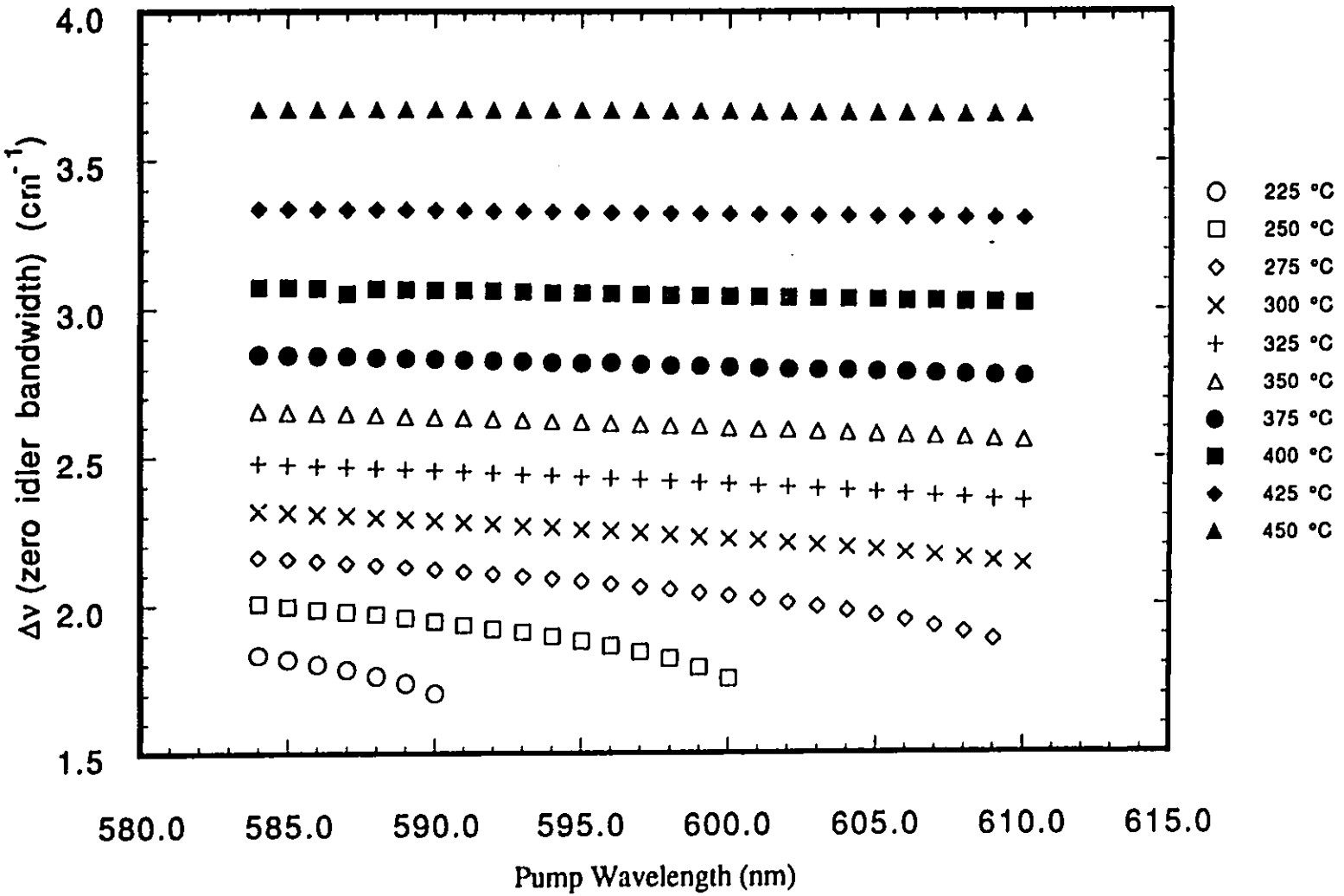

performed by taking careful measurements of the output power over the accessible pump wavelength range in order to determine the exact point at which the drops in output power occurred.

The measured output power as a function of the pump wavelength having a 0.95 cm^{-1} bandwidth is shown in figure 6.4 for following crystal temperatures: 275 °C, 300 °C, and 325 °C. The behaviour of the output power at the other temperatures did not conclusively reveal any curious change in the output power over the accessible pump wavelength range. In figure 6.4, the output power shows drops below a constant median level (indicated by the lines in figure 6.4) at the points indicated by the arrows. This drop in output power is postulated to be due to the finite pump acceptance bandwidth of the crystal. In the model the wave determining the pump acceptance bandwidth is postulated to have zero bandwidth, i.e. it remains at a fixed value for the particular pump wavelength and crystal temperature. This fixing of the wavelength of one of the waves forces the other wave to have a bandwidth that allows the phase-match conditions to be satisfied over the useful portion of the pump wave bandwidth. The values of the pump wavelengths for which the drop in output power occurs are shown in table 6.1 along with the values of the theoretical pump acceptance bandwidth for a system operating with either a signal or an idler wave having zero bandwidth.

An examination of the calculated pump acceptance bandwidth values shown in table 6.1 reveals that the value obtained for a signal wave assumed to have zero bandwidth remains approximately constant. This calculated value of the pump acceptance bandwidth is approximately the same for the three different temperatures shown for fixed pump bandwidth, but is also dependent on the pump bandwidth. The value obtained for a 0.95 cm^{-1} pump bandwidth is 1.26 cm^{-1} and that for a pump bandwidth having a value greater

Figure 6.4. Peak output power of the optical parametric amplifier as a function of the input wavelength for three different crystal temperatures, a 564 kW input power and a 0.95 cm^{-1} ($=\Delta\nu=\Delta k/2\pi$) bandwidth.

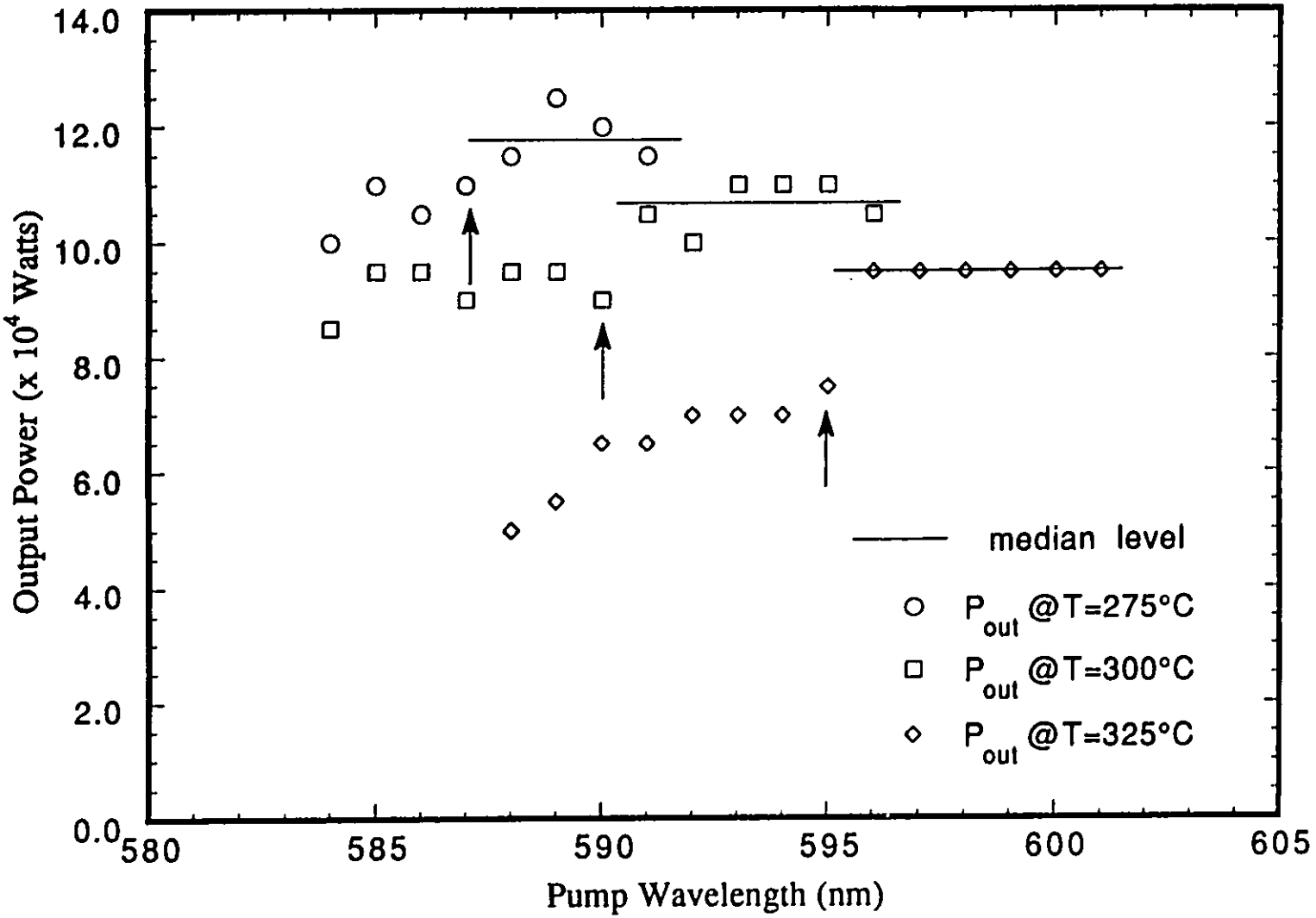

	λ_{pump} at power drop (nm)		$\Delta\nu_{pump\ acceptance}$ (cm^{-1}) (zero idler banwidth)		$\Delta\nu_{pump\ acceptance}$ (cm^{-1}) (zero signal banwidth)	
pump bandwidth / Temperature (°C)	$\Delta\nu_{pump}$ = .95 cm^{-1}	$\Delta\nu_{pump}$ > .95 cm^{-1}	$\Delta\nu_{pump}$ = .95 cm^{-1}	$\Delta\nu_{pump}$ > .95 cm^{-1}	$\Delta\nu_{pump}$ = .95 cm^{-1}	$\Delta\nu_{pump}$ > .95 cm^{-1}
275	587	595	2.15	2.08	1.27	1.36
300	590	602	2.29	2.21	1.26	1.38
325	595	606	2.44	2.38	1.26	1.36

Table 6.1. Calculated pump acceptance bandwidth of the signal and idler waves while operating the system in the Optical Parametric Amplifier configuration using two different pump bandwdiths.

than 0.95 cm^{-1} is 1.36 cm^{-1}. The pump wavelength values shown in table 6.1, obtained with the original pump bandwidth, were found by determining the pump wavelength at which the output power dropped below the rough median level that can be drawn for the output power as a function of the input power in figure 6.1. These latter results, obtained prior to the results contained in figure 6.4, as mentioned in the introductory paragraph to this section, planted the seed for the investigation into which wave determines the pump acceptance bandwidth of the crystal. An examination of the output power as a function of the pump wavelength contained in figure 6.1 reveals that power drops also occur at wavelengths lying outside the pumping range for temperatures above 325 °C. Unfortunately these pump wavelengths were not accessible with the dye used to obtain almost all the experimental measurements. In summary, the pump acceptance bandwidth must be chosen in a way that allows full use of the pump laser bandwidth.

D. Distribution of the Output Power Between the Waves Generated During OPA Operation

The output powers given at the different pump wavelengths and temperatures in figure 6.1 are distributed between the signal and idler waves. They can be separated into signal and idler output power values by using the following equations[49]:

$$P_{tot} = P_{signal} + P_{idler} \tag{6.3}$$

$$\frac{P_{signal}}{P_{idler}} = \frac{\omega_{signal}\, n_{idler}}{\omega_{idler}\, n_{signal}} = \frac{\lambda_{idler}\, n_{idler}^2}{\lambda_{signal}\, n_{signal}^2} \tag{6.4}$$

$$P_{signal} = \frac{\lambda_{idler}\, n_{idler}^2}{\lambda_{signal}\, n_{signal}^2 + \lambda_{idler}\, n_{idler}^2} P_{tot} \tag{6.5}$$

The values of the individual output powers obtained from this decomposition are shown in figure 6.5 as a function of the wavelengths of the generated waves for the different temperatures examined. The figure reveals a somewhat complex distribution of output power as a function of the wavelength. The generated wavelengths shown in the figure span the 0.8 to 2.2 μm range. In general the value of the output power at the signal wavelength increases very rapidly up to 1.0 μm. The output power seems to vary

Figure 6.5. Peak output power of the signal and idler waves produced by the optical parametric amplifier for several temperatures with pump wavelength range and 470 kW of input power.

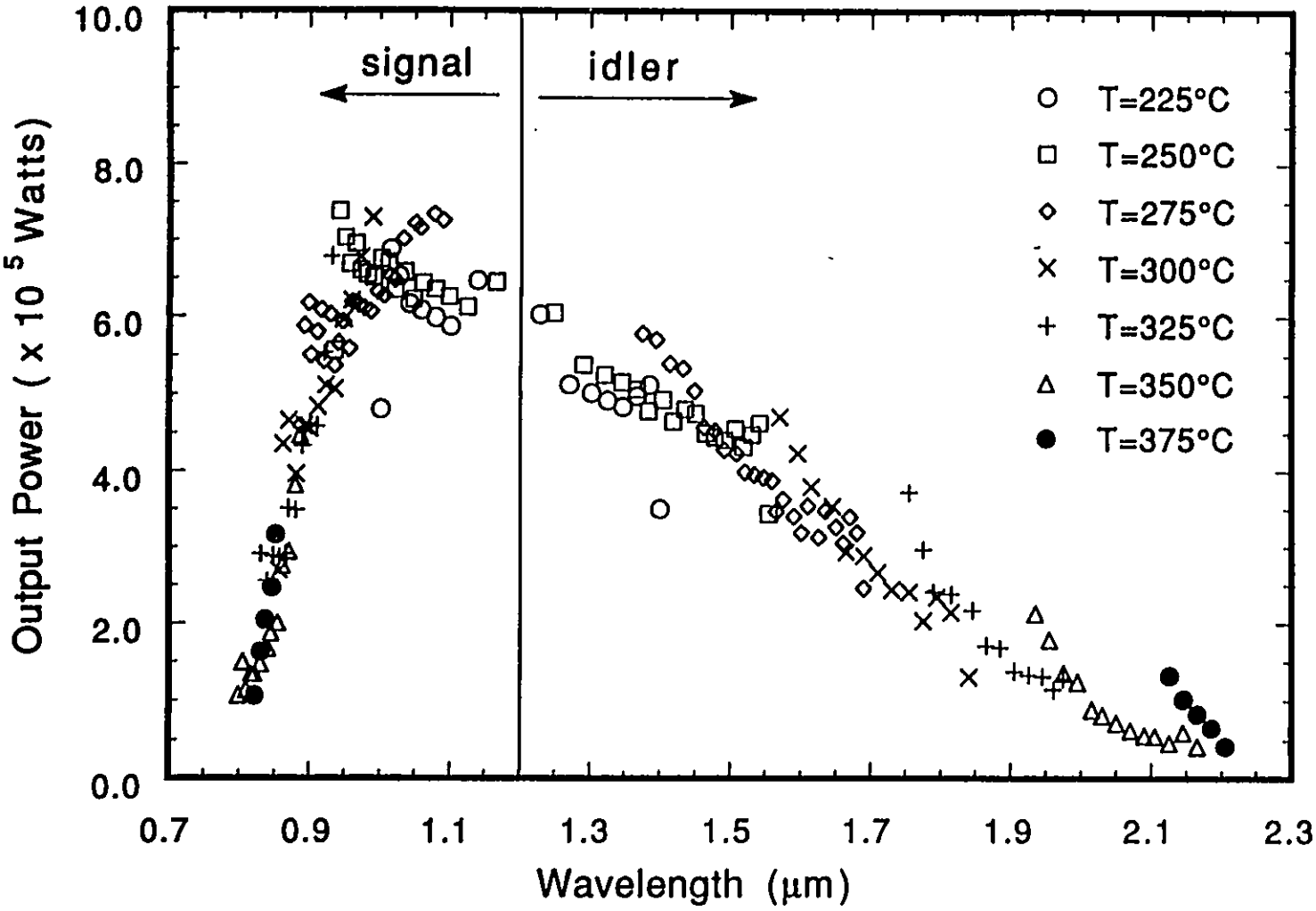

erratically for wavelength values in the 0.9 to 1.6 μm range. Part of this behaviour is related to a plateauing of the total output power as can be seen in figure 6.1 for 225 °C and 250 °C crystal temperatures. The output power of the generated idler waves tends to decrease with increasing wavelength for the majority of the wavelengths examined. The points which do not follow this trend correspond to fluctuations in the total output power as can be seen from a cross correlation between the values in this figure and those contained in figure 6.1.

It is interesting to note that the output power for the same idler wavelength generated at different temperatures is always greater for the higher temperature (this ignores the small fluctuations of the total output power). This is not always the case for the output power at the different signal wavelengths shown. An examination of the pump acceptance bandwidth assuming no bandwidth for the signal wave reveals that the acceptance bandwidth has a greater value for the higher temperatures and therefore results in greater output power for the wave produced at the higher crystal temperature (ex: T= 350°C, λ_{idler}= 2.16 μm, $\Delta\nu_{acceptance}$= 1.16 cm^{-1}, and for T= 375°C, λ_{idler}= 2.16 μm, $\Delta\nu_{acceptance}$= 1.29 cm^{-1}). An examination of the theoretical pump acceptance bandwidths shown in figure 6.2 reveals that this last statement does not hold for crystal temperatures above 375 °C. The design of a parametric frequency converter operating at temperatures above 375 °C must therefore take this variation of the expected behaviour of the output power at the idler wave into account.

E. Model of the Output Power Produced During OPA Operation

A simple model was used to qualitatively reproduce the behaviour of the output

power with input wavelength shown in figure 6.1. The model assumed a constant input intensity for the input wave. Theoretical values for gain coefficient, Γ, were obtained from equation (1.17) for the entire pump wavelength range and the different crystal temperatures shown in the figure (the computer program used is listed in Appendix V). In order to obtain the appropriate value for the gain provided by the crystal, it is necessary to multiply the values given in figure 6.6 by the square root of the pump power and the length of the crystal (see equations 1.17 and 1.20). The corresponding pump power is 560 kW and that for the length of the crystal is 0.05 m resulting in a multiplicative constant of 35 $Watts^{1/2}$. The results obtained for the gain coefficient, Γ, using the computer program listed in Appendix V are shown in figure 6.6 divided by the $(unit\ power)^{1/2}$. The behaviour of the coefficient increases very slowly with increasing pump wavelength and quite a bit faster with increasing temperature.

The next step in the evolution of the model requires taking into consideration the influence of the pump acceptance bandwidth on the output power. This influence is taken into account by multiplying the gamma coefficient by the fraction of the pump power used in the frequency conversion process. This fraction is determined by dividing the theoretical pump acceptance bandwidth value by the value obtained in table 6.1 for the drop in output power of a pump wave having a bandwidth greater than 0.95 cm^{-1}. If the resulting fraction is greater than 1, then the fraction of the pump power used is taken to be 1 since the pump acceptance bandwidth is larger than that of the value of the pump bandwidth value obtained in table 6.1 (1.36 cm^{-1}). If the fraction is less than 1, then the fraction of the pump power used is taken to be this latter value since the value of the pump bandwidth (1.36 cm^{-1}) exceeds that of the pump acceptance bandwidth. Figure 6.7 shows the results obtained from multiplying the gamma factor by the fraction of the pump bandwidth used in the

Figure 6.6. Spectral variation of the gain coefficient/(Power)$^{1/2}$ as a function of the pump wavelength for different crystal temperatures.

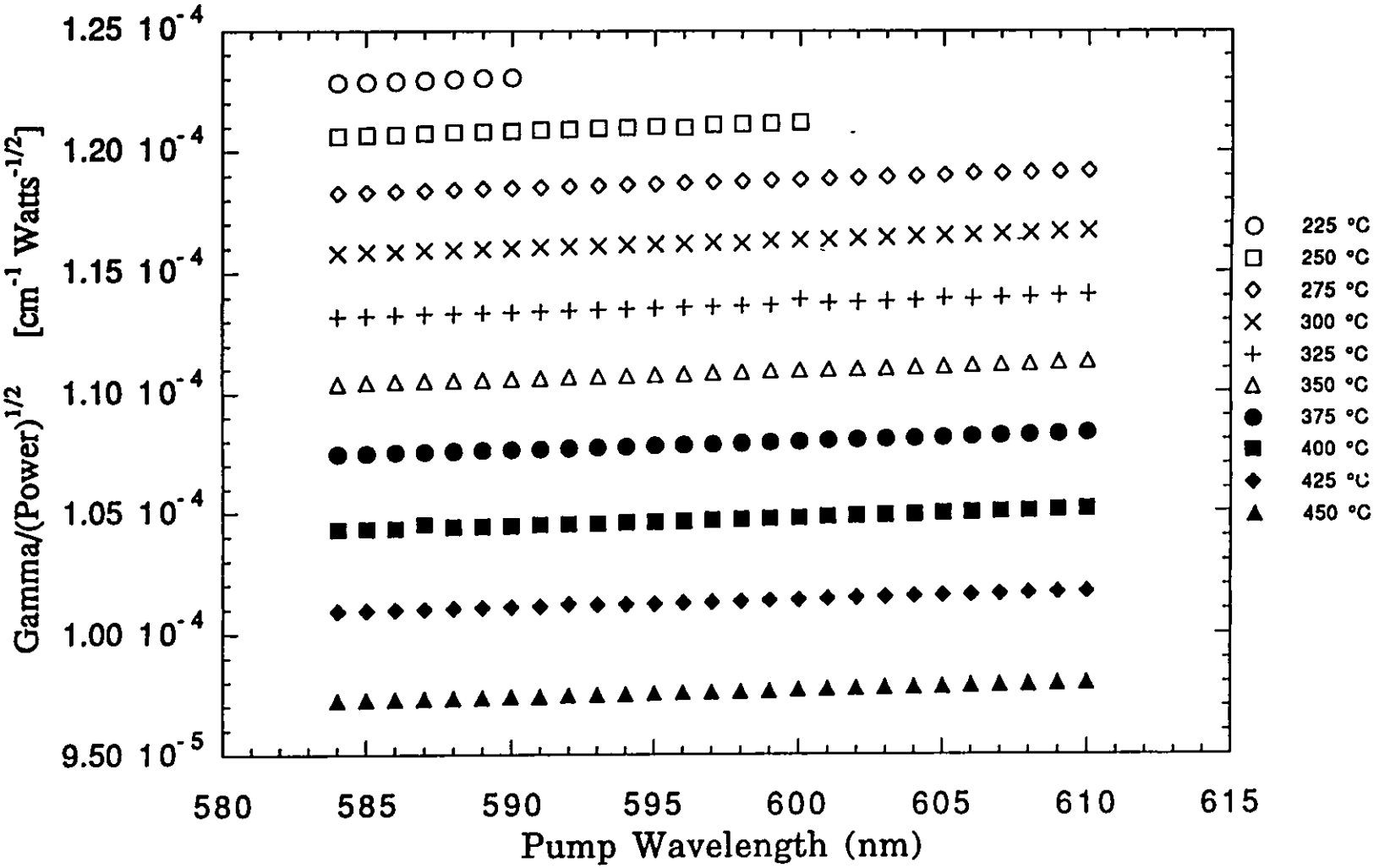

Figure 6.7. The calculated variation of the power conversion factor for several temperatures over the accesible pump wavelength range determined by the gain factor and the pump acceptance bandwidth.

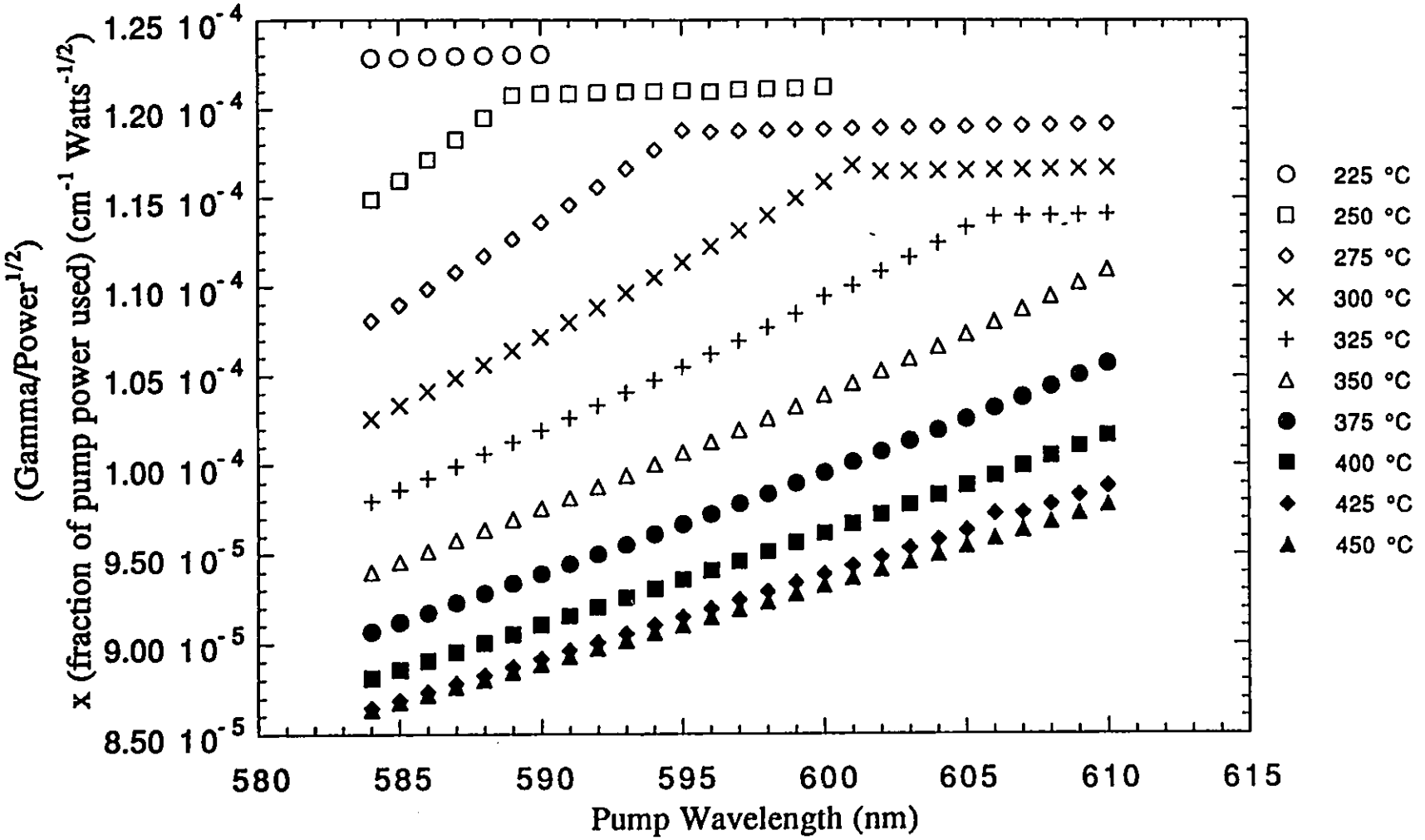

conversion process. Although there is not very good agreement between the results contained in this figure and figure 6.1, the general behaviour of the output power shown in figure 6.1 is reproduced. Multiplying the effective gain coefficient shown in figure 6.7 by the 35 Watts$^{1/2}$ multiplicative factor reveals that the theoretical power conversion from the pump wave into the generated waves is an order of magnitude lower than that observed experimentally. A more realistic model would require solving the coupled set of nonlinear differential equations (1.14) for a depleted pump beam.

The value of the gain coefficient at the signal and idler waves is shown in figure 6.8. In order to obtain a more realistic value for the gain coefficient (identical for both generated waves thus far), the power distribution between the signal and idler waves and the fraction of pump power used in the conversion process (pump acceptance bandwidth influence) must be included. The implementation of these factors are shown in figures 6.9 and 6.10. The behaviour of the gain coefficient shown in figure 6.8 shows a striking resemblance to that of the power distribution shown in figure 6.5. Unfortunately the factors influencing the effective gain coefficient of the crystal (unknown in actual value) have not been taken into consideration. Once the pump power distribution to the generated waves is taken into consideration, the resemblance to the behaviour of the output power is reduced (see figure 6.9). It should be pointed out that the smoother behaviour of the output power at the idler wavelength shown in figure 6.5 is partly reproduced by the behaviour of the effective gain coefficient as shown in figure 6.9. The behaviour of the output power at the signal wave is not at all reproduced in figure 6.9; in fact no resemblance exists. The final influencing factor of the pump acceptance bandwidth on the values of the effective gain coefficient is shown in figure 6.10. As can be seen by comparing figures 6.5 and 6.10, a better reproduction of the behaviour of the output power at the signal wavelength occurs once the effect of the pump acceptance bandwidth has been taken into account. The

Figure 6.8. Variation of the gain coefficient of the generated waves as a function of the wavelengths for different crystal temperatures.

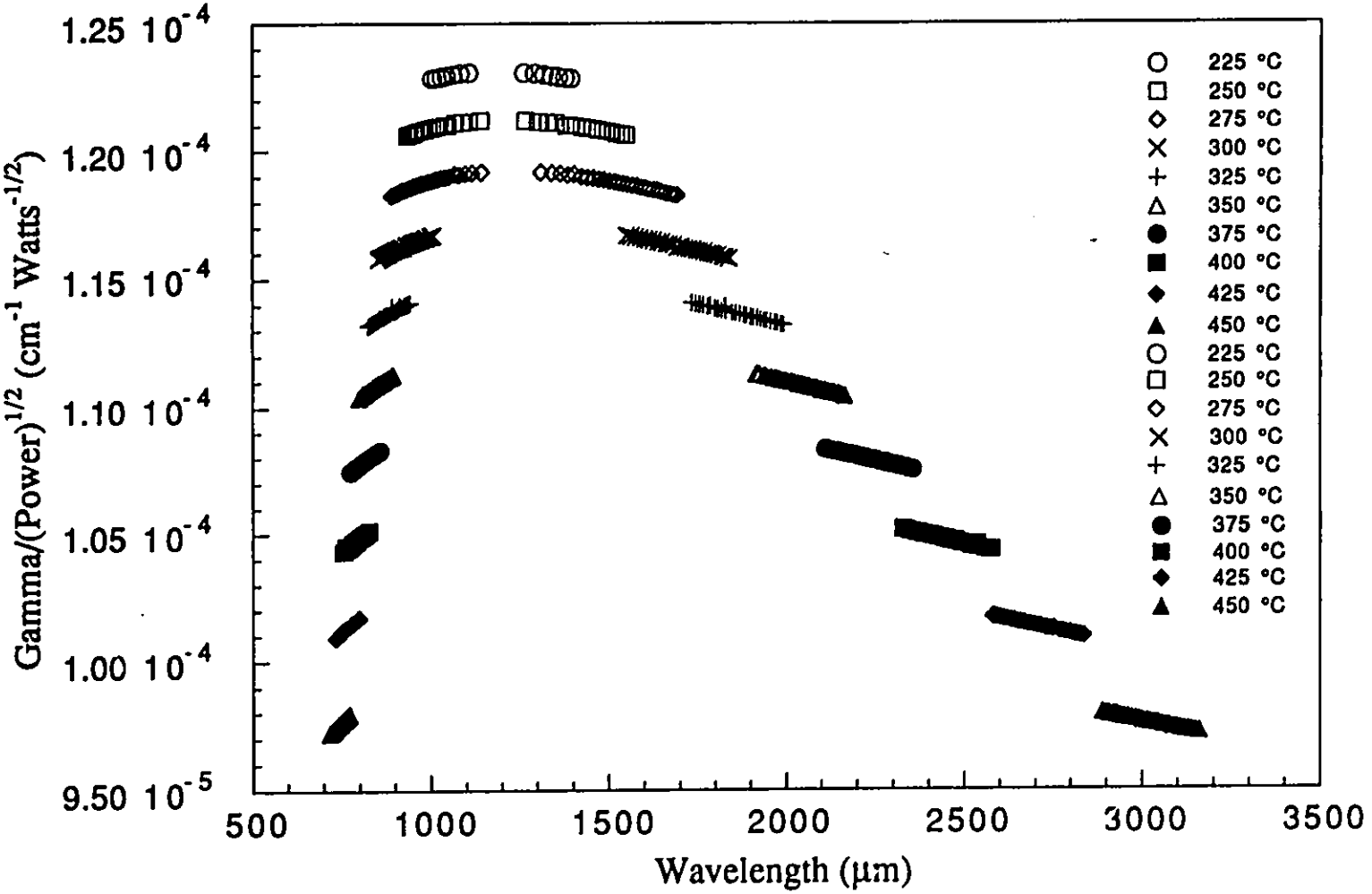

Figure 6.9. Fraction of the pump power distributed to the signal and idler waves multiplied by the gain coefficient for the generated waves for different crystal temperatures.

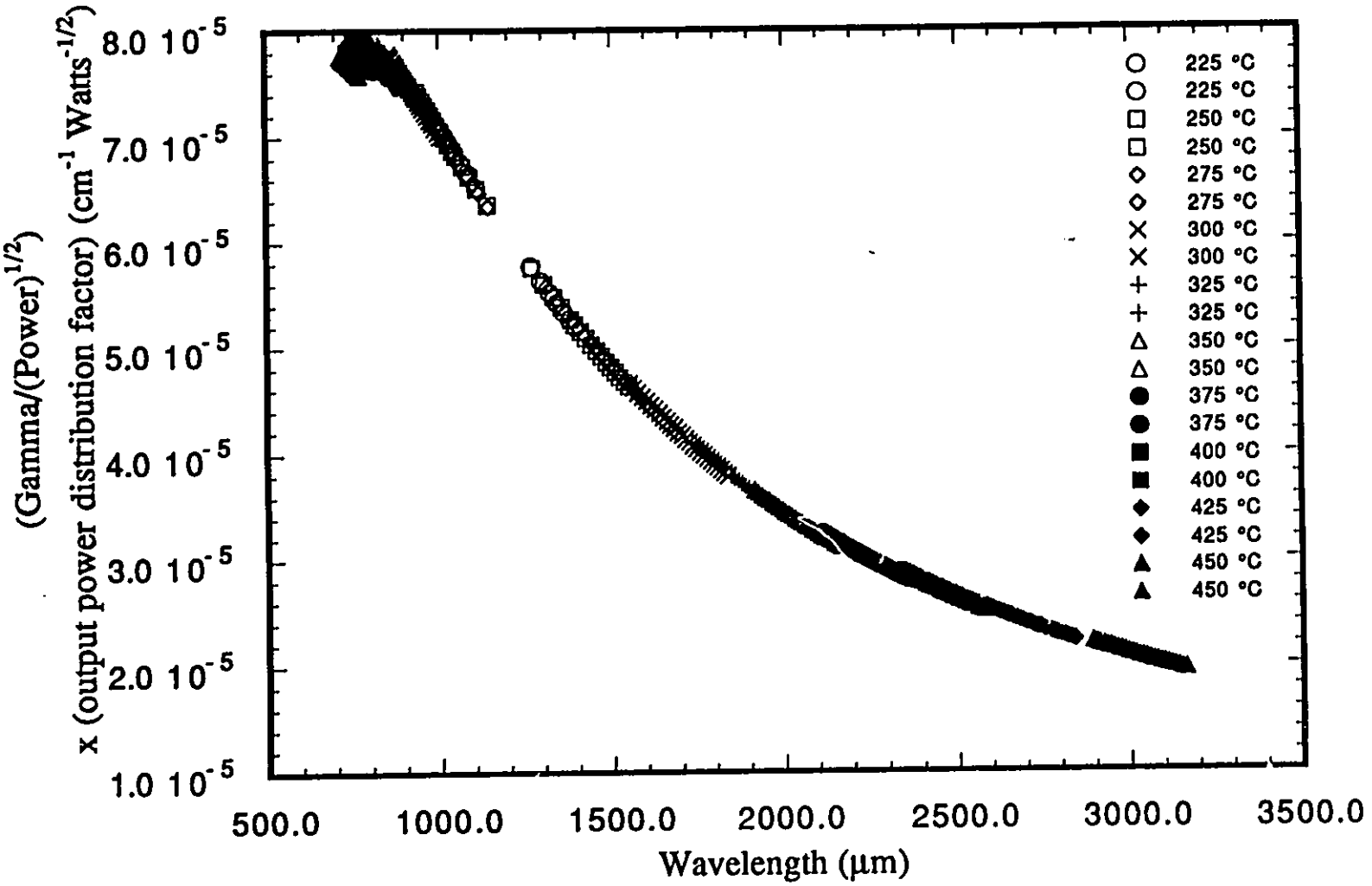

Figure 6.10. Expected linear conversion coefficient determined by the wavelength dependent gain coefficient, power distribution factor and the crystal pump acceptance bandwidth.

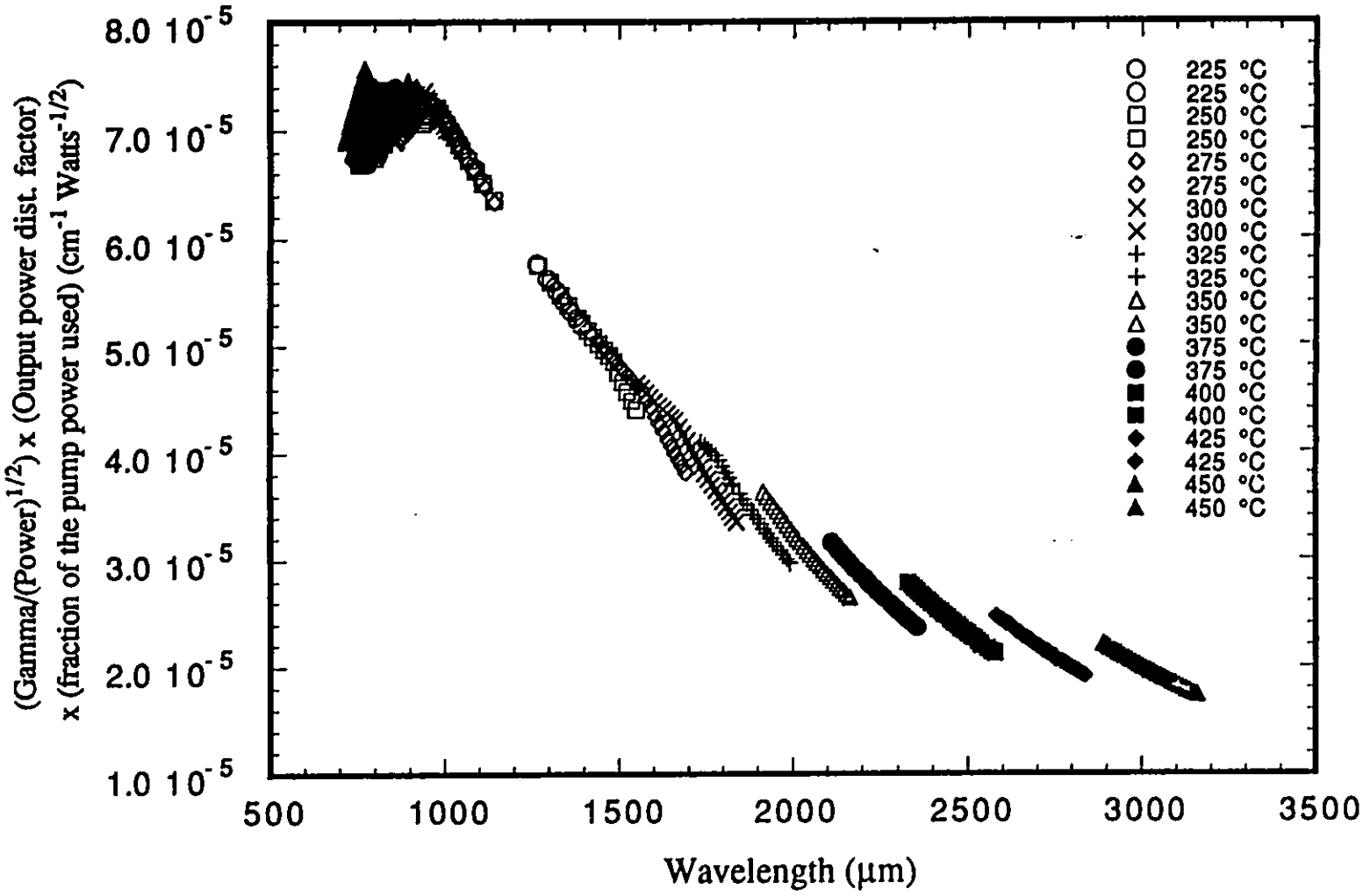

behaviour of the output power at the idler wave is also better reproduced once this last factor is taken into account.

F. Measurement of the Crystal Damage Threshold

The behaviour of the output power as a function of the input power was examined for a 592.5 nm pump beam and a 275 °C temperature in order to obtain the damage threshold on a slightly chipped UC crystal sacrificed for the occasion. The results of the behaviour of the output power with input power before the crystal damaged are shown in figure 6.11. The output power as a function of the input power follows a linear relationship having a 0.24 Watts/Watt slope. The threshold for frequency conversion is extrapolated to be in the 10 to 20 mW average input power range. The average input power reached 200 mW before the crystal began damaging. The damaging of the crystal was indirectly observed by the resulting drop in output power once the process occurred. The pump power at which the crystal damage occurred is equivalent to a 240 MW/cm^2 intensity. This value is much larger than the values quoted in the literature[2,10,43].

An subsequent examination of the crystal revealed only damage to the surface. The damage appeared to be confined to the antireflection coating and the interface between it and the crystal. R.W. Wallace has described a browning of $LiNbO_3$ crystals operated below the damage threshold. This browning of Wallace's crystal appeared after many hours of using the crystal in a non oxygenated environment[3]. Since the pump beam in the system we examined was not focused into the crystal, damage internal to the crystal was not

Figure 6.11. Maximum conversion efficiency observed for the output power as a function of the input power during optical parametric amplifier operation inducing crystal damage for a 275 °C crystal temperature and a 592.5 nm pump beam.

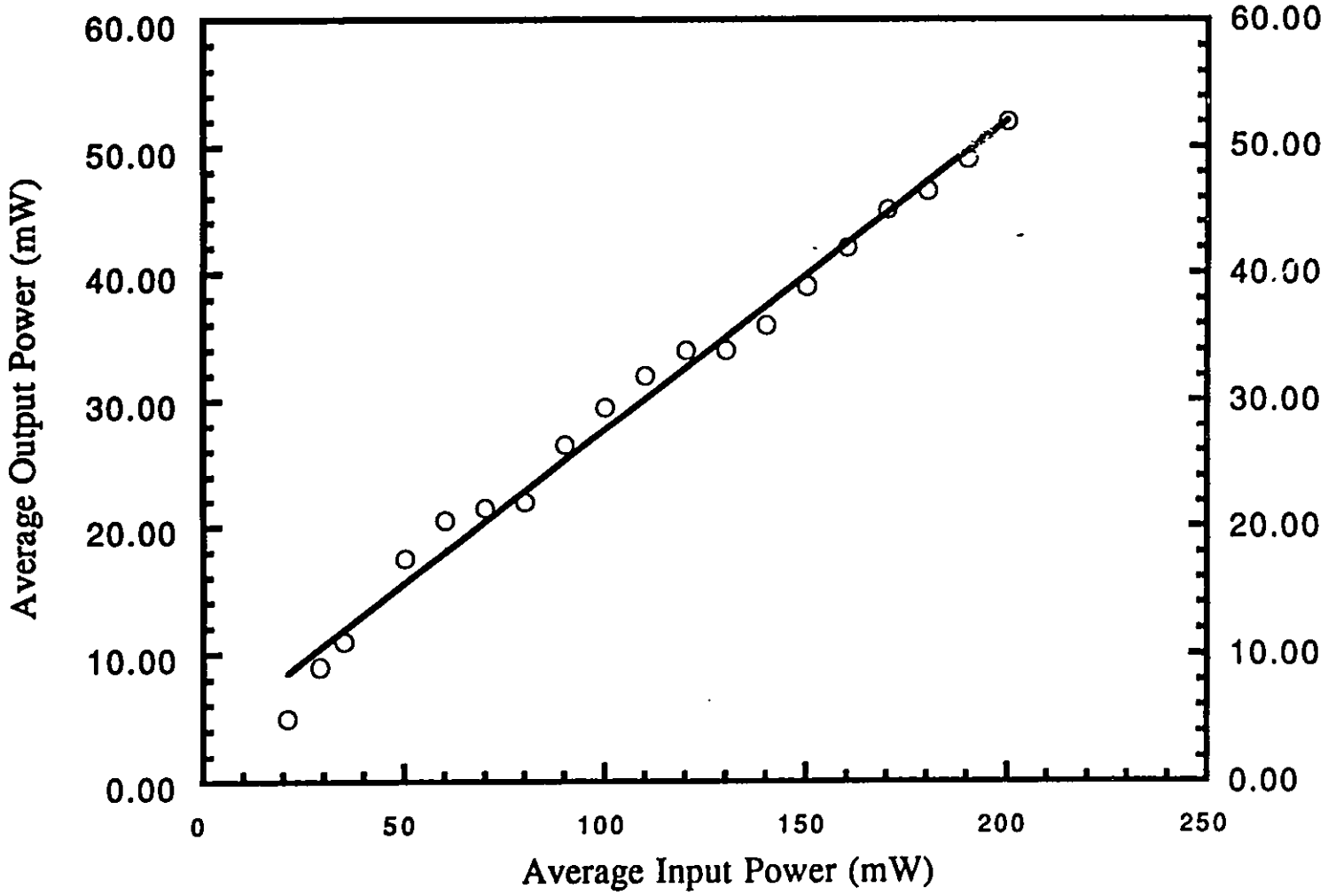

expected. A visual inspection of the Chromatix crystal after over a 100 hours of operation below the damage threshold did not reveal the presence of any macroscopic damage. This damage was avoided since the crystal was bathed in oxygen when it was heated and exposed to the intense electromagnetic fields of the pump beam.

G. Maximum Observed Conversion Efficiency

The maximum conversion efficiency observed during OPA operation was found for a 589 nm pump beam and for a 225 °C crystal temperature resulting in the production of waves having the following wavelengths: λ_s = 1.076 μm and λ_i = 1.299 μm. These results are shown in figure 6.12. The slope of the linear relationship between the input and output power is 0.50 Watts/Watt. This measurement was done at the pump wavelength for which the observed output power was maximum over the given accessible pump wavelength range for a fixed input power and crystal temperature. The particular crystal temperature used for the data in figure 6.12 was chosen arbitrarily since the behaviour of the output power with the input power using a fixed pump wavelength was not measured for all the crystal temperatures used to obtain the data in figure 6.1.

H. Full Pump Power Utilization

In order to make full use of the dye laser power, without damaging the crystal, the pump beam size was expanded by a factor of 4 in area. The results of the output power as a function of the input power are shown in figure 6.13. The temperature of the crystal was arbitrarily chosen at the low value of 250 °C. The pump wavelength was chosen at the

Figure 6.12 Maximum conversion efficiency observed for the output power as a function of the input power during optical parametric amplifier operation using a 589 nm pump beam with a 225 °C crystal temperature.

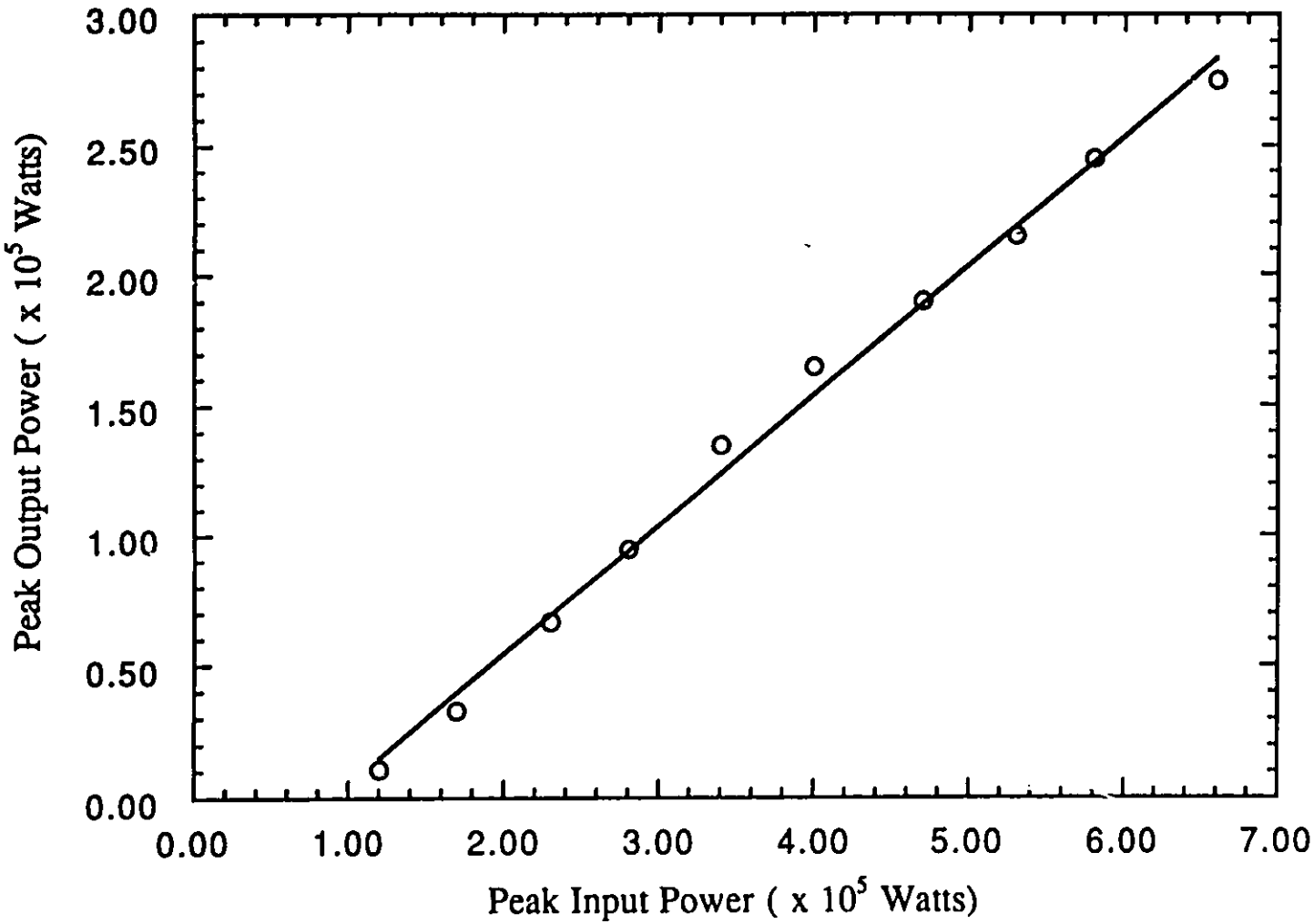

Figure 6.13. Output power of an optical parametric amplifier as a function of the input power for a pump beam expanded by a factor of 4 in cross section for a 592.5 nm pump beam and a 250 °C crystal temperature.

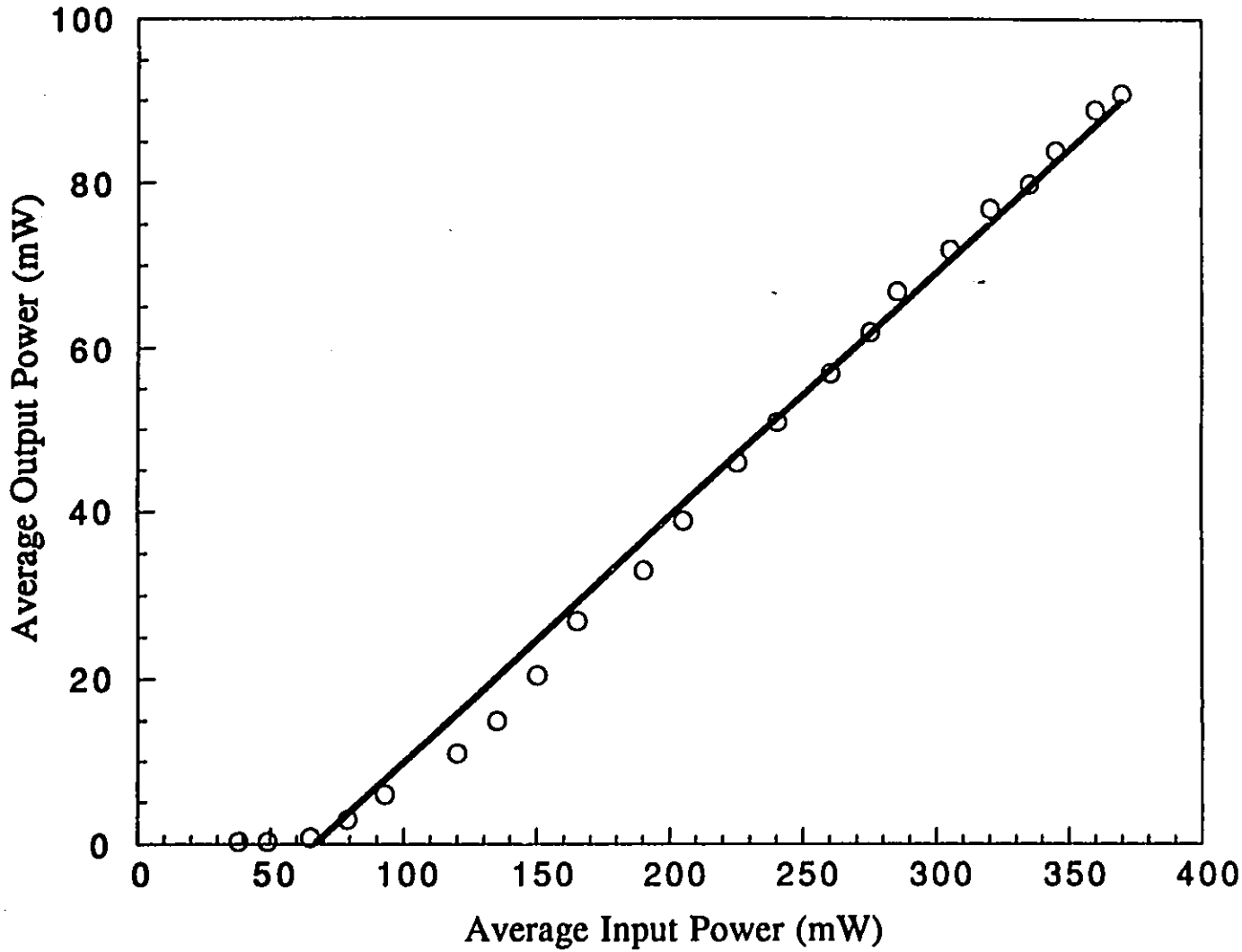

peak output power wavelength of the dye. The threshold obtained under these conditions was approximately 40 mW and is in the range expected from a beam expanded by a factor of 4 in area. The maximum average output power observed under these particular conditions was 91 mW while pumping with 370 mW of power and corresponds to 855 kW of peak output power. The slope of the approximately linear relationship describing the behaviour between the input and output power is 0.32 Watts/Watt.

I. Conclusion

This concludes the section on the results obtained while operating the system as an optical parametric amplifier. The most important result is that the system operated as a single pass frequency converter is as efficient, and possibly more so, than operating the system using a resonator. In conclusion, a system must be used to separate the two different waves generated in the single pass frequency conversion process.

Conclusion

In summary, high peak power, rapidly tunable near-infrared coherent radiation has been successfully produced in the 0.734 to 2.853 μm wavelength range using a 10 ns pulse length dye laser operating in the 584 to 610 nm range. When operating the system in the Optical Parametric Oscillator configuration, the pump wavelength and crystal temperature allowing the generation of radiation at a specific signal wavelength must be chosen carefully. If this selection is done haphazardly, the generated idler wave may not be produced in the highly reflecting region of the resonator mirrors. In such a case the output radiation from the resonator is bichromatic and the power distribution between the generated waves is no longer known. When the system is operated in the Optical Parametric Amplifier configuration it is not necessary to choose the pump wavelength and crystal temperature required to produce a given signal wave as carefully since the system does not possess the added constraint resulting from the use of selectively transmitting mirrors used to enhance the production of the signal wave. In this case, some kind of filter must be used to separate the two generated waves. Another important factor influencing Optical Parametric Amplifier operation is the crystal pump acceptance bandwidth determined by the signal wave. This acceptance bandwidth must be considered when evaluating the amount of output power achievable from the frequency conversion process.

As in many cases, the research presented in this thesis can be built upon in several ways. It would be interesting to determine the exact spectral distributions of both the generated signal and idler waves if a grating allowing an examination of the spectral characteristics of the waves having wavelengths above 1.3 μm were available. An examination of the temporal profile across the beam cross section might reveal why all the waves appear to have the same temporal behaviour. This examination would necessitate a detector with better time resolution than the one currently available as well as an oscilloscope capable of sampling signals in the GigaHertz frequency range. Mapping out of the spatial profile of both the signal and idler waves would be useful in determining the intensity profile of the generated waves. An examination of the exact transmission and reflection properties of the crystal antireflection coating could also reveal if the generated waves are resonated in any way during the Optical Parametric Amplifier frequency conversion process. The development of a better model could also help understand further some of the characteristics of Optical Parametric Amplifier operation.

Appendix I

Form of the Electron Polarization

The expected form for the electron polarization oscillating at frequency ω_1 is:

$$P(\omega_1,t,z) = P(\omega_1)\, e^{i\,(k_1 z - \omega_1 t)} + P^*(\omega_1)\, e^{-i\,(k_1 z - \omega_1 t)} \qquad (1)$$

$$P_i = \varepsilon_0\, \chi^{(2)}_{ijk}\, E_j(t)\, E_k(t) \qquad (2)$$

In order to simplify the amount of algebra only the term with i=j=k=1 is examined and all the other terms are assumed to be zero. The 2nd order nonlinear susceptibility, $\chi^{(2)}_{ijk}$, is approximated as a constant as well. If all the subscripts are dropped and the driving electromagnetic field is assumed to have the following form:

$$E(t) = E(\omega_2,z,t) + E(\omega_3,z,t) \qquad (3)$$

Then the following equation describing the polarization is obtained:

$$\rightarrow P(t) = \varepsilon_0\, \chi^{(2)}\, E(t)\, E(t)$$

$$= \varepsilon_0\, \chi^{(2)}\, (E^2(\omega_2,z,t) + E^2(\omega_3,z,t) + 2\, E(\omega_2,z,t)\, E(\omega_3,z,t)) \qquad (4)$$

The last term in equation (4) for an electromagnetic field described by the following equation:

$$E(\omega_i,t,z) = E(\omega_i)\, e^{i\,(k_i z - \omega_i t)} + E^{*}(\omega_i)\, e^{-i\,(k_i z - \omega_i t)} \qquad (5)$$

is:

$$\begin{aligned} E(\omega_2,z,t)\; E(\omega_3,z,t) = \\ & E(\omega_2)\, E(\omega_3)\, e^{i\,(k_2 + k_3)\, z}\, e^{-i\,(\omega_2 + \omega_3)\, t} \\ & + E(\omega_2)\, E^{*}(\omega_3)\, e^{i\,(k_2 - k_3)\, z}\, e^{-i\,(\omega_2 - \omega_3)\, t} \\ & + E^{*}(\omega_2)\, E(\omega_3)\, e^{-i\,(k_2 - k_3)\, z}\, e^{i\,(\omega_2 - \omega_3)\, t} \\ & + E^{*}(\omega_2)\, E^{*}(\omega_3)\, e^{-i\,(k_2 + k_3)\, z}\, e^{i\,(\omega_2 + \omega_3)\, t} \end{aligned} \qquad (6)$$

The indices of refraction are chosen in such a way that oscillating electron polarization at the difference frequency $\omega_1 = \omega_3 - \omega_2$ generates an electromagnetic wave at the same frequency. The propagation vector does not need to satisfy the conservation of wave-vector $k_1 = k_3 - k_2$ for a finite crystal length since constructive interference of the waves can still occur. The equation which must be satisfied is $k_1 = k_3 - k_2 + \Delta k$, where $|\Delta k\, l| \leq 2\pi$ for a crystal of length l. For an infinitely long crystal, $\Delta k = 0$.

Appendix II

Peak Power Calculation

$$\text{FWHM} = 10\ \text{ns} = 2\,\tau_{width}$$

$$\frac{1}{2} P_0 = P_0\, e^{-a\,\tau_{width}^2}$$

$$E_{tot} = \int_{-\infty}^{\infty} P_0\, e^{-a\,t^2}\, dt = \sqrt{\frac{\pi}{a}}\, P_0$$

$$\frac{1}{2} P_0 = P_0\, e^{-a\,(5\ \text{ns})^2}$$

$$\rightarrow \ln 2 = a\,(5\ \text{ns})^2$$

$$\rightarrow a = \frac{\ln 2}{(5\ \text{ns})^2}$$

therefore,

$$P_0 = \sqrt{\frac{a}{\pi}}\, E_{tot}$$

$$= \frac{1}{5\ \text{ns}} \sqrt{\frac{\ln 2}{\pi}}\, E_{tot}$$

$$= 0.9394\ E_{tot}\ \text{Watts}$$

Appendix III

Tuning Curve Program

```
5 DEFDBL A-Z
6 CONST=100000!
10 INPUT "pump wavelength";ST
11 INPUT"pump wavelength increment";INC
20 INPUT "Crystal Temperature";T
21 PRINT "Crystal temperature is:,";T
22 LPRINT "Crystal temperature is: ";T
30 INPUT "initial guess for l1";L1
40 INPUT "tolerance on l1";D1
41 PRINT " Pump(nm)    Signal(nm)    Idler(nm)    ne(pump)     no(signal)   no(i
dler)"
42 LPRINT " Pump(nm)    Signal(nm)    Idler(nm)    ne(pump)     no(signal)   no(
idler)"
45 L3=ST
46 COUNT=0
50 CL1=L1
51 COUNT=COUNT+1
60 L1=CL1+D1/CONST
70 GOSUB 5000
80 Y1=F0
90 L1=CL1-D1/CONST
100 GOSUB 5000
110 Y2=F0
120 F1=(Y1-Y2)/(2*D1/CONST)
130 L1=CL1
140 GOSUB 5000
150 B=F0-L1*F1
160 F=F0
170 G=F1
180 PL1=CL1
190 L1=-B/G
195 IF COUNT>CONST THEN GOTO 230
200 IF ABS(L1-PL1)>D1 THEN GOTO 50
210 GOSUB 5000
211 X1=INT(NE3*1000000!+.5)/1000000!
212 X2=INT(NO1*1000000!+.5)/1000000!
213 X3=INT(NO2*1000000!+.5)/1000000!
220 PRINT L3,INT(L1+.5),INT(L2+.5);"     ";X1;"   ";X2;"   ";X3
221 LPRINT L3,INT(L1+.5),INT(L2+.5);"     ";X1;"   ";X2;"   ";X3
224 L3=L3+INC
225 GOTO 46
230 END
5000 L2=L1*L3/(L1-L3)
5010 FK=(T-24.5)*(T+24.5+546)
5020 NO1=4.9048+(117800!+.023416*FK)/(L1^2-(218.02-2.9671E-05*FK)^2)
5030 NO1=(NO1-2.7153E-08*L1^2+2.1429E-08*FK)^.5
5040 NO2=4.9048+(117800!+.023416*FK)/(L2^2-(218.02-2.9671E-05*FK)^2)
5050 NO2=(NO2-2.7153E-08*L2^2+2.1429E-08*FK)^.5
5060 NE3=4.582+(99210!+.052716*FK)/(L3^2-(210.9-4.9143E-05*FK)^2)
5070 NE3=(NE3-2.194E-08*L3^2+2.2971E-07*FK)^.5
5080 F0=NO1/L1+NO2/L2-NE3/L3
5090 RETURN
```

Appendix IV

Bandwidth Program

```
10 DEFDBL A-Z
20 CONST=100000!
30 INPUT "pump wavelength";ST
40 INPUT"pump wavelength increment";INC
50 INPUT "Crystal Temperature";T
60 FK=(T-24.5)*(T+24.5+546)
70 INPUT"crystal length";LENGTH
80 LPRINT"crystal lentgth";LENGTH
90 PRINT "Crystal temperature is: ";T
100 LPRINT "Crystal temperature is: ";T
110 INPUT "initial guess for l1";L1
120 INPUT "tolerance on l1";D1    !
130 PRINT " Pump(nm)    Signal(nm)    Idler(nm)    dw12(cm-1)   dw13(cm-1)   dw2
3(cm-1)"
140 LPRINT " Pump(nm)    Signal(nm)    Idler(nm)    dw12(cm-1)   dw13(cm-1)   dw
23(cm-1)"
150 L3=ST
160 COUNT=0
170 CL1=L1
180 COUNT=COUNT+1
190 L1=CL1+D1/CONST
200 GOSUB 590
210 Y1=F0
220 L1=CL1-D1/CONST
230 GOSUB 590
240 Y2=F0
250 F1=(Y1-Y2)/(2*D1/CONST)
260 L1=CL1
270 GOSUB 590
280 B=F0-L1*F1
290 F=F0
300 G=F1
310 PL1=CL1
320 L1=-B/G
330 IF COUNT>CONST THEN GOTO 580
340 IF ABS(L1-PL1)>D1 THEN GOTO 170
350 GOSUB 590
360 DNO1=-(117800!+2.3416E-06*FK)/(L1^2-(218.02-2.9671E-05*FK)^2)^2
370 DNO1=(DNO1-2.7153E-08)*L1/NO1
380 DNO2=-(117800!+2.3416E-06*FK)/(L2^2-(218.02-2.9671E-05*FK)^2)^2
390 DNO2=(DNO2-2.7153E-08)*L2/NO2
400 DNE3=-(99210!+.052716*FK)/(L3^2-(210.9-4.9143E-05*FK)^2)^2
410 DNE3=(DNE3-2.194E-08)*L3/NE3
420 DK1=NO1-L1*DNO1
430 DK2=NO2-L2*DNO2
440 DK3=NE3-L3*DNE3
450 B12=DK1-DK2
460 B13=DK3-DK1
470 B23=DK3-DK2
480 DW12=1/(B12*LENGTH)
490 DW13=1/(B13*LENGTH)
500 DW23=1/(B23*LENGTH)
510 X1=INT(DW12*1000000!+.5)/1000000!
520 X2=INT(DW13*1000000!+.5)/1000000!
530 X3=INT(DW23*1000000!+.5)/1000000!
540 PRINT L3,INT(L1+.5),INT(L2+.5);"      ";X1;"   ";X2;"   ";X3
550 LPRINT L3,INT(L1+.5),INT(L2+.5);"      ";X1;"   ";X2;"   ";X3
560 L3=L3+INC
570 GOTO 160
580 END
590 L2=L1*L3/(L1-L3)
600 NO1=4.9048+(117800!+.023416*FK)/(L1^2-(218.02-2.9671E-05*FK)^2)
610 NO1=(NO1-2.7153E-08*L1^2+2.1429E-08*FK)^.5
620 NO2=4.9048+(117800!+.023416*FK)/(L2^2-(218.02-2.9671E-05*FK)^2)
630 NO2=(NO2-2.7153E-08*L2^2+2.1429E-08*FK)^.5
640 NE3=4.582+(99210!+.052716*FK)/(L3^2-(210.9-4.9143E-05*FK)^2)
650 NE3=(NE3-2.194E-08*L3^2+2.2971E-07*FK)^.5
```

Appendix V

Gain Coefficient Program

```
5 DEFDBL A-Z
6 CONST=100000!
10 INPUT "pump wavelength";ST
11 INPUT"pump wavelength increment";INC
20 INPUT "Crystal Temperature";T
21 PRINT "Crystal temperature is: ";T
22 LPRINT "Crystal temperature is: ";T
30 INPUT "initial guess for l1";L1
40 INPUT "tolerance on l1";D1
41 PRINT " Pump(nm)    Signal(nm)    Idler(nm)    ne(pump)    no(signal)   no(i
dler)"
42 LPRINT " Pump(nm)    Signal(nm)    Idler(nm)    ne(pump)    no(signal)   no(
idler)"
45 L3=ST
46 COUNT=0
50 CL1=L1
51 COUNT=COUNT+1
60 L1=CL1+D1/CONST
70 GOSUB 5000
80 Y1=F0
90 L1=CL1-D1/CONST
100 GOSUB 5000
110 Y2=F0
120 F1=(Y1-Y2)/(2*D1/CONST)
130 L1=CL1
140 GOSUB 5000
150 B=F0-L1*F1
160 F=F0
170 G=F1
180 PL1=CL1
190 L1=-B/G
195 IF COUNT>CONST THEN GOTO 230
200 IF ABS(L1-PL1)>D1 THEN GOTO 50
210 GOSUB 5000
211 X1=INT(NE3*1000000!+.5)/1000000!
212 X2=INT(NO1*1000000!+.5)/1000000!
213 X3=INT(NO2*1000000!+.5)/1000000!
214 GAMMA=8*3.14159^2*6.25E-12^2/(L1*1E-09*L2*1E-09*NO1^2*NO2^2*NE3*3E+08*8.854E
-12)
215 PRINT "gamma^2/I3";GAMMA
216 LPRINT "gamma^2/I3";GAMMA
220 PRINT L3,INT(L1+.5),INT(L2+.5);"      ";X1;"    ";X2;"    ";X3
221 LPRINT L3,INT(L1+.5),INT(L2+.5);"      ";X1;"    ";X2;"    ";X3
224 L3=L3+INC
225 GOTO 46
230 END
5000 L2=L1*L3/(L1-L3)
5010 FK=(T-24.5)*(T+24.5+546)
5020 NO1=4.9048+(117800!+.023416*FK)/(L1^2-(218.02-2.9671E-05*FK)^2)
5030 NO1=(NO1-2.7153E-08*L1^2+2.1429E-08*FK)^.5
5040 NO2=4.9048+(117800!+.023416*FK)/(L2^2-(218.02-2.9671E-05*FK)^2)
5050 NO2=(NO2-2.7153E-08*L2^2+2.1429E-08*FK)^.5
5060 NE3=4.582+(99210!+.052716*FK)/(L3^2-(210.9-4.9143E-05*FK)^2)
5070 NE3=(NE3-2.194E-08*L3^2+2.2971E-07*FK)^.5
5080 F0=NO1/L1+NO2/L2-NE3/L3
5090 RETURN
```

References

1. J.A. Giordmaine and R.C. Miller, Physical Review Letters, **24**, 973 (1965).

2. J. Falk and J.E. Murray, Applied Physics Letters, **14**, 245 (1969).

3. R.W. Wallace, Applied Physics Letters, **17**, 497 (1970).

4. R.W. Wallace, IEEE J. Quantum Electronics, **8**, 819 (1972).

5. A. Piskarskas, V. Smil'gyavichyus, A. Umbrasas, and I. Yuodishyus, Sov. J. Quantum Electronics, **16**, 841 (1986).

6. G. Ionushauskas, A. Piskarskas, V. Sirutkaitis, and A. Yuozapavichyus, Sov. J. Quantum Electronics, **17**, 1303 (1988).

7. M.L.W Thewalt and D.J.S. Beckett, Can. J. Physics, **66**, 868 (1988).

8. M. Ignatavichyus, G. Orshevskii, V. Potsyunas, and É. Skardhyus, Sov. J. Quantum Electronics, **19**, 318 (1989).

9. Pan Zhonghan, Cui Yiben, Tang Hong, Lu Shiping, Wu Lusheng, Qi Hongxin, Chinese Journal of Lasers, **15** , 55 (1988).

10. Yu. A. Bakhirkin, Yu. A. Byokovskii, A.S. Sokol'nikov, V.A. Ukrainstev, A.A. Chistyakov, and T.M. Yakupov, Sov. J. Quantum Electronics, **18**, 1277(1989).

11. P.G. Harper and B.S. Wherrett, Nonlinear Optics, Proceedings of the Sixteenth Scottish Universities Summer School in Physics, 1975, New York: Academic Press Inc., 1977, pp.53,58-59.

12. Ibid, p.83.

13. Ibid, p.86.

14. Ibid, p.87.

15. Ibid, p.88.

16. S.E. Harris, Proceedings of the IEEE , **57**, 2096 (1969).

17. J.E. Bjorkholm, IEEE Journal of Quantum Electronics, **7**, 109 (1971).

18. P.P. Bey, and C.L. Tang, IEEE Journal of Quantum Electronics, **8**, 361 (1972).

19. S.J. Brosnan, and R.L. Byer, IEEE Journal of Quantum Electronics, **15**, 415 (1979).

20. S.J. Brosnan, and R.L. Byer, IEEE Journal of Quantum Electronics, **15**, 432 (1979).

21. J.V. Moloney, and A.C. Newell, Physica D, **44**, 1 (1990).

22. L.B. Kreuzer, Proceedings of the Joint Conference on Lasers and Opto-Electronics, London, 1969, p.53.
23. P.G. Harper and B.S. Wherrett, Nonlinear Optics, Proceedings of the Sixteenth Scottish Universities Summer School in Physics, 1975, New York: Academic Press Inc., 1977, p.68.
24. O. Svelto, Principles of Lasers, New York: Plenum Press, 1982, p. 317.
25. E. Hecht, Optics, Reading, Massachussetts:Addison-Wesley Publishing Company, 1987, p. 282.
26. Ibid. p. 289.
27. P.G. Harper and B.S. Wherrett, Nonlinear Optics, Proceedings of the Sixteenth Scottish Universities Summer School in Physics, 1975, New York: Academic Press Inc., 1977, p.65.
28. O. Svelto, Principles of Lasers, New York: Plenum Press, 1982, p.318.
29. Properities of Lithium Niobate, EMIS Datareview Series No. 5, London: INSPEC, 1989, pp.131-142.
30. M.V. Hobden, and J. Warner, Physics Letter, **22**, 243 (1966).
31. D.F. Nelson, and R.M. Mikulyak, Journal of Applied Physics, **45**, 3688 (1974).
32. D.S. Smith, and H.D. Riccius, Optics Communications, **17**, 332 (1976).
33. V.K. Semenchenko, I.T. Bodnar, and V.P. Yarunichev, Opt. Spectrosc. (USSR), **54**, 405 (1983).
34. G.J. Edwards, and M. Lawrence, Optical and Quantum Electronics,**16**, 373 (1984).
35. D.H. Jundt, M.M. Fejer, and R.L. Byer, IEEE Journal of Quantum Electronics, **26**, 135 (1990).
36. P.G. Harper and B.S. Wherrett, Nonlinear Optics, Proceedings of the Sixteenth Scottish Universities Summer School in Physics, 1975, New York: Academic Press Inc., 1977, p.53.
37. G.D. Boyd, R.C. Miller, K. Nassau, W.L. Bond, and A. Savage, Applied Physics Letters, **5**, 234 (1964).
38. J.E. Bjorkholm, Applied Physics Letters, **13**, 36 (1968).
39. J.E. Bjorkholm, IEEE Journal of Quantum Electronics, **5**, 260 (1969).
40. R.C. Miller, and W.A. Nordland, Applied Physics Letters, **16**, 174 (1970).
41. P.G. Harper and B.S. Wherrett, Nonlinear Optics, Proceedings of the Sixteenth Scottish

Universities Summer School in Physics, 1975, New York: Academic Press Inc., 1977, p.68.

42. P.G. Harper and B.S. Wherrett, Nonlinear Optics, Proceedings of the Sixteenth Scottish Universities Summer School in Physics, 1975, New York: Academic Press Inc., 1977, p.148.

43. Ibid, p. 133.

44. A.E. Siegman, Applied Optics **1**,739 (1962).

45. L.B. Kreuzer, Applied Physics Letters, **13**, 57 (1968).

46. R.L. Byer, and S.E. Harris, Physical Review, **168**,1064 (1968).

47. D.J. Kuizenga, Applied Physics Letters, **21**, 570 (1972).

48. P.G. Harper and B.S. Wherrett, Nonlinear Optics, Proceedings of the Sixteenth Scottish Universities Summer School in Physics, 1975, New York: Academic Press Inc., 1977, p.117.

49. Ibid, p.86.

50. R.C. Miller, and W.A. Nordland, Applied Physics Letters, **10**, 53 (1967).

51. S.E. Harris, M.K. Oshman, and R.L. Byer, Physical Review Letters, **18**, 732 (1967).

52. M.J. Colles, and R.C. Smith, Applied Physics Letters, **10**, 309 (1967).